Optical and Near-Infrared Photometry of Old Galactic Clusters

by

Joanne Marie Rosvick
B.Sc., University of Alberta, 1987
M.Sc., University of Victoria, 1990

A Dissertation Submitted in Partial Fulfillment of the
Requirements for the Degree of

DOCTOR OF PHILOSOPHY

in the Department of Physics and Astronomy

We accept this dissertation as conforming
to the required standard

Dr. C. D. Scarfe, Supervisor

Dr. T. J. Davidge, Supervisor

Dr. F. D. A. Hartwick,
Departmental Member

Dr. D. A. VandenBerg,
Departmental Member

Dr. A. C. Gower, Departmental Member

Dr. P. Wan, Outside Member

Dr. E. D. Friel, External Examiner

Abstract

Supervisors: Dr. C. D. Scarfe, Dr. T. J. Davidge

The open clusters NGC 2141, NGC 6791, NGC 6819 and NGC 7142, all suspected of having ages greater than 2 billion years (Gyr), were observed at optical and near-infrared wavelengths. The images were reduced using standard IRAF routines, and magnitudes for the stars were determined using DAOPHOT (Stetson, 1987). These data were used to construct colour-magnitude diagrams (CMDs) for each cluster, as well as two-colour diagrams $(J-K, V-K), (J-H, H-K)$ of the giants.

Colour excesses were redetermined by comparing the optical CMD main sequences to semi-empirical ZAMS calibrations (VandenBerg and Poll, 1989; this work) and are as follows: $E(B-V) = 0.32 \pm 0.04$, 0.23 ± 0.03, 0.11 ± 0.03 and 0.29 ± 0.04, for NGC 2141, NGC 6791, NGC 6819 and NGC 7142, respectively. Apparent distance moduli for the clusters listed above were found to be $(m-M)_V = 13.93 \pm 0.13$, 13.52 ± 0.13, 12.10 ± 0.13 and 12.96 ± 0.16.

The optical CMDs were compared to sets of theoretical isochrones to ascertain ages and test whether canonical or convective overshooting models best represent the data. It was found that isochrones which allowed for convective overshooting provided the best fits, resulting in ages of 2.5 Gyr, 10 Gyr, 2.5 Gyr and 2.5 Gyr for NGC 2141, NGC 6791, NGC 6819 and NGC 7142, respectively. Two sets of overshooting isochrones (Bertelli et

al., 1994; Dowler and VandenBerg, 1996) yielded ages within 0.5 Gyr. The MAR method (Anthony-Twarog and Twarog, 1985) placed the three younger clusters at an approximate age of 3 Gyr.

In theory, the two-colour diagrams may be used to distinguish between cluster giants and field stars. However, in practice this is not an easy task since the infrared observations are not always accurate enough to separate the cluster members and field stars. This was the case for these data, since a problem with the H magnitudes resulted in colours offset from what was expected.

The infrared ($V, V-K$ and $K, V-K$) CMDs were useful in defining the giant branch locus based on the position of cluster members. $(V-K)_0$ colours were computed for each giant suspected of being a member. These were used to determine effective temperatures and bolometric luminosities, which in turn were used to produce an HR diagram for each cluster. These were compared to HR diagrams of other open and globular clusters (Houdashelt et al., 1992; Frogel et al., 1983), as well as evolutionary tracks (Bertelli et al., 1994). The giant branch loci of the near-solar abundance and metal-poor clusters were found to lie between those defined by the clusters M67 and 47 Tuc. The comparison between the cluster HR diagrams and evolutionary tracks indicated that the theoretical temperatures may be too hot.

The new cluster results were plotted on the age-metallicity relation defined by Houdashelt et al.'s (1992) and Friel and Janes' (1993) sample of open clusters, and confirmed the lack of correlation between these two quantities. The galactocentic distances (calculated from the distances given above) for the clusters studied here were determined and used with the cluster metallicities to support the presence of a metallicity gradient (~ -0.09 dex kpc^{-1}) in the galaxy.

Examiners:

Dr. C. D. Scarfe, Supervisor (Department of Physics & Astronomy)

Dr. T. J. Davidge, Supervisor (Department of Physics & Astronomy, University of British Columbia)

Dr. F. D. A. Hartwick, Departmental Member (Department of Physics & Astronomy)

Dr. D. A. VandenBerg, Departmental Member (Department of Physics & Astronomy)

Dr. A. C. Gower, Departmental Member (Department of Physics & Astronomy)

Dr. P. Wan, Outside Member (Department of Chemistry)

Dr. E. Friel, External Examiner (National Science Foundation)

Acknowledgements

First and foremost, I would like to thank Colin Scarfe for convincing me to undertake this endeavour and then agreeing to co-supervise me for yet another degree, and Tim Davidge for co-supervising me as well despite being already busier than is humanly possible. Their patience, knowledge, guidance and friendship is deeply appreciated, and they have made the past four years an immense learning experience, both scholastically and personally.

I also would like to thank Don VandenBerg and David Hartwick for the advice they gave me during several discussions regarding various aspects of this work. I appreciate the time Pat Dowler took to generate some of his isochrones for comparison with my clusters, and would like to thank him for explaining all sorts of concepts associated with convective overshooting. I am also grateful to Dave Zurek for obtaining some of the observations of NGC 2141 and NGC 6791.

All the observations were taken with the 1.8 m telescope at the DAO, and this would not have been possible without the help from Les Saddlemyer, Doug Bond and Frank Younger. They have been super night assistants, and were always ready to help. I offer them my thanks. Of course, I could not have observed so much had Robert McClure not been so generous with telescope time! I have him to thank for so many observing nights. I do not, however, thank the Victoria weather demons for being so uncooperative during many of those nights.

With the work comes stress, and much of the tension was relieved through the friendship of the 4th floor crowd. I have the other grad students, Russ Robb and Ann Gower to thank for listening to my problems and brightening my mood. You all are better than any psychiatrist, and you don't cost as much!

When the stress was too great to be reduced by hearing the sounds of Homer Simpson or farm animals emanating from the workstations, or the sounds of laughter, I knew I could count on karate to relieve me of it for at least a few hours. My deepest thanks go to Sensei Greg, Sensei Erich, Sensei Debra and Sensei Brendan for encouraging me to develop a side of myself I never knew existed, and for guiding me down the path towards greater peace and strength.

I would like to thank my parents, and my brother and sister for their support and encouragement and for trying to understand why I would want to go to University for so many years (yes Dad I'm going to get a real job now), and the feline members of my family for providing me with much-needed fuzz therapy throughout my university career. Finally, I am eternally grateful to my husband Myron for his never-ending well of patience, encouragement and love. I'm sure he will be as glad as I that this work is completed!

Contents

List of Tables

List of Figures

Chapter 1

Introduction

The internal structure of a star has been shown theoretically to depend on its mass and its chemical composition profile which may vary with its evolutionary state (Mihalas and Binney, 1988a). As the star's chemical profile changes, its structural properties change. These changes manifest themselves in the Hertzsprung-Russell (brightness versus spectral type) diagram. Inspection of the Hertzsprung-Russell (or HR) diagram in Figure 1.1 (Kaufmann, 1987) shows that stars populate several distinct sequences. The majority of stars lie on the main sequence, which ranges from hot, luminous stars to cool, faint ones. The giant branch is the next most prominent sequence. Stars located there are cool and about 100 times more luminous than main sequence stars of the same spectral class. Supergiants, at the top of the diagram, are extremely bright stars which span a range of spectral classes, while white dwarfs, stars which are near the end of their lives, are faint, cool, and reside about ten magnitudes below the main sequence. Since each sequence represents a different stage of a star's life, the HR diagram should yield important information about stellar evolution.

While the nearby stars are the easiest to study, they do not constitute a homogeneous sample, as they cover a range of chemical compositions, masses, ages and distances. An HR diagram composed of these stars is a confusing

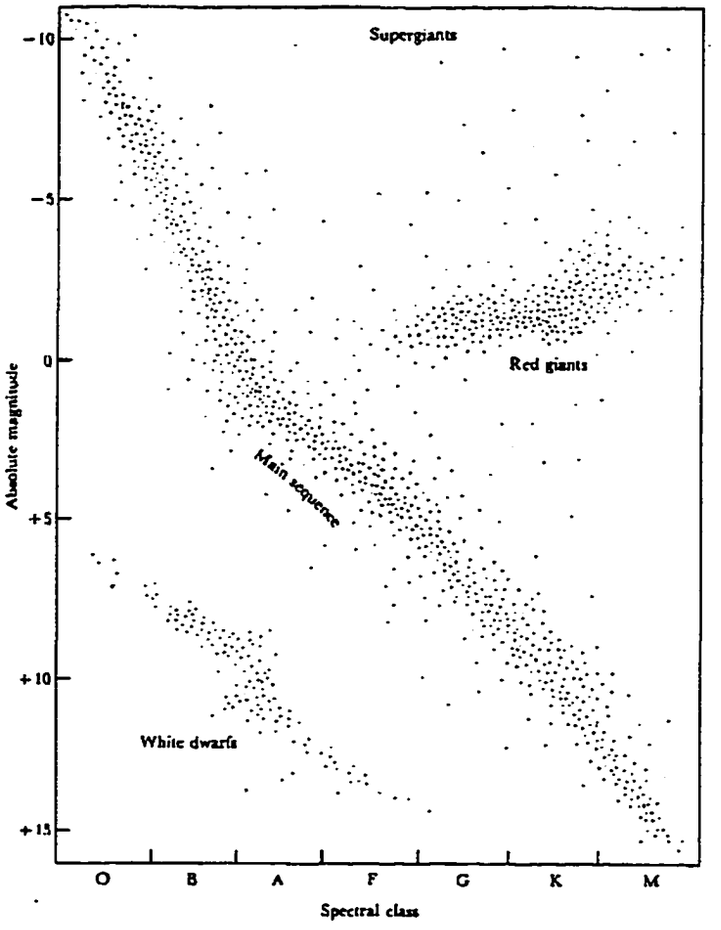

Figure 1.1: HR diagram illustrating main sequence dwarfs, red giants, supergiants and white dwarfs. Absolute visual magnitude is plotted along the ordinate, spectral class is along the abscissa. Absolute visual magnitudes of 5, 0 and -5 correspond roughly to luminosities 1, 100 and 10,000 times that of the sun. Spectral classes of A0, F0 and G0 correspond approximately to effective temperatures of 10 000, 7500 and 6200 Kelvin, respectively. From Kaufmann (1987).

scatter of points, and thus very difficult to analyse. The advantage of using star clusters is that the stars probably formed at the same time from the fragmentation of a vast, dense molecular cloud (Lada and Lada, 1991), and therefore are of similar age, initial chemical composition and distance from us. Since they only differ in their masses, the cluster as a whole provides us with a snapshot of the relative evolutionary behaviour of the stars.

Our galaxy contains two main types of stellar clusters, as well as looser systems called associations (Mihalas and Binney, 1988b). Globular clusters are found in two groups – a metal-poor spherical halo and a somewhat flattened, higher metallicity "disk" (Zinn, 1991). These clusters contain hundreds of thousands of stars in a roughly spherical volume with typical radius 20-50 pc. Globular clusters are old (ages $>$ 10 billion years), and recent evidence points toward an age spread (as much as 3-4 billion years) among clusters of similar metallicity (VandenBerg et al., 1990; Sarajedini and Demarque, 1990).

Open, or galactic, clusters are located in the disk of the galaxy, and usually are loose and somewhat irregular in morphology. These clusters contain a wide variety of stellar types, and range in age from a few million to several billion years. While the youngest clusters often have stars still forming, and therefore provide clues about star and cluster formation (Lada and Lada, 1991), the old ones serve as valuable probes of the formation and evolution of the galactic disk (Phelps et al., 1994; Janes et al., 1988). Since the oldest open clusters of the galaxy are located almost exclusively beyond the solar galactocentric radius, having escaped tidal disruption by interactions with molecular clouds, they also act as tracers of the outer galactic disk (Friel, 1993; Friel, 1995). However, past attempts to study them have been fraught with problems, since the clusters are distant and old methods of obtain-

ing photometry did not provide reliable results. For example, photographic plates, while useful for the spatial coverage they provide, are not as sensitive as CCDs, and thus old photographic photometry often did not extend faint enough, nor was it very accurate (see van den Bergh and Heeringa (1970); Burkhead et al. (1972), for example).

1.1 Problems

The advent of CCD (charge-coupled device) detectors has improved upon efforts to identify and study distant clusters, but problems still exist which hinder accurate calculations of fundamental parameters such as age, distance and heavy element abundance. For example, some clusters lie in or very close to the galactic plane, where obscuration from interstellar material can be substantial, and nonuniform (Friel, 1993). As well, intracluster extinction may vary across the cluster face (extinction refers to the dimming of starlight caused by absorption and scattering of the light by intervening interstellar or intracluster dust and the earth's atmosphere. Starlight is also reddened since the extinction of blue light is greater than that of red light). This serves to broaden the main sequence of the observed colour-magnitude diagram (the photometric counterpart of the HR diagram, hereafter designated CMD), and it can be difficult to correct the photometry properly (Crinklaw and Talbert, 1991). Consequently, the ages obtained by fitting theoretical isochrones, as well as distances determined from techniques such as main-sequence fitting, are uncertain. Attempts to correct for this differential extinction by adjusting the photometry according to mean reddening values determined for different parts of the cluster are time-consuming, and still may not produce a CMD suitable for accurate measurement of various parameters.

Ambiguity in cluster membership also affects the width of the main se-

quence. The CMD of field stars resembles those of open clusters, and since many of these clusters appear against a rich background (and foreground) of field stars, contamination of the cluster CMD by non-members can be great. The distances of these clusters render proper motion studies inapplicable in most cases (Mihalas and Binney, 1988c), while attempts to establish membership on the basis of radial velocities may be fruitless since velocities can be obtained only for the few brightest stars and there may not be significant contrast with respect to nearby field stars.

Line-blanketing affects the shape of the energy distribution, mostly at optical wavelengths, and increases for metal-rich clusters and for the coolest stars (Mihalas and Binney, 1988d). One effect of this phenomenon is to cause the cooler, more bolometrically luminous part of the red giant branch of certain colour-magnitude diagrams to hook back and droop down towards fainter magnitudes in the CMD (see Ortolani et al. (1990), for example), since line-blanketing is larger in V relative to B for the coolest stars. In the past, this distortion was interpreted as a metallicity effect, *i.e.* a spread in metallicity would cause a widening of the giant branch. An important implication of this problem is the fact that it is very difficult to obtain the true absolute bolometric magnitude of the red and asymptotic giant branch tips, from the CMD in question, since the optical brightnesses of the giants no longer increase monotonically with bolometric luminosity.

1.2 Advantages of Near-infrared Observations

There are several reasons why near-infrared observations are particularly applicable to the situations described above (note that throughout this work near-infrared refers to wavelengths longer than 9000 $\AA$). For example, interstellar and intracluster extinction are greatly decreased at near-infrared

wavelengths [by a factor of ten at 2.2 μm, according to Joyce (1992)]. Thus, extinction corrections are much smaller. Also, normal interstellar dust produces a ratio R of visual extinction A_V to colour excess $E(B-V)$ of about 3.0 [Rieke and Lebofsky (1985) derived a value of 3.09 ± 0.03 from measurements of stars toward the galactic centre], but this ratio may be different in other directions, because of different grain properties (note that throughout this work, $R = 3.09$ has been adopted). This is important since most of the target clusters are not located toward the galactic centre, and serious errors in determining the reddening and distance of the clusters (based on optical data) may arise from the variation in R. However, since the reddening is smaller in purely infrared colours [$(J-H)$, for example], the choice of R has little influence at red and infrared wavelengths. Thus, the reddening and distance may be determined with more reliability using infrared data.

As was stated above, it is difficult to establish cluster membership, and while observing several "blank" fields near the cluster helps to assure that the statistics will be reliable, it does not indicate which stars are members and which ones are not. However, it is possible to distinguish between cluster giants and foreground dwarf field stars by making observations at both optical and near-infrared wavelengths. The $(J-H, H-K)$ and $(V-K, J-K)$ colour-colour diagrams are sensitive to surface gravity g (Cohen et al., 1978), and since the atmospheres of giants and dwarfs have different values of g, they lie along different loci in the colour-colour diagrams. For example, at $(H-K) = 0.2$, the $(J-H)$ colour of giants is about 0.85 ± 0.05, while that for dwarfs is only 0.68 ± 0.1 (Bessell and Brett, 1988). Errors are estimated from the scatter in the diagram.

In their study of the metal-rich globular cluster NGC 6553, Ortolani et al. (1990) include optical CMDs which illustrate clearly the distortion

of the red giant branch due to line-blanketing by molecules, mostly TiO and ZrO. As their data progress towards longer wavelengths, the amount of distortion decreases, in that the giant branch gradually rises upward. The next two figures illustrate the extremes of this case: Figure 1.2 shows their $(V, B-V)$ CMD in which the upper half of the red giant branch has folded back upon itself to the extent that the actual tip has the same magnitude as the horizontal branch, while the giant branch in the $(I, V-I)$ diagram is straighter and forms an arc extending to the red. Garnavich et al. (1994) have studied the metal-rich open cluster NGC 6791 (one of the clusters in this study), and their optical CMDs and the near-infrared ones contained in this work illustrate this effect very clearly. As will be shown in Chapter 4, the giant branch of NGC 6791 at near-infrared wavelengths is nearly vertical.

1.3 Stellar Models

It is important to study intermediate-age open clusters since the cluster stars leaving the main sequence are undergoing a period of evolution crucial for detailed tests of stellar evolution. Convection is the main source of energy transport in the cores of these stars, the principles of which are explained briefly below (see, for example, Böhm-Vitense (1989) for details).

Imagine a small mass element in the stellar core which is given an initial outward radial displacement. At a higher level in the core, the mass element expands to adjust to the lower gas pressure of the new surroundings, and cools nearly adiabatically (i.e., with very little heat lost). If the adiabatic temperature gradient $\frac{dT}{dP_{gas}}$ is less than the temperature gradient in the surroundings, then an instability towards convection occurs, and the mass element continues to rise until it thermalizes with the local environment (this distance is called the mixing length parameter, α).

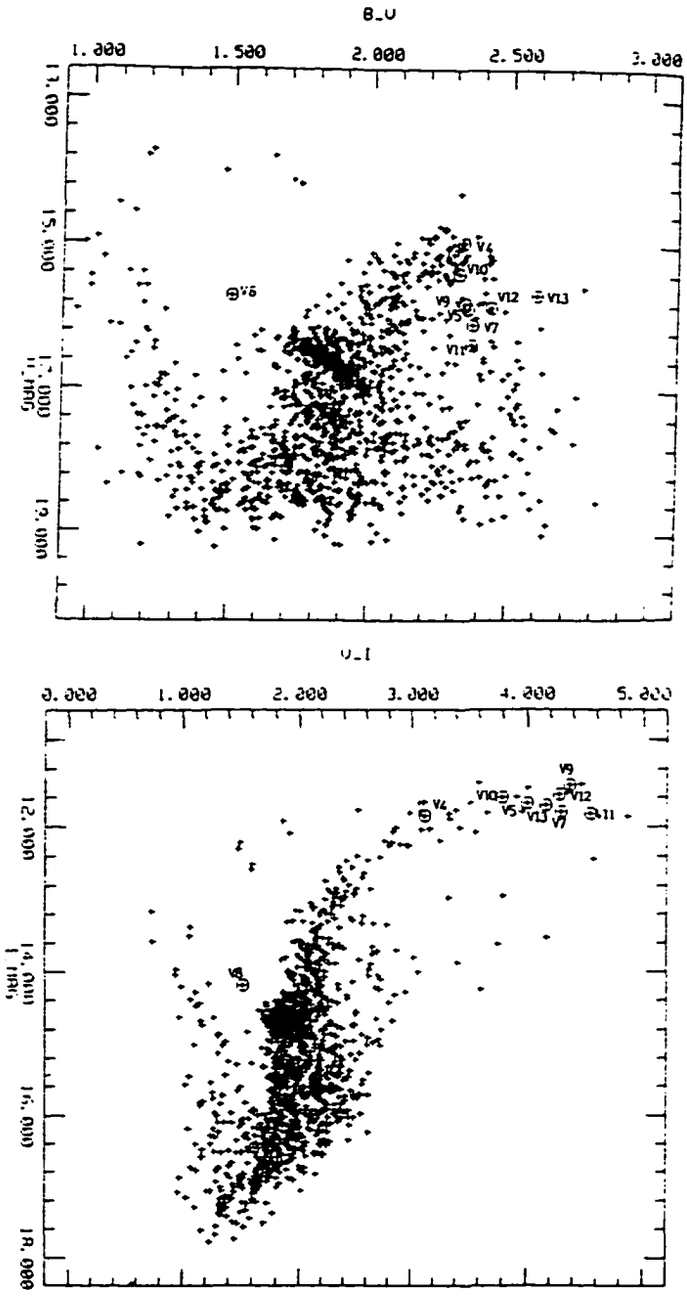

Figure 1.2: $(V, B-V)$ and $(I, V-I)$ CMDs of the metal-rich globular cluster NGC 6553, illustrating the effect of metallicity on the location of the extreme end of the giant branch. From Ortolani et al. (1990).

The mass element's motion causes the actual convection zone to extend beyond the point at which the gradients are equal. This phenomenon is called convective overshooting, and depends on the mass element's inertia as well as forces such as viscous dissipation which act to slow the upward motion. If overshooting occurs in a star which has a convective core, the main sequence evolution of that star may be dramatically altered since the core size, and therefore the hydrogen supply, is increased (according to Zahn (1983), an individual element may extend past the boundary only by a small amount, but the cumulative effect of several mass elements may enlarge the convective region considerably). Thus, the star is able to evolve to higher luminosities and lower surface temperatures before core hydrogen exhaustion occurs. The major implication of this is that the main sequence lifetime of the star is extended beyond that obtained by neglecting this effect, by as much as 20% for clusters 3-7 Gyr old (Maeder and Meynet, 1989). Stars which have convective cores are of intermediate mass (greater than 1.2 $M_{\odot}$) and age (less than 4-5 Gyr), and clusters whose turnoff stars are at least this massive are expected to show the effects of overshooting (Daniel et al., 1994).

To treat convection in the convective envelopes of stars, the adoption of mixing length theory (Böhm-Vitense, (1958), for example) allowed for the comparison between stellar evolutionary theory (via stellar models) and observational data, with the mixing length parameter α defined as the ratio of the mixing length to the pressure scale height. α is a free parameter in the models, and its value is subject to uncertainty. Therefore the comparison between the models and the observations provides a check on its value.

Chapter 5 contains a more extensive discussion on the construction of stellar models, but a brief introduction will be given here. The equations of stellar structure describe the run of temperature, pressure, radius and lumi-

nosity in the star, and require for their solution the chemical composition (fractions by mass of helium denoted by Y, and heavy elements, given by Z), mass of the star and mixing length parameter α as well as the density, opacity (a measure of the ability of the stellar material to absorb radiation) and energy generation rate. The calculations result in a series of evolutionary sequences which plot, for various stellar masses, a star's luminosity and effective temperature as it ages. Isochrones are obtained by connecting points on the evolutionary sequences at a specific time, and transformed to the observational plane prior to comparison with cluster CMDs.

When comparisons between canonical (non-overshooting) isochrones and intermediate-age cluster data were made, it was found that the theory did not match the observations (Maeder, 1975). In particular, the shape of the turnoff region in the cluster CMD did not follow the curve of the isochrone. Several authors reasoned that convective overshooting, which had not been included in the model calculations, could remove the discrepancy (Bressan et al., 1981; Maeder and Mermilliod, 1981; Bertelli et al., 1986; Mermilliod and Maeder, 1986). A controversy erupted regarding which models best represented real stars, as well as the extent of overshoot in the convective core. Those favouring the canonical models believed that large amounts of overshooting could be generated simply by including various physical assumptions or simplifications to suit the predictions (Eggleton, 1983), while assumptions regarding inner boundary conditions and methods of integrating the stellar structure equations produced negligible overshooting (Langer, 1986). More recently, Castellani et al. (1992) claimed that early conclusions for the presence of convective overshoot arose from the fact that the input physics resulted in a convective core which was too small (Becker and Mathews, 1983), and that updated canonical models which used improved

physics (newer opacities, for example) overcame the difficulties in the fit to observations and made overshooting unnecessary.

However, the wealth of new observational evidence lends strong support to the claim that overshooting is a non-negligible occurrence in intermediate-age stars (Mazzei and Pigatto, 1988; Bergbusch et al., 1991; Anthony-Twarog et al., 1991; Montgomery et al., 1993; Daniel et al., 1994; Dowler, 1994; Carraro et al., 1994). The most recent of these references use up-to-date canonical *and* overshooting models to make their comparisons (Bertelli et al., 1994; Dowler, 1994), and in all cases the latter models provide superior fits to the observations.

1.4 Motivation and Goals

In recent years, the galaxy has been surveyed in the hope of detecting more old open clusters, and several candidates have been found [see, for example, Janes and Phelps, (1994)]. However, many of these clusters have not yet been studied in detail. In particular, infrared photometry of old clusters has been done only for a sample of evolved stars in some of the better-known clusters (Houdashelt et al., 1992). The recent availability of near-infrared array cameras has made it possible to observe completely all but the nearest, largest clusters, but so far, only globular clusters (Davidge et al. (1996); Cohen and Sleeper (1995); Ferraro et al. (1995), and references therein, to name a few) and very young clusters still embedded in their parental clouds (Wilking et al. (1994) and Strom et al. (1993), for example) have been studied with these detectors. Near-infrared observations of the old open clusters are required for several reasons: to fill the gap in the observational database (which includes the construction of CMDs which should be more accurate than their optical counterparts because of reduced extinction), to

provide more clues to the timescale of galactic formation and evolution, and to constrain theoretical models.

Observations at optical (BVI) and near-infrared (JHK') [1] wavelengths of four open clusters were obtained as described in subsequent chapters. These observations were used to construct optical [$(V, B-V)$ and $(V, V-I)$] as well as $(V, V-K)$ and $(K, V-K)$ CMDs. The CMDs are intended to contribute to the number of "classical" observations, and assist in comparisons with similar-combination CMDs of other clusters in the literature, as well as provide the means to redetermine cluster parameters such as distance and age, which are poorly known for some of the target clusters. Both canonical and overshooting isochrones will be compared to the cluster CMDs to determine ages of the clusters as well as determine which kind of isochrones best represent the clusters studied here.

The $(V-K)$ colours enable computation of accurate effective temperatures using the colour-temperature scale derived from near-solar metallicity field giants of Ridgway et al. (1980) and that from metal-poor globular cluster giants of Frogel et al. (1978), as well as bolometric luminosities using the colour-bolometric correction relation derived by Frogel et al. (1981). Both the effective temperatures and bolometric luminosities will be useful to theorists who compute models of stellar evolution, since they provide valuable constraints.

1.5 Target Objects

The chosen clusters are suspected of having ages greater than two billion years: they are richly populated and located at or beyond the solar galacto-

[1] K' has its peak wavelength slightly blueward of that of K, yet still within the same atmospheric window.

centric radius and accessible with the Dominion Astrophysical Observatory's 1.8 m Plaskett telescope. Several catalogues (Janes and Adler, 1982; Lyngå, 1987) were examined in order to find candidate clusters meeting the various requirements and restrictions. These clusters are listed in Table 1.1; the right ascension and declination coordinates are for the equinox and equator of 1950.0, l and b are galactic longitude and latitude, respectively, and α is the angular diameter of the cluster in minutes of arc (note: Lyngå(1987) estimated these diameters by examining plates, and therefore they represent only the central concentration of stars). Height, in parsecs, above the galactic plane is denoted by z, while galactocentric radii R_{gc} are in kpc. Both quantities have been calculated for the cluster distances derived in Chapter 4. A diagram of the galactic disk showing the approximate relative projected positions of the four clusters is given in Figure 1.3. Numbers around the box refer to galactic longitude in degrees, while dotted lines indicate spiral arms; "P", "O-C" and "S" are the Perseus, Orion-Cygnus and Sagittarius arms, respectively. Uncertainties in the distances range from $0.1 - 0.5$ kpc. A short description of each cluster follows.

Table 1.1: Coordinates and angular diameters α of the candidate clusters. Also included are galactocentric radii R_{gc} in kpc, and height z above or below the galactic plane, in pc. Uncertainties in z range from 15 to 50 pc.

Cluster	RA (h m s)	DEC (° ′)	l(°)	b(°)	α (′)	z	R_{gc}
NGC 2141	06 00 18	10 26	198.1	−5.8	10	−385	12.2
NGC 6791	19 18 47	37 45	70.0	+11.0	15	745	8.0
NGC 6819	19 39 33	40 04	74.0	+8.5	5	295	8.2
NGC 7142	21 44 42	65 34	105.4	+9.5	4.3	330	9.2

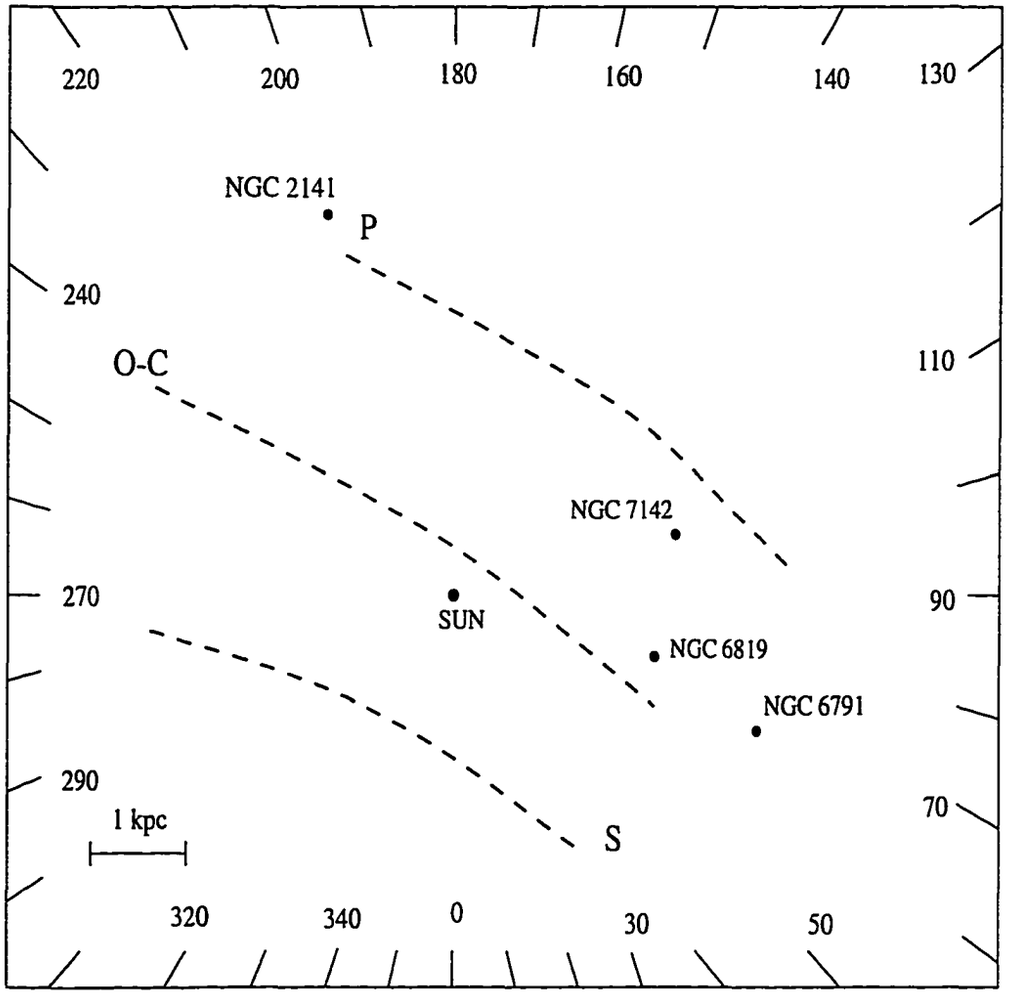

Figure 1.3: Schematic diagram illustrating the positions of the clusters with respect to the sun. Numbers refer to galactic longitude in degrees, and dashed lines indicate approximate locations of the median positions of the Perseus (P), Orion-Cygnus (O-C) and Sagittarius (S) spiral arms. A scale in kiloparsecs is given in the lower left corner.

NGC 2141

Burkhead et al. (1972) constructed the first CMD for this cluster, using photographic and photoelectric UBV observations of about 300 stars. They determined a mean colour excess of 0.30, an apparent distance modulus of $(m - M)_V = 14.1$, and an age estimate of about 4 Gyr. Janes (1979) determined, from DDO photometry, a metallicity of $[Fe/H] = -0.54 \pm 0.42$, while Geisler (1987) determined a value of -0.63 ± 0.15, from Washington photoelectric photometry. The most recent estimate of the metallicity has been computed by Friel and Janes (1993), who give a value of -0.39 ± 0.11 from medium-resolution spectra. No CCD photometry had been done on this cluster before the present study.

NGC 6791

This cluster is one of the oldest known, with an age estimated between 7 and 12 Gyr (Harris and Canterna, 1981; Janes, 1988; Kaluzny, 1990; DeMarque et al., 1992) and is metal-rich; Friel and Janes (1993) derive a value of the metallicity equal to 0.19 ± 0.19, from medium-resolution spectra. NGC 6791 is very important for studies of galactic evolution since its age and metallicity, and the presence of cluster members populating a blue horizontal branch (Kaluzny and Udalski, 1992; Liebert et al., 1994), seem to suggest it might be a link between the open and globular cluster populations.

Discrepancies regarding the value of the reddening abound in the literature. For example, several values around $E(B - V) = 0.10$ have been published (Harris and Canterna, 1981; Janes, 1984; Montgomery et al., 1994a), while many authors favour a $E(B-V) = 0.20$ (Anthony-Twarog and Twarog, 1985; Kaluzny and Udalski, 1992; Garnavich et al., 1994). New estimates

for the apparent distance modulus and age have been determined by Garnavich et al. (1994) as 13.65 $\pm$0.25 and 9 Gyr, respectively, based on a comparison of the CMD constructed from high quality VI CCD photometry with evolutionary tracks. Using radial velocities obtained from spectra, they confirm that at least 12 of the 25 giants observed are cluster members. A recent study by Tripicco et al. (1995) gives an age of 10 Gyr and colour excess of $0.19 < E(B-V) < 0.24$ provided the metallicity is in the range $0.44 > [Fe/H] > 0.27$.

NGC 6819

Lindoff (1972) and Auner (1974) both observed this cluster and constructed CMDs. Lindoff (1972) used photographic and photoelectric UBV photometry, while Auner (1974) used only photographic UBV photometry. Reddenings and distance moduli were estimated as 0.3 and 12.6 for the former, and 0.28 and 12.50 for the latter. Lindoff (1972) estimated the age as 2 Gyr. A proper-motion survey of 189 stars, conducted by Sanders (1972), yielded 129 stars having membership probabilities greater than zero. Canterna et al. (1986) obtained Washington photometry and determined a reddening of 0.15 and a metal abundance of -0.10, while Strobel (1989) gave the age as 3.5 Gyr. Kaluzny and Shara (1988) constructed a new CMD from optical CCD observations of approximately 850 stars, and estimated an age of 4 Gyr using the MAR technique (a morphological method which uses the CMD giant branch clump and cluster turnoff) developed by Anthony-Twarog and Twarog (1985). Finally, Friel and Janes (1993) determined, from medium-resolution spectra, a metallicity of $+0.05 \pm 0.19$.

NGC 7142

van den Bergh and Sher (1960) used star counts to construct a luminosity function for this cluster, while Hoag (1961) constructed the first CMD. Since then others have studied it in order to obtain accurate determinations of the reddening, age, distance and metallicity. However, the values for these quantities vary widely since there is a substantial amount of variable internal absorption. For example, the mean reddening varies from 0.18 (Johnson et al., 1961) to 0.41 (van den Bergh and Heeringa, 1970), while $[Fe/H]$ ranges from -0.45 (Jennens and Helfer, 1975) to about 0.0 (Friel and Janes, 1993). As well, the apparent distance modulus ranges from 10.5 (Johnson et al., 1961) to 13.7 (van den Bergh and Heeringa, 1970). Recently, Crinklaw and Talbert (1991) obtained BV CCD observations of approximately 1000 stars in the central region of the cluster, and determined a new estimate of the distance modulus as 12.7 ± 0.9 [$(m - M)_0 = 11.4$, $E(B - V) = 0.41$ as given in the paper]. They estimate the age of this cluster as 4 Gyr, using the MAR method.

1.6 Outline of the Thesis

Chapter 2 discusses CCD and IR photometry. A brief explanation of how the detectors operate will be given, and the similarities and differences, as well as the advantages and disadvantages of each will be discussed. The methods of data acquisition will be given as well. Chapter 3 contains details of the observations, descriptions of each cluster studied and a summary of the data reduction process. The results will be presented in Chapter 4 and discussed in Chapter 5, and finally conclusions and a discussion of future work will be given in Chapter 6. The Appendices contain a description of near-infrared

two-colour diagrams and my personal experience with the data reduction process.

Chapter 2

CCD and Infrared Array Photometry

Charge-coupled devices, or CCDs, were introduced to the scientific community about 25 years ago (Boyle and Smith, 1970), and used in astronomical applications five years later. Typical format sizes then were 100 × 100 pixels, and the devices had high read noise and very little sensitivity at short wavelengths. Infrared detectors with sensitivities required for serious astronomical applications have been used for the past 30 years, but it has only been within the past 10 years or so that two-dimensional infrared (IR) arrays have become available. Even though the earliest ones were small (typically 32 × 32, or 58 × 62 pixels), they represented a great improvement over single detectors.

The size and quality of both CCDs and IR array detectors have increased dramatically over the past few years, with format sizes now of 2048 × 2048 pixels, and 1024 × 1024 pixels, for CCDs and IR arrays, respectively. New developments are leading to even larger formats, with greater sensitivities. This chapter describes the operation of CCDs and IR arrays, and similarities and differences in data acquisition. Only brief descriptions will be given here; more details may be found in papers by Janesick and Elliott (1992),

Table 2.1: Wide band optical filters and their FWHM bandwidths (Johnson and Morgan, 1953; Johnson, 1966).

Filter	λ (Å)	$\Delta\lambda$ (Å)
U	3650	680
B	4400	980
V	5500	890
R	7000	2200
I	9000	2400

and Joyce (1992).

2.1 CCD Detectors

CCD chips are constructed primarily of silicon (Si), with several closely-spaced capacitors forming a two-dimensional array of pixels (picture elements). Due to the nature of Si, CCDs are sensitive to radiation over a wide range of wavelengths; typical optical observations are performed from 3800 to 9000 Å(see Table 2.1 for peak wavelengths and bandwidths of the standard optical broadband filters), but reasonable quantum efficiencies are demonstrated for soft x-ray (100 Å) and near-infrared (11,000 Å) radiation for some CCDs (Janesick and Elliott, 1992).

CCD detectors operate and are read out as follows (refer to Figures 2.1 and 2.2). Charge creation is governed by the photoelectric effect: during an exposure, photons striking the Si atoms liberate electrons. When a positive voltage is applied to the pixels, potential wells are formed at the pixel surfaces which are capable of accumulating the electrons, which shall be referred to as a packet. After the exposure is completed, the CCD is read out. During this stage, the voltage on the pixels is manipulated such that rows

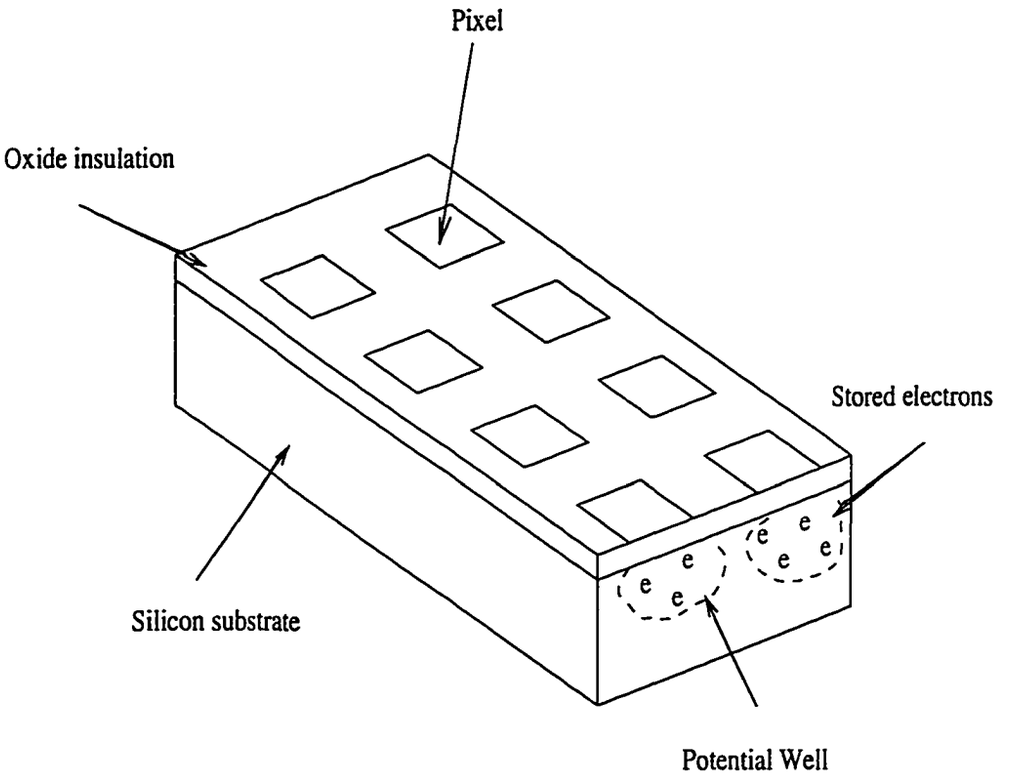

Figure 2.1: Schematic diagram of a CCD. Shown are the electrodes (pixels), insulating material which shields the electrodes from the silicon substrate, and the potential well with accumulated charge. Note that this diagram is not to scale. In an actual CCD, the pixel spacings are much smaller relative to the pixel size.

of accumulated electrons are transfered via parallel registers to the serial register at one edge of the CCD. This register transports the packets to an on-chip amplifier, which converts them to an output voltage. This voltage is amplified again, converted to a digital signal, and stored. The stored image may be displayed at any time on a computer monitor. CCD detectors have a high quantum efficiency, large dynamic range, are linear over a wide range, and have relatively low noise.

There are several processing steps to which a digitised image, hereafter referred to as a frame, must be subjected before it can be used in analysis. An additive background known as the bias must be subtracted from every frame taken. This quantity, a small positive voltage deliberately added to the true CCD signal, is what the whole chip would record in a zero second exposure, and has a stationary pattern that is repeated for each readout. In practice, several such readouts are taken and averaged together, the result of which is subtracted from all data frames. The overscan region of the CCD, which is not actually a physical part of the chip, consists of a few virtual columns at the edge of the CCD opposite from the on-chip amplifier. It provides a measure of the electronics bias level that physically indicates zero photons counted. Usually, a mean level is determined and subtracted from all data frames (including the bias frames).

Two quantities affecting the noise are the read noise and dark current. The read noise is produced by the entire analog signal chain, which includes the chip itself, the on-chip amplifier, the secondary amplifier and the analog-to-digital converter. The dark current arises from thermally created electrons. Its effect increases proportionately with exposure time and is sensitive to the CCD temperature. Thus, cooling the chip and surroundings decreases the dark current (often to a negligible level).

Small structural variations exist on the CCD chip, which lead to pixel-

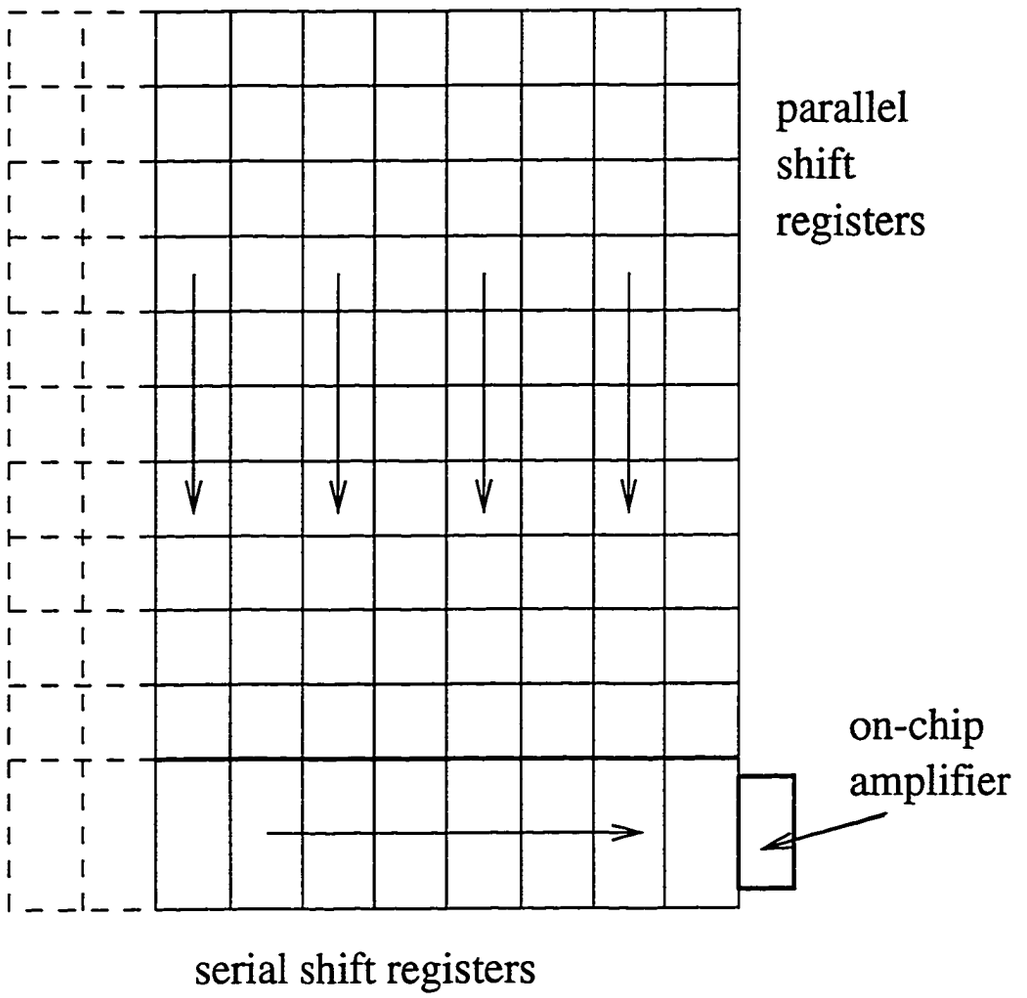

Figure 2.2: Schematic diagram illustrating charge transfer during readout. Also shown is the overscan region, indicated by the dashed line. Note that this region is not a physical part of the chip.

to-pixel variations in quantum efficiency. In addition, the telescope optics introduce large-scale patterns which occur as a result of spatially nonuniform illumination of the CCD. In order to correct for this, a calibration frame (called a flat-field) must be produced and divided into each image. Flat-field frames are obtained by exposing the CCD to a uniformly illuminated surface (such as a lamp and screen, or the twilight sky) and scaling the mean exposure level to 1.0 ADU (analogue to digital units). In the case of twilight flats several frames, shifted slightly from exposure to exposure, are taken in each bandpass and median-combined (the median of the exposure levels on a pixel-by-pixel basis for the set of frames is taken). This process removes any stars which may have become visible during twilight.

2.2 IR Array Detectors

Near-infrared astronomy covers wavelengths from about 1 to 2.2 μm. The Earth's atmosphere produces strong absorption bands due to water and carbon dioxide (see Figure 2.3). However there are a few transparent "windows" remaining, in which have been located the standard photometric bands – J, H and K (Johnson, 1965; Glass, 1974). Problems associated with contamination in the H filter due to a water vapour band at 1.9 μm may arise and make it very difficult to obtain good photometry. This will be discussed in more detail in a subsequent chapter.

Table 2.2 lists these bands and their wavelengths. Note that an additional passband, K', has been included. Recall that this filter has its peak wavelength slightly blueward of that of K, yet still within the same atmospheric window. As a result, the thermal component of the background is lower, and the background surface brightness reduced by up to 0.9 magnitudes arcsec^{-1}. Even though the filter width is narrower, the gain in reduced

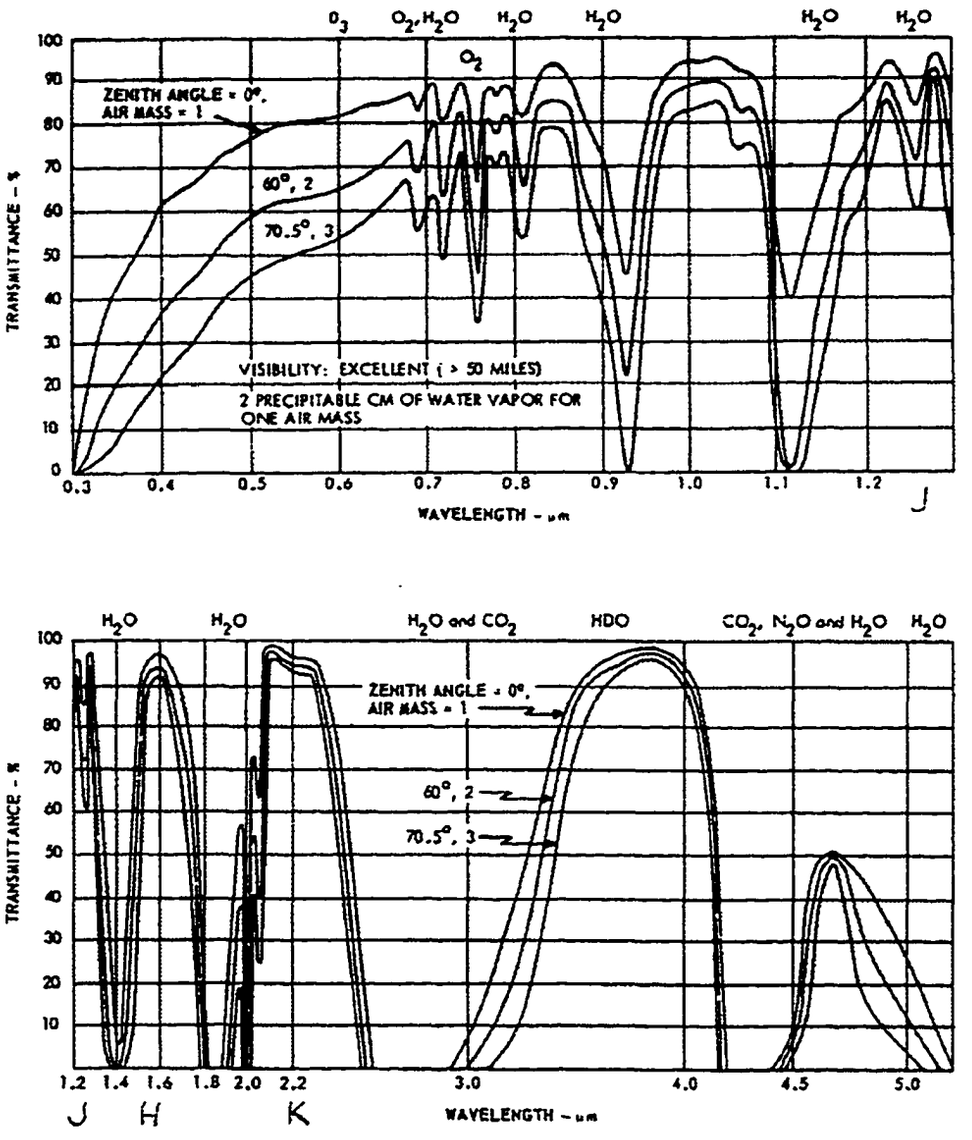

Figure 2.3: Atmospheric transmittance, in percent, as a function of wavelength in μm. This figure illustrates the absorption bands due to water vapour (and other substances) in the earth's atmosphere. Placement of the J, H and K filters is indicated. From the RCA Electro-Optics Handbook (1974).

Table 2.2: Near-infrared filters and their nominal peak wavelengths and bandwidths.

Filter	λ (μm)	$\Delta\lambda$ (Å)
J	1.25	3000
H	1.65	3000
K	2.2	4000
K'	2.12	3400

background yields deeper imaging capabilities in the same integration time (Wainscoat and Cowie, 1992).

The methods of observing with IR arrays in the wavelength interval 1 – 2.5 μm are similar to CCDs, but the construction and actual operation are different. For example, the chips are made of material combinations such as platinum silicide (PtSi), indium antimonide (InSb), mercury cadmium telluride (HgCdTe), or silicon doped with indium, gallium, or arsenic, rather than pure silicon. Each material has different properties useful for different applications. A PtSi chip was used in the present work. These chips are inexpensive as compared to the InSb or HgCdTe ones, but suffer from low quantum efficiency [8-10% for the infrared wavelength range considered here, according to Perry (1992)].

Since the energy gap between the valence and conduction bands for IR arrays is smaller than that for CCDs, electrons can be excited into the conduction band not only by photons but by thermal energy, so the operating temperatures have to be much lower (30-80 K for the IR arrays, as opposed to 150-170 K for CCDs). Since the thermal energy arises from the electronics as well as the ambient environment, the chip must be shielded in order to admit only the solid angle subtended by the telescope optics.

IR detectors are not constructed as shift registers like CCDs since the

materials from which they are made do not function well enough at low temperatures. Thus, the array is actually a hybrid, formed by aligning and joining a detector array and a readout array. The interface between the two is formed by small bumps of indium metal. An advantage of this device is that blooming, which occurs when the potential well of a pixel saturates and causes charge to spill over to neighbouring pixels, does not occur since each pixel is separate and thus no charge transfer from one pixel to another occurs.

As in CCDs, each pixel in the detector array can be considered a capacitor which, when biased towards a preset voltage, acts as a potential well for collecting electrons produced by photons absorbed in the chip material. However, readout takes place via a different process. The readout array measures the voltage on each pixel, which is related to the number of electrons. This readout process is nondestructive, so it can be carried out at any time without affecting the charge on the pixels.

2.3 Differences in Observing Techniques

Most of the differences between the two types of detectors described above are hidden in the electronics, so the actual operation of the detectors is similar, with a few exceptions. For example, IR arrays have a higher dark current, which may or may not be linear with integration time, so one must take a "dark frame" for every integration time used on the program objects. IR arrays also have a higher read noise, so techniques such as performing multiple readouts and averaging several exposures together are employed to reduce the problem.

Since the sky brightness is greater in the infrared than at optical wavelengths (from Joyce (1992), $V_{sky} \sim 22$ mag square arcsec^{-1}, while $K_{sky} \sim 13$

mag square arcsec^{-1}), exposures are sky-limited. This enhancement comes from thermal emission from the telescope optics and optically thick telluric absorption lines longward of 2.2μm, as well as airglow (OH and O_2 molecules in the atmosphere excited by solar radiation during the day), which varies both spatially and temporally, especially at dusk.

The sky variability described above necessitates a different process for the production of IR flat-field frames. Whereas a single set of flat-field frames are taken with CCDs, it is necessary to use the IR data frames themselves to construct flat-fields. In this process, a series of frames (usually 3 or 5) of the object in question is taken, with each frame shifted slightly (a few tens of arcseconds) from the others (this process is referred to as "dithering"). The frames are normalized to a mean of 1, and median-combined, which removes stars. The resulting flat-field is divided into each program frame for that particular field. In certain cases, this procedure is not enough to achieve a uniformly flat final image. Additional steps, which will be detailed in a subsequent chapter, must be taken to construct an "extra-flat-field" frame.

Chapter 3

Observations and Data Reduction

3.1 Observational Details

All the observations were obtained at the Dominion Astrophysical Observatory (DAO) with the 1.8 m Plaskett telescope. The infrared observations for all four clusters were obtained with the 256x256 pixel PtSi near-infrared array detector, and J, H and K' filters. The detector has 40μm square pixels, and an image scale of 0.66 arcsec pixel^{-1}, yielding a field 2.8 arcmin on a side. The optical observations were obtained using three different CCDs. The Tek 2 CCD chip (1024x1024 pixel), used to obtain the optical observations for NGC 2141, had an image scale of 0.53 arcsec pixel^{-1}, which resulted in a 9x9 square arcmin field. The 1024x1024 pixel Site-1 chip, which replaced the Tek 2, has an image scale of 0.55 arcsec pixel^{-1}. It was used for the observations of NGC 6819 and NGC 7142. Both CCD chips are thin, with pixel sizes of 24μm. Garnavich et al. (1994), who obtained the optical observations for NGC 6791, used a thick Ford Aerospace 2048x2048 pixel CCD chip binned on readout to 1024^2 pixels (pixel size 15μm). This yielded an image scale of 0.68 arcsec pixel^{-1}, 11.6 arcmin on a side. V and I (and B for NGC 6819 only)

filters were used for all observations. Note that the I filter is in the Johnson (1953) system. The choice of filters was governed by the availability of good quality, pre-existing data in other passbands, as well as time constraints (if clear skies were assured only for part of the night, only two filters were used, for example). Tables 3.1, 3.3, 3.5 and 3.8 list the optical and near-infrared program frames. The tables contain the cluster regions observed, the filters used, the exposure times in seconds and the air masses at which the fields were observed.

Several Landolt (1992) standards were observed in conjunction with the optical observations of all four clusters (Tables 3.2, 3.4 and 3.6). Fields in the globular clusters M3 and M92 containing standards (Stetson and Harris, 1988) were used to supplement the standard star observations for NGC 2141 and NGC 7142, respectively. I [Kron-Cousins system – Kron et al. (1953), and Cousins (1976)] band photometry for M92 was supplied by Stetson (private communication), while a transformation from $(B-V)$ to $(V-I)$ for the M3 data was effected using a statistical relation, based on high-quality standard star observations, derived by Caldwell et al. (1993). JHK standard stars taken from Elias et al. (1982) were observed on the nights the clusters were observed with the IR camera (Tables 3.2, 3.4, 3.7 and 3.8).

The optical images were bias-subtracted and flat-fielded using bias frames taken during the night, and sky flats taken during twilight and dawn. The near-infrared images were dark-subtracted using dark frames taken during the night, and flat-fielded using flats constructed by median-combining the slightly offset data frames (to remove stars). It was found that at least 5 frames were needed for a good flat-field frame, and applying a 1-sigma clipping algorithm to the frames before combining helped in reducing the number of residual images that may remain after median combination. The

flat-fielded frames were aligned and averaged to produce the final images. Note that since this procedure reduces the area covered and causes stars on the edges of the frames to be lost, the long-exposure individual frames, as well as the averaged ones, were photometered. The magnitudes of the stars on the edges of the individual frames were added to the averaged frames' photometry lists to increase the total number of observations.

In some cases, an additional flat-fielding process was required for the infrared data to correct for residual variations which appeared after the images were flattened via the method described above. A residual flat-field frame was created as follows: a line of form $y = mx + b$ was fit to the columns of the preliminary flat-fielded images. Next, the rows were fit by a straight line, producing images which were regarded as templates of the large-scale background variation. The templates for each field were averaged, normalized to 1, and divided into the preliminary flat-fielded images. This procedure produced final, flat-fielded images with more uniform backgrounds.

Several points regarding the reduction of the data for some of the clusters merit discussion:

NGC 2141

The long-exposure I frames of this cluster exhibited fringe effects at the 0.5–1% level. Subtraction of a fringe frame constructed from exposures of sparsely populated regions of the sky removed the fringes, but increased the overall noise level in the sky background to values greater than the noise produced by the fringes themselves. As a check on the accuracy of the photometry, a corrected frame was compared with its uncorrected counterpart. The photometric errors for the fringe-corrected frame's stars were slightly higher ($\delta V \sim 0.005$ at $V \sim 14$) than those for the uncorrected frame, and

became worse for fainter magnitudes (as would be expected for a noisy background). However, a key point is which *magnitudes* are more nearly correct? Even though the noise and therefore the photometric errors are higher in the corrected frame, those faint magnitudes may be more appropriate simply because the background is more uniform. As a test, 100 artificial stars generated from the frame's point-spread-function (PSF, see Section 3.2) were added to the original and the corrected images. Photometry was performed on each new frame, and the results compared to the input magnitudes. The average magnitude difference between stars on the corrected frame was 0.014 ± 0.175 (82 stars recovered), while the average difference for the uncorrected frame was 0.027 ± 0.153 (83 stars). The uncertainties are so large that the difference between the above averages is negligible. As a final check, a plot of the uncorrected versus corrected frames' magnitudes for the real stars was made, which yielded a straight slope and no noticeable difference. Since subtraction of a fringe frame did not substantially improve the results, the uncorrected frames were used in subsequent analyses.

NGC 7142

The seeing on one of the optical observing nights was poor ($\geq$ 3 arcsec), which made it difficult to focus the telescope properly. As a result, several images were out-of-focus. Difficulties arose when photometry was performed on the images. Subtraction of the PSF resulted in residuals exhibiting black central holes at the positions of the stars, surrounded by bright rings. The reason for this is as follows. The PSF consists of an analytical function (such as a Gaussian) as a first approximation and a table of residuals from the best-fitting function to the actual observed brightness values within the average profile of several bright, uncrowded stars in the image. If the stellar

profile has a dip in the centre, then any point along the edge of the dip may be used by the program as the centre of the profile. Thus the true centre of the profile (in the middle of the dip) is never used, and the table of residuals does not reproduce the deviations from the analytical function.

To circumvent the problem, the poorest images were binned, either by 2 or 4 pixels, in order to produce frames which contained stars having a central peak in the radial profile. Note that this process results in magnitudes which are "out" by $2.5\log(n)$, where n is the total number of pixels that have been binned. For the 4×4 binning case, this results in a magnitude correction factor of 3.01.

NGC 6819

The one clear night of observation for this cluster had seeing of less than 2 arcsec. However, telescope tracking problems led to stellar images which were elongated in the east-west direction. Some of the problems were alleviated by restricting the exposure times to less than 100 seconds, but the problem was great enough to necessitate the use of a Moffatt function as the analytical first approximation to the PSF, rather than the usual Gaussian (the Moffatt function has three free parameters – the half-width-at-half-maximum for both x and y, and a position angle for the major axis of the ellipse. The last parameter was required in this case since the east-west direction was oriented about 10 degrees off the x axis). In addition, several stars were being rejected by the finding algorithm, so a parameter which was designed to screen out elongated objects in the image (such as bad rows and columns) was adjusted to accommodate the stellar images.

Table 3.1: NGC 2141 observations: optical – February 1, 1994; near-infrared – January 16, 1995. Given are the observed fields, filters used, exposure times in seconds and airmass.

Field	Filter	Exp	X	Field	Filter	Exp	X
centre	V	60	1.529	centre	J	60	1.346
centre	V	600	1.495	centre	J	180	1.343
centre	I	600	1.478	centre	H	60	1.337
centre	I	60	1.441	centre	H	180	1.335
centre	I	60	1.433	centre	K'	30	1.328
centre	I	600	1.425	north	J	60	1.285
centre	V	600	1.394	north	J	180	1.284
centre	V	60	1.367	north	H	60	1.279
southwest	V	60	1.359	north	H	180	1.278
southwest	V	600	1.355	north	K'	30	1.281
southwest	I	600	1.333	south	J	60	1.277
southwest	I	60	1.314	south	J	180	1.275
southeast	I	60	1.312	south	H	60	1.277
southeast	I	600	1.296	south	H	180	1.275
southeast	V	600	1.295	south	K'	30	1.280
southeast	V	60	1.285	west	J	60	1.312
northeast	V	60	1.279	west	J	180	1.314
northeast	V	600	1.270	west	H	60	1.319
northeast	I	600	1.270	west	H	180	1.321
northeast	I	60	1.269	west	K'	30	1.326
northwest	I	60	1.268				
northwest	I	600	1.268				
northwest	V	600	1.271				
northwest	V	60	1.274				

Table 3.2: NGC 2141 - Optical and near-infrared primary and M3 secondary standards as described in the text. Column headings include identification, filter, exposure time in seconds and airmass.

ID	Filter	Exp	X	ID	Filter	Exp	X
PG0220+132	*V*	60	1.234	M3	*V*	420	1.091
PG0220+132	*I*	60	1.237	M3	*V*	60	1.084
PG0220+132	*I*	60	1.239	M3	*V*	60	1.082
PG0220+132	*V*	60	1.241	M3	*V*	420	1.081
PG0231+051	*V*	60	1.395	M3	*I*	420	1.076
PG0231+051	*I*	60	1.398	M3	*I*	60	1.072
PG0231+051	*I*	60	1.400				
PG0231+051	*V*	60	1.404	HD 18881	*J*	20	1.042
PG0918+029	*I*	60	1.440	HD 225023	*J*	20	1.362
PG0918+029	*V*	60	1.443	Gl 105.5	*J*	20	1.571
RU 149	*V*	60	1.930	HD 18881	*H*	20	1.042
RU 149	*I*	60	1.945	HD 225023	*H*	20	1.366
M3	*V*	60	1.129	Gl 105.5	*H*	20	1.573
M3	*V*	420	1.124	HD 18881	*K'*	30	1.043
M3	*I*	60	1.113	HD 225023	*K'*	30	1.368
M3	*I*	420	1.109	Gl 105.5	*K'*	30	1.575
M3	*I*	420	1.100				
M3	*I*	60	1.093				

Table 3.3: NGC 6819 observations: optical – June 27, 1994; near-infrared – August 24, 1995. Column headings as in Table 3.1.

Field	Filter	Exp	X	Field	Filter	Exp	X
south	B	60	1.061	centre	J	3×200	1.014
south	B	3×200	1.046	centre	H	3×60	1.013
south	V	60	1.035	centre	H	3×200	1.015
south	V	3×200	1.032	centre	K'	30×15	1.013
south	I	10	1.020	north	J	3×60	1.097
south	I	5	1.019	north	J	3×200	1.099
south	I	60	1.018	north	H	3×60	1.104
northeast	B	60	1.012	north	H	3×200	1.107
northeast	B	200	1.012	north	K'	30×15	1.112
northeast	V	30	1.013	northeast	J	3×60	1.250
northeast	V	2×100	1.014	northeast	J	3×200	1.275
northeast	I	5	1.020	northeast	H	3×60	1.292
northeast	I	2×60	1.021	northeast	H	3×200	1.299
centre	J	3×60	1.012	northeast	K'	30×15	1.312

3.2 Photometry and Reduction to a Standard System

PSF, or point-spread-function, photometry was performed on the images using DAOPHOT and ALLSTAR (Stetson, 1987). The basic principle is as follows. All the stellar objects in an image have the same form, and differ from one another only by a scaling ratio. By fitting a PSF to the stellar images, one obtains magnitudes via the equation $m = zpt - 2.5\log(\text{scaling ratio})$, where zpt is the magnitude of the PSF, determined within some fixed aperture.

A very brief description of the photometry process is given below; a full description may be found in Stetson's (1987) paper. First, the stellar images were located above a certain specified threshold by convolving the image with a lowered truncated Gaussian function having a user-specified full-width-half-

Table 3.4: NGC6819 optical and near-infrared standard stars as described in the text. Column headings as in Table 3.2.

ID	Filter	Exp	X	ID	Filter	Exp	X
SA61228	*B*	10	1.073	SA112805	*V*	30	1.503
SA61225	*B*	10	1.073	SA61228	*I*	30	1.066
SA107544	*B*	10	1.563	SA107544	*I*	2	1.587
SA109231	*B*	15	1.565	SA109381	*I*	20	1.522
SA10971	*B*	40	1.539	SA109537	*I*	2	1.520
SA109381	*B*	40	1.539	SA61225	*I*	5	1.178
SA109381	*B*	40	1.525	SA61228	*I*	5	1.178
SA10971	*B*	40	1.525	SA61228	*I*	8	1.555
SA109537	*B*	40	1.522	SA61225	*I*	8	1.555
SA61228	*B*	40	1.161	SA1121242	*I*	1	1.497
SA61225	*B*	40	1.161	SA112275	*I*	1	1.506
SA1121242	*B*	10	1.497	SA112250	*I*	1	1.506
SA112275	*B*	20	1.506	SA112805	*I*	30	1.505
SA112250	*B*	20	1.506				
SA112822	*B*	40	1.503	HD 203856	*J*	10	1.181
SA112805	*B*	40	1.503	HD 162208	*J*	10	1.038
SA61228	*V*	30	1.067	HD 201941	*J*	10	1.616
SA107544	*V*	1	1.567	Gl 748	*J*	10	1.438
SA109231	*V*	3	1.559	HD 18881	*J*	10	1.183
SA10971	*V*	25	1.536	HD 203856	*H*	10	1.178
SA109381	*V*	25	1.536	HD 162208	*H*	10	1.038
SA109381	*V*	25	1.524	HD 201941	*H*	10	1.614
SA10971	*V*	25	1.524	Gl 748	*H*	10	1.438
SA109537	*V*	5	1.520	HD 18881	*H*	10	1.180
SA61225	*V*	15	1.168	HD 203856	K'	15	1.176
SA1121242	*V*	2	1.497	HD 162208	K'	15	1.042
SA112275	*V*	3	1.506	HD 201941	K'	15	1.612
SA112250	*V*	3	1.506	Gl 748	K'	15	1.439
SA112822	*V*	30	1.503	HD 18881	K'	15	1.179

Table 3.5: NGC 7142 observations: optical – October 14 and 15, 1994; near-infrared – August 1, 25, 28, September 21, 22, 1993. Column headings as in Table 3.1.

Field	Filter	Exp	X	Field	Filter	Exp	X
east	*V*	3×200	1.055	G421	*J*	3×30	1.047
east	*I*	30	1.050	G421	*J*	3×180	1.047
east	*I*	3×100	1.049	G421	*H*	3×30	1.047
centre	*V*	3×200	1.049	G421	*H*	3×180	1.047
centre	*I*	3×100	1.055	G421	*K'*	45×20	1.047
centre	*I*	3×60	1.080	G160	*J*	3×30	1.065
west	*V*	5×60	1.169	G160	*J*	3×180	1.066
west	*I*	5×30	1.193	G160	*H*	3×30	1.057
west	*I*	5×60	1.208	G160	*H*	3×180	1.063
southwest	*V*	5×60	1.106	G160	*K'*	45×20	1.069
southwest	*V*	3×200	1.113	G93	*J*	3×30	1.120
southwest	*I*	4×60	1.131	G93	*J*	3×180	1.121
southwest	*I*	5×30	1.142	G93	*H*	3×30	1.116
southeast	*V*	5×60	1.163	G93	*H*	3×180	1.117
southeast	*V*	3×200	1.178	G93	*K'*	45×20	1.125
southeast	*I*	5×30	1.199	G51	*J*	3×30	1.049
southeast	*I*	5×60	1.212	G51	*J*	3×180	1.049
blank	*V*	3×60	1.233	G51	*H*	3×30	1.049
blank	*V*	3×200	1.244	G51	*H*	3×180	1.049
blank	*I*	3×60	1.270	G51	*K'*	45×20	1.048
blank	*I*	2×200	1.283	G342	*J*	3×30	1.052
				G342	*J*	3×180	1.052
G170	*J*	3×180	1.051	G342	*H*	3×30	1.051
G170	*H*	3×180	1.052	G342	*H*	3×180	1.051
G170	*K'*	30×20	1.053	G342	*K'*	45×20	1.053
G196	*J*	3×180	1.209				
G196	*H*	2×180	1.215				
G196	*K'*	30×20	1.221				

Table 3.6: NGC 7142 optical primary standard star observations as described in the text. Column headings as in Table 3.2.

ID	Filter	Exp	X	ID	Filter	Exp	X
SA1111965	*V*	30	1.502	SA95100	*V*	60	1.541
M92 4	*V*	200	1.378	SA95101	*V*	60	1.541
M92 17	*V*	200	1.378	SA9598	*V*	60	1.541
M92 35	*V*	200	1.378	SA9621	*V*	60	1.626
M92 14	*V*	200	1.378	SA97351	*V*	20	1.772
M92 10	*V*	200	1.378	SA97351	*I*	20	1.762
M92 91	*V*	200	1.378	SA98646	*I*	60	1.519
PG0231+051	*V*	60	1.377	SA98626	*I*	60	1.519
F22	*V*	60	1.373	SA98650	*I*	60	1.519
SA9542	*V*	60	1.565	SA98624	*I*	60	1.519
SA9543	*V*	60	1.565	M92 4	*I*	100	1.397
SA98626	*V*	60	1.522	M92 14	*I*	100	1.397
SA98650	*V*	60	1.522	M92 10	*I*	100	1.397
SA98627	*V*	60	1.522	PG0231+051	*I*	60	1.374
SA98634	*V*	60	1.522	SA9542	*I*	60	1.548
SA98624	*V*	60	1.522	SA9543	*I*	60	1.548
SA95115	*V*	60	1.565	SA95105	*I*	60	1.548
SA9541	*V*	60	1.565	SA9597	*I*	60	1.529
SA95105	*V*	60	1.565	SA95100	*I*	60	1.529
SA95106	*V*	60	1.565	SA95101	*I*	60	1.529
SA95112	*V*	60	1.565	SA9598	*I*	60	1.529
SA9597	*V*	60	1.541	SA9621	*I*	60	1.606

Table 3.7: NGC 7142 near-infrared standard observations as described in the text. Column headings as in Table 3.2.

ID	Filter	Exp	X	ID	Filter	Exp	X
HD 203856	*J*	10	1.212	Gl 105.5	*H*	10	1.476
HD 22686	*J*	10	1.496	HD 203856	*H*	10	1.012
Gl 748	*J*	10	1.042	HD 225023	*H*	10	1.055
HD 203856	*J*	10	1.042	HD 40336	*H*	10	1.532
HD 1160	*J*	10	1.406	HD 22686	*H*	10	1.475
HD 18881	*J*	10	1.017	HD 225023	*H*	10	1.034
Gl 105.5	*J*	10	1.476	HD 44612	*H*	10	1.037
HD 203856	*J*	10	1.026	HD 203856	*K'*	15	1.206
HD 203856	*J*	10	1.012	HD 22686	*K'*	15	1.499
HD 225023	*J*	10	1.055	Gl 748	*K'*	15	1.445
HD 22686	*J*	10	1.476	HD 203856	*K'*	15	1.043
HD 225023	*J*	10	1.033	HD 1160	*K'*	15	1.407
HD 40336	*J*	10	1.530	HD 18881	*K'*	15	1.018
HD 44612	*J*	10	1.038	HD 203856	*K'*	15	1.027
Gl 748	*J*	10	1.439	Gl 105.5	*K'*	15	1.476
HD 22686	*H*	10	1.497	HD 203856	*K'*	15	1.012
HD 1160	*H*	10	1.406	HD 22686	*K'*	15	1.477
HD 18881	*H*	10	1.017	HD 44612	*K'*	15	1.037
HD 203856	*H*	10	1.026	Gl 748	*K'*	15	1.439

Table 3.8: NGC 6791 near-infrared observations. Column headings as in Table 3.1.

ID	Filter	Exp	X	ID	Filter	Exp	X
R5	J	3×10	1.030	R3	J	3×60	1.033
R5	H	3×10	1.030	R3	H	3×60	1.032
R5	K'	15×10	1.029	R3	K'	33×10	1.031
R4	J	3×10	1.022	R16	J	3×60	1.022
R4	H	3×10	1.022	R16	H	3×60	1.021
R4	K'	15×10	1.022	R16	K'	33×10	1.020
R1	J	3×10	1.018	R24	J	3×120	1.018
R1	H	3×10	1.018	R24	H	3×120	1.018
R1	K'	15×10	1.018	R24	K'	45×10	1.018
R7	J	3×10	1.046	R10	J	3×120	1.026
R7	H	3×10	1.047	R10	H	3×120	1.029
R7	K'	15×10	1.048	R10	K'	45×10	1.031
R14	J	3×30	1.062	R8s	J	3×120	1.055
R14	H	3×30	1.063	R8s	H	3×120	1.062
R14	K'	21×10	1.065	R8s	K'	45×10	1.065
R12	J	3×30	1.115				
R12	H	3×30	1.118	Standards			
R12	K'	21×10	1.120				
R2	J	3×30	1.177	Gl 748	J	10	1.489
R2	H	3×30	1.153	Gl 748	H	10	1.487
R2	K'	21×10	1.156	Gl 748	K'	10	1.486
R8	J	3×60	1.199	HD 1160	J	10	1.404
R8	H	3×60	1.204	HD 1160	H	10	1.403
R8	K'	45×10	1.209	HD 1160	K'	10	1.403
R3	J	3×60	1.298	HD 162208	J	10	1.023
R3	H	3×60	1.304	HD 162208	H	10	1.023
R3	K'	33×10	1.310	HD 162208	K'	10	1.022
R2517	J	3×120	1.276	Gl 748	J	10	1.482
R2517	H	3×120	1.286	Gl 748	H	10	1.481
R2517	K'	45×10	1.294	Gl 748	K'	10	1.480
R19	J	3×120	1.175	HD 162208	J	10	1.021
R19	H	3×120	1.184	HD 162208	H	10	1.021
R19	K'	45×10	1.190	HD 162208	K'	10	1.021
R22	J	3×120	1.107	HD 225023	J	10	1.029
R22	H	3×120	1.111	HD 225023	H	10	1.029
R22	K'	45×10	1.116	HD 225023	K'	10	1.028

maximum (FWHM), and searching for local maxima in brightness enhancement. Any bad pixels (delta functions) or bad rows and columns (elongated x or y enhancements) were weeded out during this process. Next, aperture photometry was performed on, and sky values determined for, each object in the list. A PSF was defined using several bright, uncrowded stars (an iterative process which resulted in the removal of neighbour stars which contaminated the PSF). Finally, the PSF was fit to the entire star list at once, in an iterative fashion. With each iteration, all the stars were subtracted from the image on the basis of the current estimates of position and magnitudes. After examination of the residuals, the estimates of positions and magnitudes were refined, and the subtraction procedure repeated. When the fit between a star and the PSF converged, that is, when the incremental corrections to positions and magnitudes became insignificant, the star was subtracted from the image and hence excluded from subsequent iterations. The process described above produced a file containing raw, instrumental magnitudes.

The subsequent transformation of the raw magnitudes to standard ones involved the application of aperture corrections, followed by transformation coefficients. A set of programs obtained from Stetson (private communication) was used to do this. Aperture corrections must be applied for the following reason. Since DAOPHOT derives relative magnitudes in an aperture of some given size, aperture corrections are required to put the magnitudes onto an absolute scale (by adding the light from the star which is outside the fixed aperture). A simple way to determine the correction involves performing aperture photometry on several bright, uncrowded stars, using a small aperture (the PSF aperture, for example), and a large one (several times the FWHM), and taking the difference. A better procedure

(which was adopted in this work) is to measure the magnitude of these stars through a series of concentric apertures, ranging from small up to very large, and then plot a "growth" curve (the differences in magnitude between adjacent apertures, versus aperture). The average magnitude differences between successive apertures are read from the growth curve and summed from the largest aperture to the smallest to yield cumulative corrections for each of the smaller apertures. The correction corresponding to the magnitude difference between the largest and the PSF radius is applied to all the stars on the frame (see Stetson (1990) for a complete discussion). For the data considered here, typical uncertainties in the average aperture correction per frame ranged from 0.03 to 0.04 mag.

After application of aperture corrections, the stars were cross-identified from filter to filter and frame to frame, and the magnitudes transformed to a standard system. An equation of the form

$$m_{inst} = M_{std} + a_0 + a_1 C_{std} + a_2 X, \tag{3.1}$$

where M_{std} is the standard apparent magnitude, m_{inst} is the instrumental magnitude, C_{std} is the standard colour, and X is the airmass, was used to transform the data to a standard system. In this equation, a_0 is the zeropoint and is a measure of the sensitivity of the CCD/telescope system in that particular bandpass, a_1 is the colour term, which is a measure of how well the instrumental system approximates the standard system. A value of zero indicates the instrumental system matches the standard system perfectly. a_2 is the first order extinction coefficient, which depends on atmospheric transmission, and varies from site to site, as well as night to night. It is different for each filter. Note that in this case, the $i_{\rm Johnson}$ observations were transformed into $I_{\rm Cousins}$ standard magnitudes since Landolt (1992) used a Cousins I filter for his standard star observations.

After determining transformation coefficients using the above equation, the residuals were plotted against various quantities to check for correlations. Also, in the case of NGC 2141, a better transformation was obtained using higher order extinction and colour terms ($a_3 C_{std}^2$ and $a_4 X C_{std}$). It was found that a correlation existed between the residuals and the time of night (denoted by T) for NGC 7142, so an additional term ($a_3 T$) was included in the above equation, and a new solution found. In addition, extinction coefficients for the NGC 7142 October 14 data were fixed since the range in airmass was not enough to facilitate a meaningful transformation. The residuals of the optical and near-infrared standard star observations are presented in Figures 3.1, 3.2, 3.3 and 3.4 (infrared data only). Average standard errors per observation (which accounts for uncertainties in the standard and observed magnitudes, and additional observational scatter caused by fluctuations in detector quantum efficiency, errors in flatfielding the data, and variations in atmospheric transparency during the night, for example) ranged from 0.01 to 0.04. In most cases, the residuals are reasonable, but large ones reflect the observing conditions (variable cloudiness during some observing runs) and choice of standard stars. More discussion on the latter is warranted. Most of Landolt's standard stars are situated near the celestial equator. While they are still accessible from northern observatories, their minimum airmasses recorded at Victoria's latitude may not bracket the program observations. Landolt (1992) provides some standard stars with declinations around 15°, which give a better range in airmass, however it was found after the fact that several of these stars are unsatisfactory. Many of them (the PG stars) are very blue [$(B-V) \sim -0.2$], which requires the inclusion of higher order terms in the transformation equation. In addition, a few others (GD 71, and the RU stars, for example) appear to have anomalous magnitudes or

colours. The problems with these standards stars have been recognised by Balam (private communication) as well.

Stetson's (private communication) set of programs was used to perform the above reductions. Tables 3.9 and 3.10 give the optical and near-infrared transformation coefficients for the clusters NGC 2141, NGC 6819, NGC 6791 and NGC 7142. The coefficients were applied first to a selected set of bright stars which were common to all the frames. These stars then served as local secondary standards which defined the zeropoint for each frame prior to transforming all the stars on the frames. The resulting output file was a list of all found stars on the frames, their magnitude (usually V) and colours, plus errors and various parameters giving goodness-of-fit which allows the user to apply selection criteria to exclude objects such as poorly-defined stars and galaxies.

Specific details of the above reduction process may be found in Appendix B, which include problems encountered, hints on smooth operation of the programs, and sample files to show readers what they should expect upon running the programs.

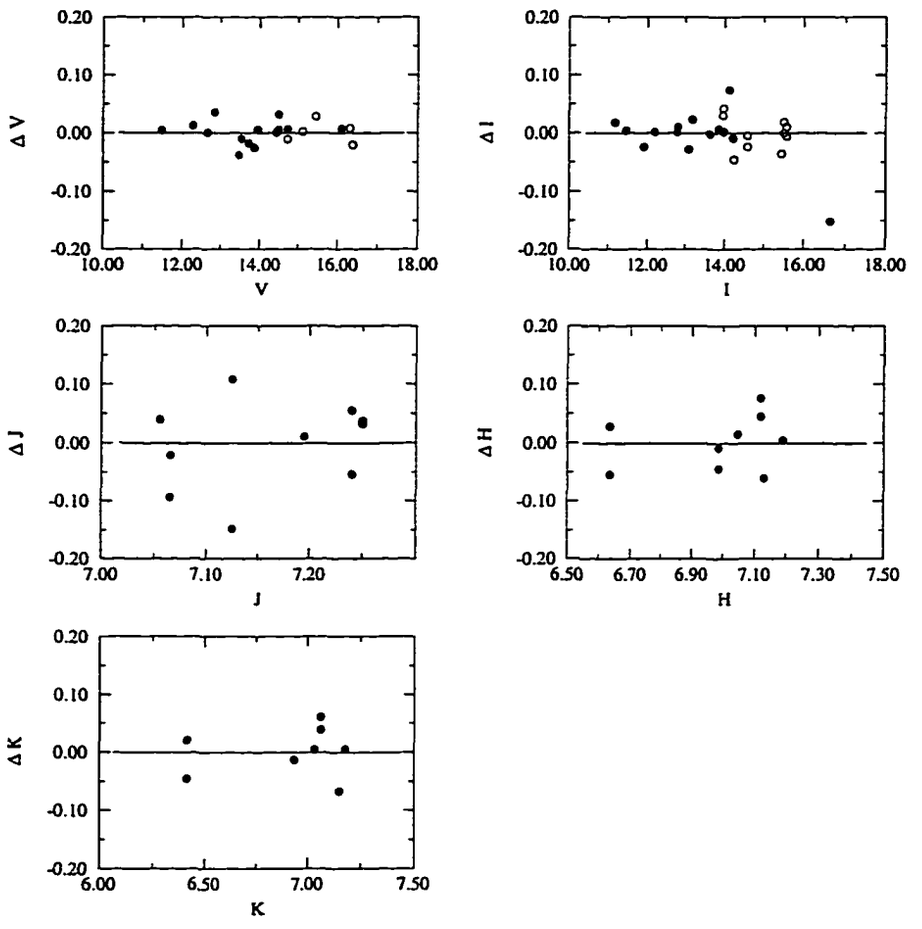

Figure 3.1: Residuals of the optical (VI) and near-infrared (JHK) standard star observations, plotted against standard magnitude, for NGC 2141. Optical Landolt (1992) standards are indicated by filled circles, while M3 secondary standards (Stetson and Harris, 1988) are represented by open circles.

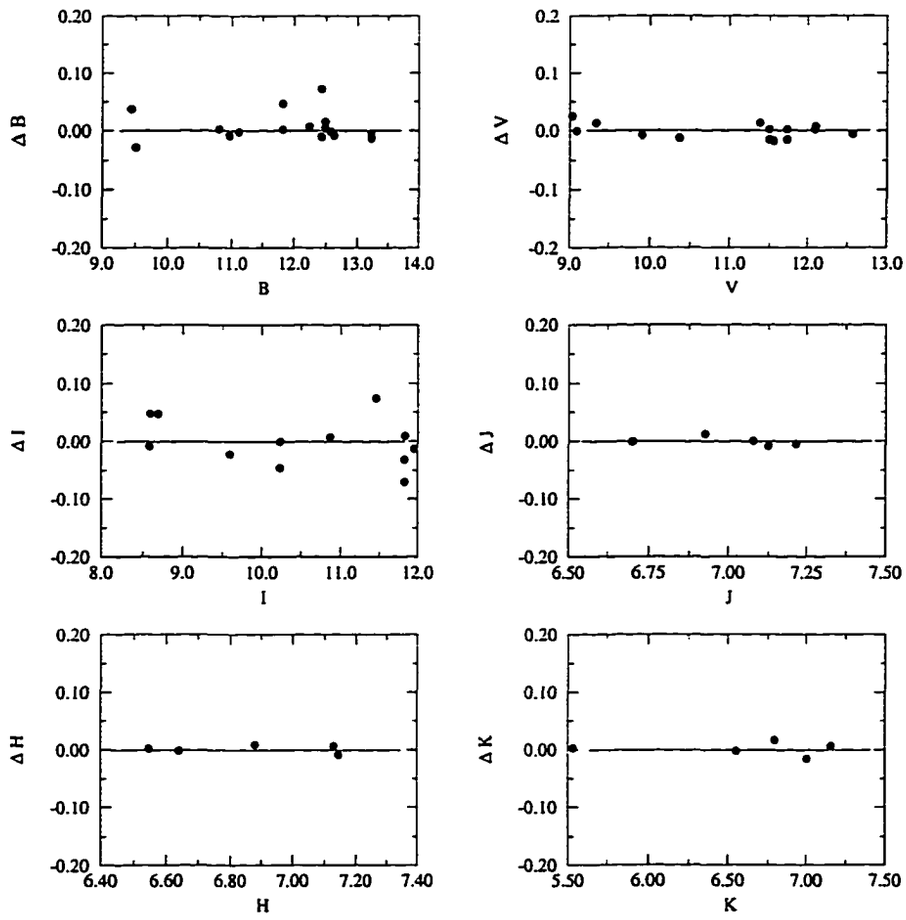

Figure 3.2: Residuals of the optical (BVI) and near-infrared (JHK) standard star observations, plotted against standard magnitude, for NGC 6819.

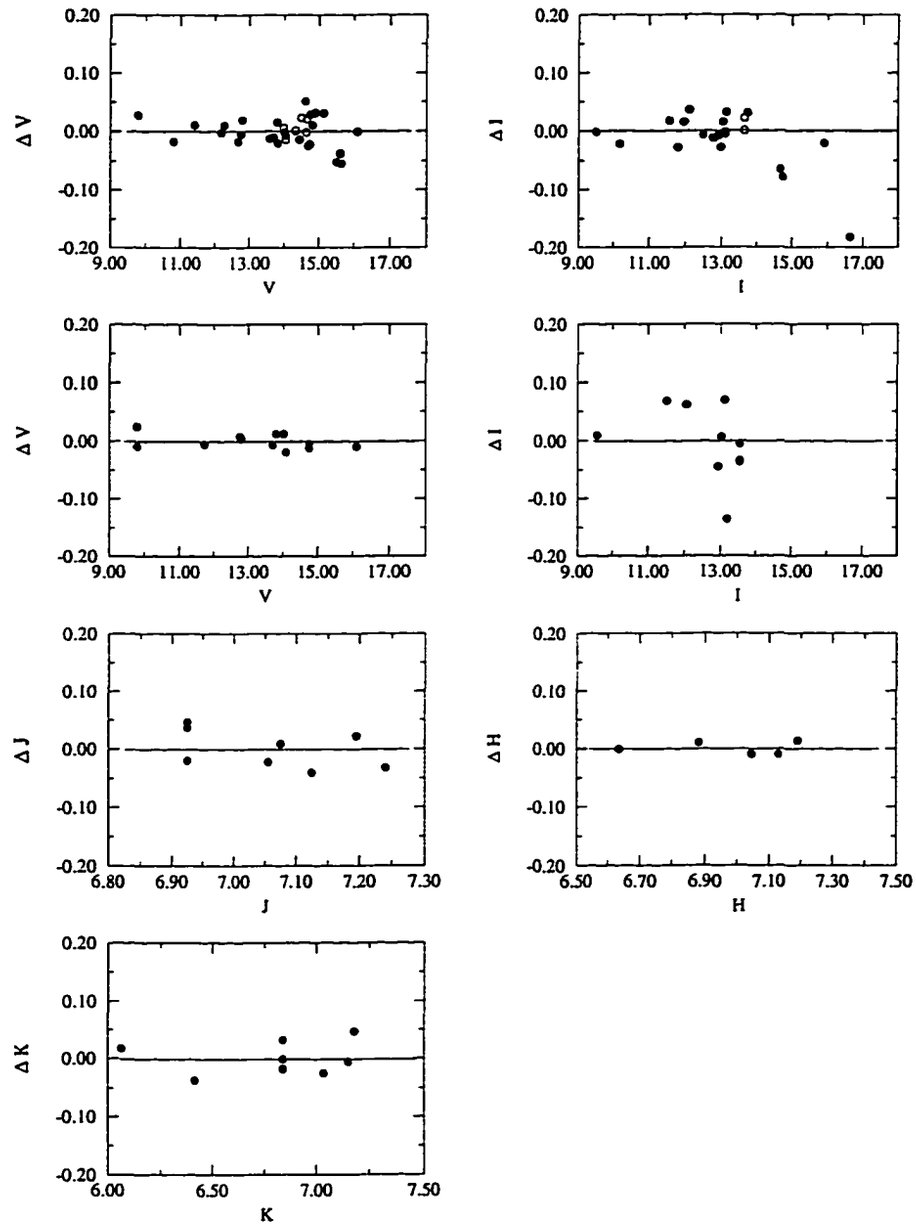

Figure 3.3: Residuals of the optical (VI) and near-infrared (JHK) standard star observations, plotted against standard magnitude, for NGC 7142. Optical Landolt (1992) standards are denoted by filled circles, while M92 secondary standards (Stetson and Harris, 1988) are represented by open circles. The top two and next two figures plot the October 14, and October 15 optical data, respectively.

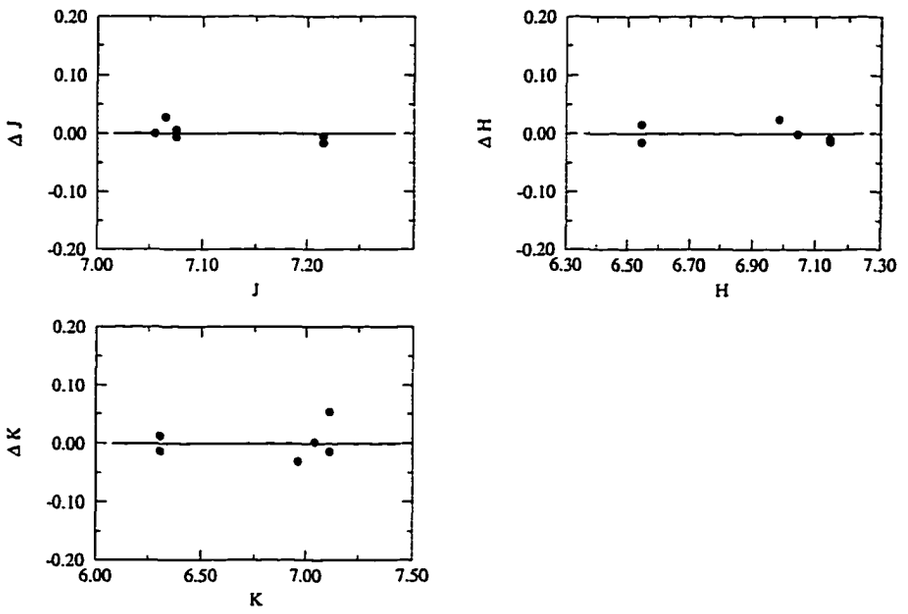

Figure 3.4: Residuals of the near-infrared standard star observations, plotted against standard magnitude, for NGC 6791.

Table 3.9: Transformation coefficients for the optical standard star observations. The equation $m_{inst} = M_{std} + a_0 + a_1 C_{std} + a_2 X$ was used in all cases, with the exception of NGC 2141, which has two additional terms: $a_3 C_{std}^2$ and $a_4 X C_{std}$, and NGC 7142, which has the additional term $a_3 T$ for the October 14 data.

Cluster	Filter		
NGC 2141	B	V	I
	———	$a_0 = 3.12 \pm 0.02$	$a_0 = 3.24 \pm 0.02$
	———	$a_1 = -0.18 \pm 0.02$	$a_1 = -0.17 \pm 0.03$
	———	$a_2 = 0.18 \pm 0.03$	$a_2 = 0.15 \pm 0.04$
	———	$a_3 = 0.11 \pm 0.01$	$a_3 = 0.11 \pm 0.01$
	———	$a_4 = 0.13 \pm 0.04$	$a_4 = 0.16 \pm 0.06$
NGC 6819	B	V	I
	$a_0 = 3.65 \pm 0.01$	$a_0 = 2.90 \pm 0.01$	$a_0 = 3.09 \pm 0.04$
	$a_1 = 0.04 \pm 0.01$	$a_1 = -0.01 \pm 0.01$	$a_1 = -0.03 \pm 0.04$
	$a_2 = 0.27 \pm 0.02$	$a_2 = 0.18 \pm 0.03$	$a_2 = 0.16 \pm 0.08$
NGC 7142	B	V	I
(Oct 14)	———	$a_0 = 2.99 \pm 0.01$	$a_0 = 3.17 \pm 0.03$
	———	$a_1 = 0.002 \pm 0.002$	$a_1 = -0.006 \pm 0.015$
	———	$a_2 = 0.18$ (fixed)	$a_2 = 0.15$ (fixed)
	———	$a_3 = -0.005 \pm 0.001$	$a_3 = -0.004 \pm 0.002$
NGC 7142	B	V	I
(Oct 15)	———	$a_0 = 2.99 \pm 0.01$	$a_0 = 2.98 \pm 0.03$
	———	$a_1 = -0.02 \pm 0.01$	$a_1 = -0.01 \pm 0.05$
	———	$a_2 = 0.14 \pm 0.03$	$a_2 = 0.34 \pm 0.15$

Table 3.10: Transformation coefficients for the near-infrared standard star observations. The equation $m_{inst} = M_{std} + a_0 + a_1 C_{std} + a_2 X$ was used in all cases.

Cluster	Filter		
NGC 6819	J	H	K
	7.65 ± 0.01	$a_0 = 7.95 \pm 0.01$	$a_0 = 9.69 \pm 0.01$
	-0.01 ± 0.03	$a_1 = -0.01 \pm 0.02$	$a_1 = 0.04 \pm 0.03$
	0.13 ± 0.02	$a_2 = 0.08 \pm 0.03$	$a_2 = 0.17 \pm 0.03$
NGC 7142	J	H	K
	7.62 ± 0.02	$a_0 = 7.95 \pm 0.01$	$a_0 = 9.70 \pm 0.02$
	0.03 ± 0.07	$a_1 = -0.17 \pm 0.18$	$a_1 = 0.09 \pm 0.20$
	0.18 ± 0.11	$a_2 = 0.12 \pm 0.05$	$a_2 = 0.20 \pm 0.08$
NGC 6791	J	H	K
	7.62 ± 0.01	$a_0 = 7.89 \pm 0.01$	$a_0 = 9.72 \pm 0.02$
	-0.03 ± 0.02	$a_1 = -0.02 \pm 0.12$	$a_1 = 0.06 \pm 0.20$
	0.21 ± 0.03	$a_2 = 0.13 \pm 0.05$	$a_2 = 0.13 \pm 0.09$
NGC 2141	J	H	K
	7.65 ± 0.04	$a_0 = 7.97 \pm 0.03$	$a_0 = 9.69 \pm 0.02$
	-0.30 ± 0.83	$a_1 = -0.09 \pm 0.54$	$a_1 = -0.18 \pm 0.40$
	0.08 ± 0.19	$a_2 = 0.10 \pm 0.14$	$a_2 = 0.14 \pm 0.11$

Chapter 4

Results

As was discussed in Chapter 1, the study of star clusters provides important details on stellar evolution. CMDs present the observational data in a form suitable for the derivation of a variety of cluster parameters as well as comparison to theoretical models. This chapter contains the results of the photometry which was described in Chapter 3. Section 4.1 presents the various CMDs constructed for each cluster, and discusses field star contamination, and corrections for this effect. Differential and mean cluster reddening values, metallicity determinations found in the literature, and distance modulus calculations are given in Section 4.2. The reader should note that all the photometry files will be available on CD-ROM at the Canadian Astronomy Data Centre, Dominion Astrophysical Observatory, in machine-readable format. Access to the data will be possible via any World Wide Web browser.

4.1 Colour-Magnitude Diagrams

Initially, both optical and near-infrared CMDs were constructed from the data. However, preliminary inspection of the infrared CMDs indicated that there were problems with the H observations which gave unexpected results when the H magnitudes were used in the colours. This is discussed

in Appendix A. Also, it was decided that the $V-K$ colour would be the most useful. Thus, the J and H observations were not used except for the construction of two-colour diagrams, a discussion of which is presented in Appendix A as well.

$(V, V-I)$, $(V, V-K)$ and $(K, V-K)$ CMDs are presented for all four clusters. In addition, a $(V, B-V)$ and an $(I, V-I)$ CMD are given for NGC 6819 and NGC 6791, respectively [note that the data for NGC 6791 have been published by Garnavich et al. (1994)]. All the clusters have been studied previously (see the references in Chapter 1), and all but NGC 2141 have had CMDs constructed from CCD observations available in the literature. However, the observations presented here are the first $(V, V-I)$ and near-infrared ones for these clusters. For clarity's sake, the CMDs constructed from BVI and VK observations will be discussed in separate sections.

4.1.1 Optical CMDs

The $(V, V-I)$ CMD of NGC 2141, shown in Figure 4.1 (Rosvick, 1995), contains 2950 stars in the combined centre, southwest and northwest fields. A well-populated main sequence and subgiant region, and red giant clump are visible. There is a suggestion of a giant branch as well. Even though field star contamination is substantial, several of the stars located above and blueward of the main sequence turnoff may be blue stragglers, cluster members which are believed to be coalesced binary stars, or stars merged by collisions (Leonard, 1996). Typical photometric uncertainties range from 0.01 mag for $V \sim 16$ to 0.1 mag at $V \sim 20$.

This CMD supersedes the photographic one (Burkhead et al., 1972) for several reasons. First, the use of a CCD detector resulted in more accurate magnitudes as well as an increase in the number of stars observed (a few

thousand as opposed to a few hundred). Secondly, the magnitude limit of the new observations is about $V = 20.5$, two magnitudes fainter than the previous study. Even though there is still a fair amount of scatter in the CMD, it may be explained by the presence of field star contamination, differential reddening across the face of the cluster, and a 60-Hz non-repeating noise source (believed to have been caused by faulty wiring) which appeared on some of the images as "short-dashed" rows of bad pixels and is believed to have affected the photometric accuracy.

Artificial star tests were performed to estimate the amount of scatter due to photon noise. Three artificial frames were created from one long exposure V and one long exposure I frame, for a total of six frames. Each of these frames had 150 artificial stars added to it. The data reduction procedure was performed in the same manner as for the real frames, and instrumental CMDs were constructed from the recovered artificial stars and compared to the actual data CMDs. It was found that at faint magnitudes ($v \sim 15$) the artificial star CMD produced a scatter of ~ 0.2 mag, while the real star instrumental CMD showed a scatter of ~ 0.27 mag. This indicates that the excess scatter must be due to the sources described above.

Figures 4.2 and 4.3 display the $(V, B-V)$ and $(V, V-I)$ CMDs of 2179 stars in the south and northeast fields of NGC 6819. A well-defined main sequence extends to at least $V = 18.5$. A giant branch, and red giant clump at $V \sim 13.0$, are visible as well. Most of the giants and clump stars were shown to have membership probabilities greater than 80% in Sanders' (1972) proper motion survey. Several of the blue stragglers located above and blueward of the turnoff were found to be probable proper motion members as well. Typical uncertainties range from 0.008 mag at $V \sim 15$ to 0.04 mag at $V \sim 18$.

Figures 4.4 and 4.5 give the $(V, V-I)$ and $(I, V-I)$ CMDs for NGC 6791 produced by Garnavich et al. (1994). Both CMDs contain 7538 stars, ex-

tend below 20th magnitude, and exhibit well-established subgiant and giant branches. The red giant clump appears at $V \sim 14.5$. Typical uncertainties range from 0.008 mag at $V \sim 17$ to 0.09 mag at $V \sim 21$. The most interesting feature of this CMD is the drooping of the extremely red section of the giant branch (larger symbols), which probably indicates the cluster is metal-rich and old (recall the earlier discussion of the metal-rich globular cluster NGC 6553). This effect is caused by line blanketing at shorter wavelengths, and lessens as the wavelength at which the observations are made increases. These two CMDs and the $(V, V-K)$ one in Figure 4.9 support this claim extremely well. The magnitude range covered by the extreme end of the giant branch in the optical CMDs changes from 1 magnitudes in V to 3 magnitudes in I, while the K magnitude in Figure 4.9 spans 5 magnitudes, illustrating quite effectively that the giant branch becomes more upright as the wavelength of the observations increases.

The optical CMD of NGC 7142 (Figure 4.6) exhibits a fair amount of scatter in the main sequence which may be due to heavy field star contamination, differential reddening and somewhat poor quality data which reflect the partly cloudy observing conditions (attempts to correct for differential reddening and field-star contamination will be discussed in a subsequent section). Typical uncertainties range from 0.01 mag at $V \sim 16$ to 0.15 mag at $V \sim 20$. Artificial star tests for this case showed that at $v \sim 16$, the scatter in the main sequence was 0.1 and 0.2 mag, for the artificial and real CMDs, respectively. A rather scattered giant branch is evident, as are several stars in the region where blue stragglers would be expected to appear. Another interesting feature is the apparent lack of a red giant clump.

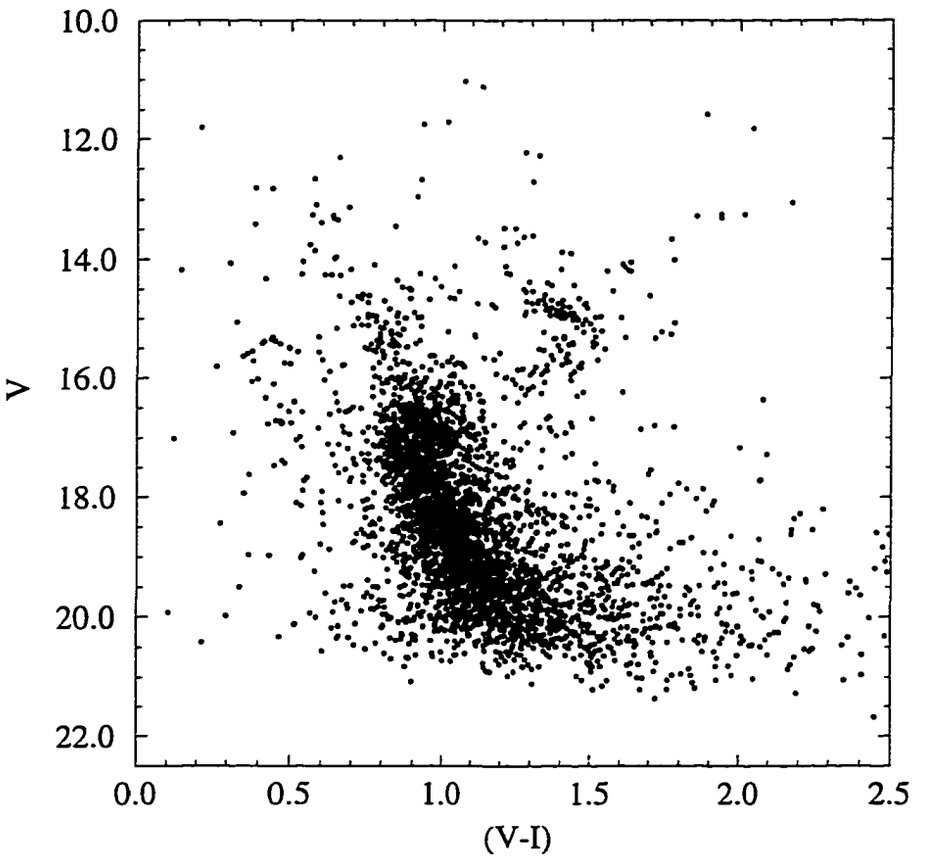

Figure 4.1: $(V, V-I)$ CMD of NGC 2141 containing 2950 stars. Sources for the scatter are discussed in the text.

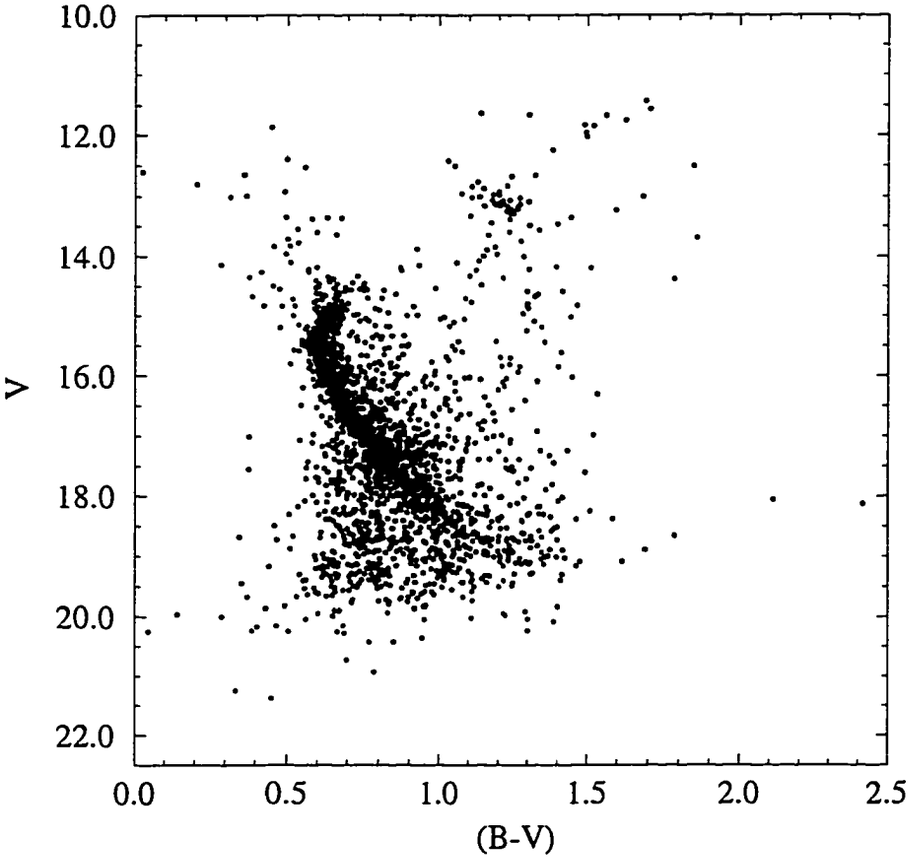

Figure 4.2: $(V, B-V)$ CMD of NGC 6819, containing 2179 stars.

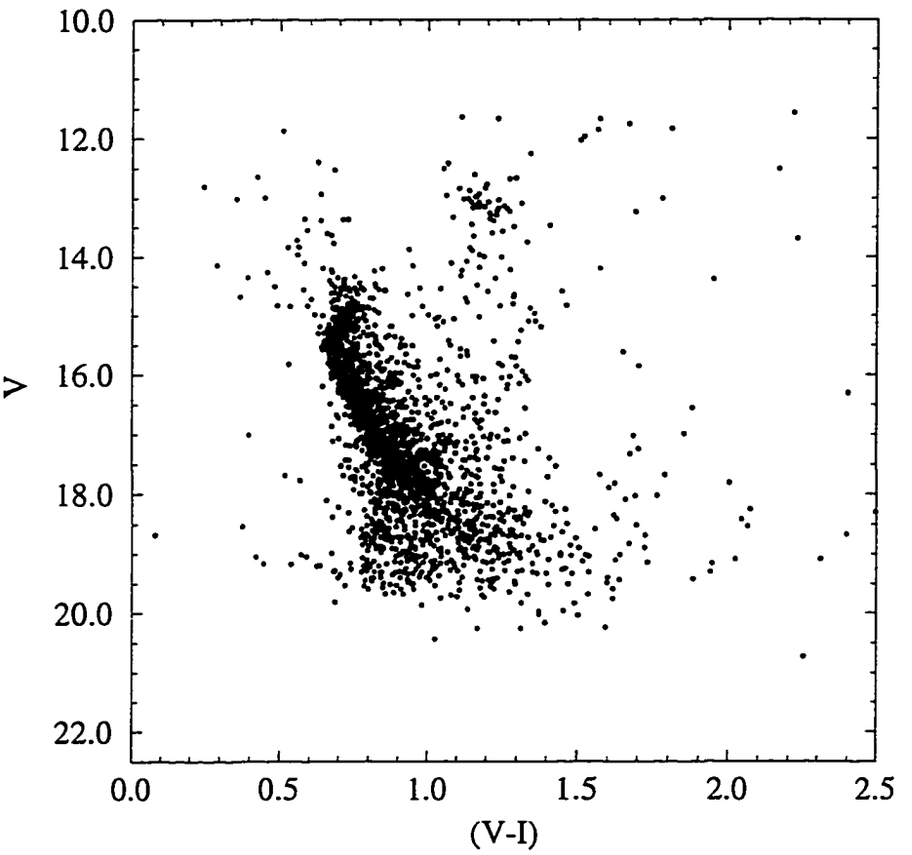

Figure 4.3: $(V, V-I)$ CMD of NGC 6819, containing 2179 stars.

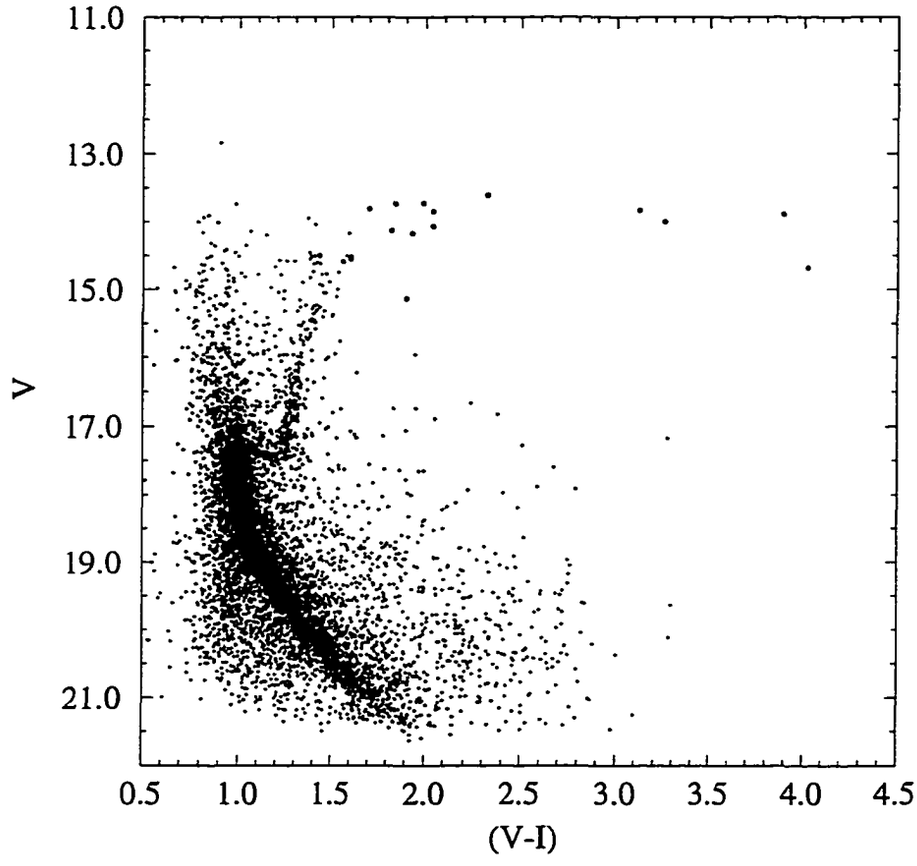

Figure 4.4: $(V, V-I)$ CMD of NGC 6791, containing 7538 stars (Garnavich et al., 1994). This CMD uses larger symbols to emphasize the extreme red end of the giant branch.

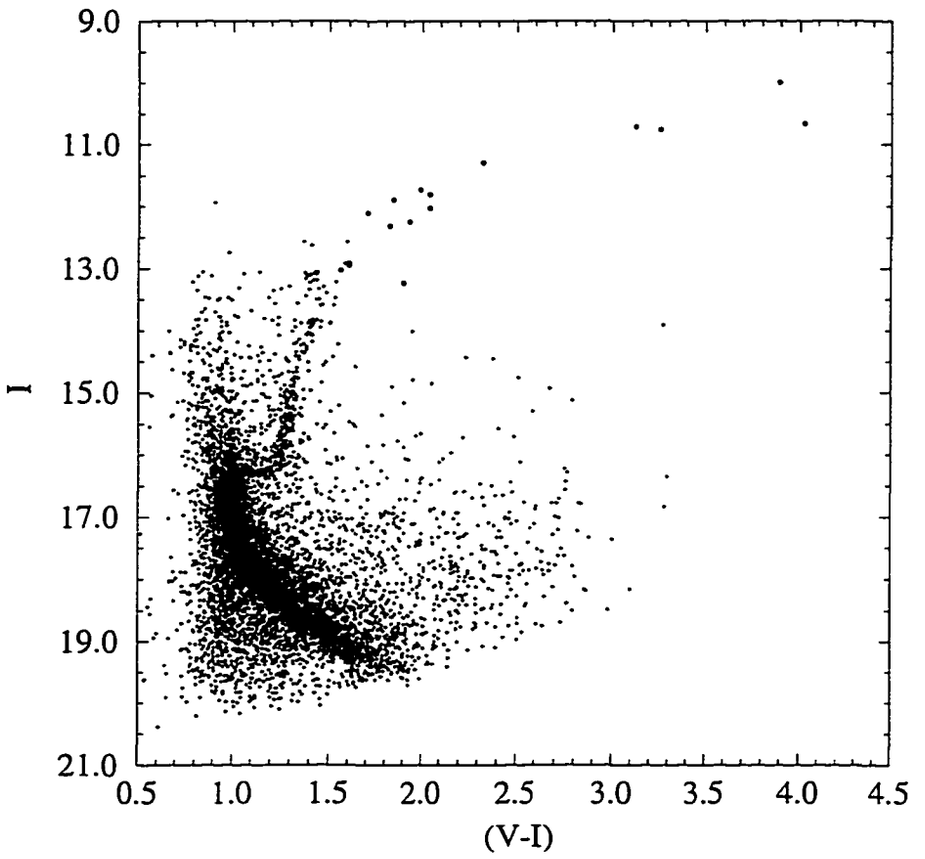

Figure 4.5: $(I, V-I)$ CMD of NGC 6791 (Garnavich et al., 1994). This CMD uses larger symbols to emphasize the extreme red end of the giant branch.

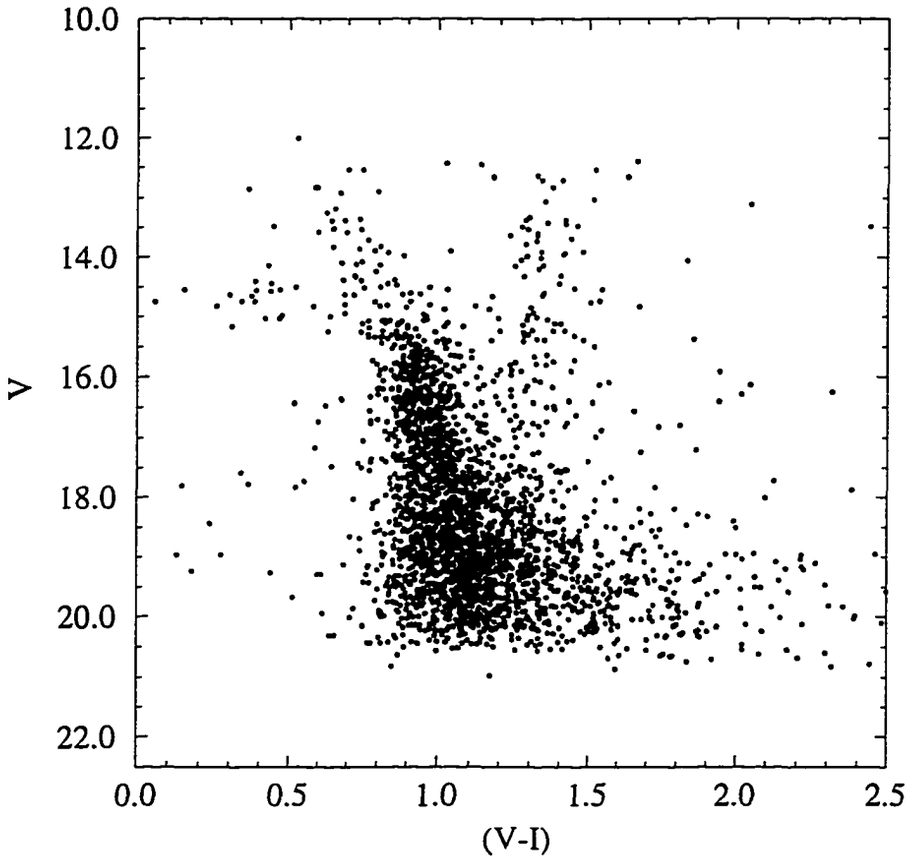

Figure 4.6: $(V, V-I)$ CMD of NGC 7142, containing 2549 stars, not corrected for differential reddening. Sources of scatter are described in the text.

4.1.2 Near-infrared CMDs

The near-infrared observations were restricted by the sensitivity limit of the IR detector. Hence only the giant branches, red giant clumps and turnoff regions were accessible. Also, since an image obtained with the IR detector covered a smaller area of sky (2.8 arcmin on a side compared with a 9 arcmin CCD field), the observing efforts were concentrated on the cluster giants.

Tables 4.1, 4.2, 4.3 and 4.4 contain the VK photometry, while Figures 4.7, 4.8, 4.9 and 4.10 display the $(V, V-K)$ and $(K, V-K)$ CMDs for the four clusters (hereafter, these CMDs will be referred to as near-infrared, or IR, CMDs). These diagrams clearly show that at longer wavelengths the giant branch becomes more upright, and the effect is more pronounced for metal-rich clusters. These CMDs can be compared to the optical ones presented earlier to help define the locus of the giant branch as well as identify possible asymptotic giant branch (AGB) stars or nonmembers.

The IR CMD of NGC 2141 is composed of all the stars found on the K' frames, and agrees with the optical one shown in the previous section. Stars which were determined to be cluster members by Friel and Janes (1993) on the basis of radial velocity measurements are indicated by open circles on the $(K, V-K)$ CMD. The four stars at $(V, V-K \sim 13.7, 3.0)$, and the one at $(V, V-K \sim 12.2, 2.8)$ reside above and blueward of the clump in the optical CMD, and probably are field stars, since they lie to the left of the other stars defining the giant branch. The star at $(V, V-K \sim 14.3, 1.75)$ may be a blue straggler. The clump is situated at $V \sim 15.0$ $(K \sim 11.4)$.

The stars defining the giant branch of NGC 6819 form a very tight sequence (admittedly due in part to a compressed scale for the abscissa), and the clump is represented well by several stars. All these stars have membership probabilities greater than 80%, based on proper motions determined by

Table 4.1: NGC 2141 - optical and infrared photometry of the giants.

Optical ID	IR ID	V	δ	K	δ	$(V-K)$	δ
7	145-1	13.052	0.022	8.333	0.026	4.72	0.03
19	145-50001	14.052	0.007	10.199	0.060	3.85	0.06
22	145-2	14.132	0.007	10.293	0.023	3.84	0.02
14	145-3	13.648	0.007	10.802	0.025	2.85	0.02
81	145-4	15.071	0.011	10.860	0.023	4.21	0.03
71	145-5	14.981	0.006	11.270	0.023	3.71	0.02
43	145-6	14.694	0.007	11.396	0.032	3.30	0.03
31	145-7	14.499	0.006	11.223	0.026	3.28	0.03
67	145-9	14.961	0.005	11.301	0.015	3.66	0.02
59	145-10	14.909	0.005	11.415	0.024	3.49	0.02
104	145-13	15.449	0.010	11.793	0.057	3.66	0.06
24	145-14	14.266	0.006	12.263	0.070	2.00	0.07
152	177-1	15.014	0.025	8.294	0.033	6.72	0.04
50009	177-50001	12.231	0.010	8.979	0.059	3.25	0.06
11	177-2	13.250	0.006	8.775	0.040	4.48	0.04
15	177-3	13.663	0.005	9.542	0.057	4.12	0.06
35	177-5	14.528	0.013	10.876	0.057	3.65	0.06
58	177-9	14.901	0.006	11.368	0.058	3.53	0.06
79	177-11	15.088	0.005	11.605	0.023	3.48	0.02
51	177-10	14.846	0.010	11.647	0.058	3.20	0.06
50025	199-50001	13.886	0.011	10.562	0.185	3.32	0.19
50020	199-50002	13.624	0.013	10.496	0.185	3.13	0.19
50023	199-50003	13.789	0.010	10.885	0.186	2.90	0.19
50060	199-50004	14.799	0.011	11.445	0.190	3.35	0.2
12	225-3	13.303	0.007	8.850	0.024	4.45	0.03
26	225-4	14.185	0.017	10.367	0.024	3.82	0.03
40	225-5	14.614	0.020	10.601	0.024	4.01	0.03
3	225-10	12.821	0.007	11.571	0.028	1.25	0.03
72	225-12	15.005	0.005	11.580	0.057	3.42	0.06
64	225-14	14.941	0.006	11.357	0.058	3.58	0.06

Table 4.2: NGC 7142 - optical and infrared photometry of the giants. The V magnitude for G160-33 is from Crinklaw and Talbert (1991) since that star was saturated in the photometry presented in this work. The error for star G160-33 is an upper limit.

Optical ID	IR ID	V	δ	K	δ	$(V-K)$	δ
50007	h3-106	12.635	0.029	9.260	0.031	3.38	0.04
3	h3-1	13.637	0.018	10.248	0.023	3.39	0.03
9	h3-2	13.730	0.007	10.659	0.023	3.07	0.02
13	h3-3	13.379	0.019	11.656	0.025	1.72	0.03
50015	h5-1	13.031	0.009	9.223	0.029	3.81	0.03
1	h5-2	13.383	0.006	9.858	0.028	3.53	0.03
17	h5-3	14.142	0.007	10.891	0.029	3.25	0.03
30	h5-4	14.645	0.006	11.255	0.029	3.39	0.03
24	h5-5	13.482	0.165	11.924	0.030	1.56	0.17
50010	G93-58	12.706	0.017	8.539	0.039	4.17	0.04
7	G93-1	13.635	0.018	10.543	0.024	3.09	0.03
16	G93-3	13.388	0.021	12.002	0.029	1.39	0.04
34	G93-2	14.979	0.027	11.731	0.030	3.25	0.04
35	G93-4	14.826	0.008	12.109	0.030	2.72	0.03
55	G93-5	15.061	0.019	12.709	0.030	2.35	0.04
97	G93-6	16.524	0.035	12.749	0.031	3.78	0.05
—	G160-33	11.140	< 0.1	7.585	0.023	3.56	0.1
4	G160-1	13.447	0.026	9.901	0.018	3.55	0.03
12	G160-3	14.047	0.019	10.954	0.012	3.09	0.02
13	G160-4	13.379	0.019	11.722	0.015	1.66	0.02
428	G160-5	16.140	0.055	12.312	0.058	3.83	0.08
21	G342-2	14.314	0.008	10.962	0.041	3.35	0.04
23	G342-3	13.577	0.010	11.989	0.085	1.59	0.09
58	G342-4	15.160	0.006	12.519	0.053	2.64	0.05
50004	G421-16	12.009	0.023	7.614	0.023	4.40	0.03
2	G421-1	13.374	0.010	10.153	0.021	3.22	0.02
32	G421-2	15.377	0.009	10.791	0.026	4.59	0.03
20	G421-3	13.536	0.006	11.783	0.025	1.75	0.03
22	G421-5	13.523	0.008	11.697	0.023	1.83	0.02
255	G421-4	16.668	0.028	12.034	0.019	4.63	0.03
11	G51-1	13.910	0.008	11.052	0.008	2.86	0.01
14	G51-2	14.012	0.009	11.125	0.009	2.89	0.01
31	G51-3	14.853	0.020	12.033	0.019	2.82	0.03

Table 4.3: NGC 6791 - optical and infrared photometry of the giants. ID numbers and V magnitudes are from Garnavich et al. (1994). According to those authors, an error estimate is missing for star R1 since only one V and one I frame were photometered and therefore an rms error could not be calculated.

ID	V	δ	K	δ	$(V-K)$	δ
R1	13.88		6.60	0.05	1.28	0.05
R2	13.72	0.08	9.32	0.19	1.40	0.21
R3	14.06	0.03	9.78	0.06	1.28	0.07
R4	14.00	0.13	7.82	0.06	1.18	0.14
R5	14.68	0.09	6.84	0.06	1.84	0.11
R7	13.83	0.07	7.69	0.05	1.14	0.09
R8	13.80	0.03	10.26	0.15	1.54	0.15
R9	14.13	0.05	10.19	0.16	1.94	0.17
R10	14.52	0.08	11.03	0.21	1.49	0.22
R11	14.59	0.03	11.60	0.52	1.99	0.52
R12	13.84	0.02	9.50	0.05	1.34	0.05
R14	13.61	0.07	8.84	0.07	1.77	0.10
R16	13.73	0.02	9.79	0.07	1.94	0.07
R17	14.55	0.06	11.07	0.30	1.48	0.31
R19	14.17	0.13	10.14	0.12	1.03	0.18
R22	14.50	0.03	11.34	0.38	1.16	0.38

Table 4.4: NGC 6819 - optical and infrared photometry of the giants.

Optical ID	IR ID	V	δ	K	δ	$(V-K)$	δ
50004	f1655-1	11.656	0.013	8.444	0.010	3.21	0.02
50003	f1655-2	11.643	0.009	8.957	0.013	2.69	0.08
10	f1655-3	13.133	0.007	10.115	0.013	3.02	0.01
2	f1655-4	12.869	0.006	10.181	0.012	2.69	0.09
30	f1655-5	13.284	0.007	10.428	0.015	2.86	0.05
14	f1655-6	12.956	0.006	10.431	0.011	2.53	0.02
29	f1655-7	13.245	0.006	10.367	0.049	2.88	0.08
44	f1655-8	13.897	0.007	11.187	0.170	2.71	0.01
32	f1655-9	12.645	0.005	12.051	0.363	0.59	0.05
50008	f1655-95	11.837	0.207	7.764	0.016	4.07	0.08
50012	f1657-176	11.966	0.013	8.062	0.013	3.90	0.00
50013	f1657-50001	11.426	0.013	5.501	0.072	5.93	0.03
3	f1657-50002	12.833	0.006	10.112	0.064	2.72	0.02
49	f1657-50004	14.101	0.006	11.477	0.087	2.62	0.02
54	f1687-2	14.234	0.008	11.326	0.029	2.91	0.00
21	f1687-94	13.122	0.007	10.212	0.013	2.91	0.01
50002	f1687-50001	11.570	0.013	6.779	0.055	4.79	0.09
20	f1687-50008	13.120	0.007	10.180	0.039	2.94	0.04
50006	f1707-148	11.854	0.013	8.130	0.017	3.72	0.02
18	f1707-50009	13.069	0.005	10.185	0.041	2.88	0.08
25	f1707-50010	13.126	0.006	10.310	0.039	2.82	0.01
34	f1707-50012	13.644	0.007	10.794	0.051	2.85	0.05
8	f1746-4	13.065	0.008	10.130	0.012	2.94	0.04
17	f1746-5	13.107	0.008	10.170	0.018	2.94	0.04
2450	f1772-2	12.244	0.007	8.912	0.009	3.33	0.03
1	f1772-4	12.831	0.005	9.692	0.013	3.14	0.04
50021	f1772-5	12.763	0.005	9.638	0.013	4.13	0.02
9	f1772-6	13.013	0.006	10.097	0.015	2.92	0.01
16	f1772-7	13.169	0.008	10.055	0.013	3.11	0.01
11	f1772-11	13.017	0.006	10.177	0.015	2.84	0.04
22	f1772-50001	13.213	0.008	10.107	0.015	3.11	0.02

Sanders (1972). The two stars at $(V, V-K \sim 11.6, 2.7;\ 11.7, 3.2)$ probably are nonmembers, even though the bluer one was shown to have a proper motion membership probability of 92%.

At first glance, the $(V, V-K)$ CMD of NGC 6791 appears to be extremely scattered. However, comparison with the optical one shows that only a 1 magnitude range is apparent for the red end of the giant branch, and the scale of the IR CMD is reflecting this range (the stars redder than $(V-K) \sim 5.5$ are the ones defining the extreme end of the giant branch). The giant branch is much straighter in the $(K, V-K)$ CMD. A few stars mark the position of the clump at $V \sim 14.5$. All the giants shown in the IR CMDs are members, according to radial velocity measurements obtained by Garnavich et al. (1994).

The IR CMD of NGC 7142 is somewhat scattered, but this probably is due to the presence of nonmembers since the radial velocity members ascertained by Friel and Janes (1993) (indicated by open circles) forms a tight locus. It is assumed that the small group of stars at $K \sim 11.0$ mark the location of the red giant clump since various optical CMDs (this work, van den Bergh and Heeringa (1970) and Crinklaw and Talbert (1991), for example) show a loose clustering of stars about this magnitude, while the stars at $(V-K) \sim 1.5$ reside in the region where blue stragglers would be expected.

4.1.3 Field Star Contamination

The presence of foreground and background stars in a CCD image of a star cluster leads to confusion in the cluster CMD, since the main sequence may appear anomalously wide, while the number of stars in other features such as giant branches and clumps may become artificially enhanced. Thus, removal of field stars results in a more realistic portrayal of the cluster CMD. In

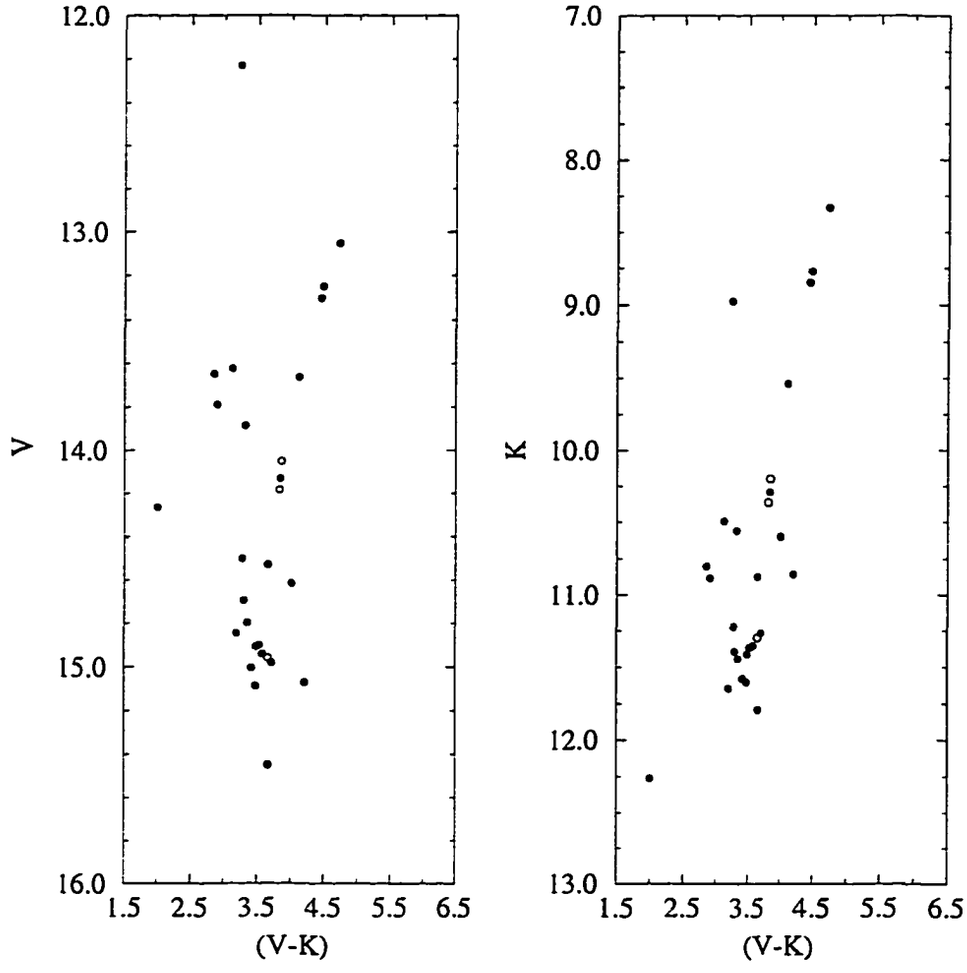

Figure 4.7: $(V, V-K)$ and $(K, V-K)$ CMDs of the giant branch of NGC 2141. Radial velocity measurements by Friel and Janes (1993) determined the membership of a few stars, as indicated by open circles.

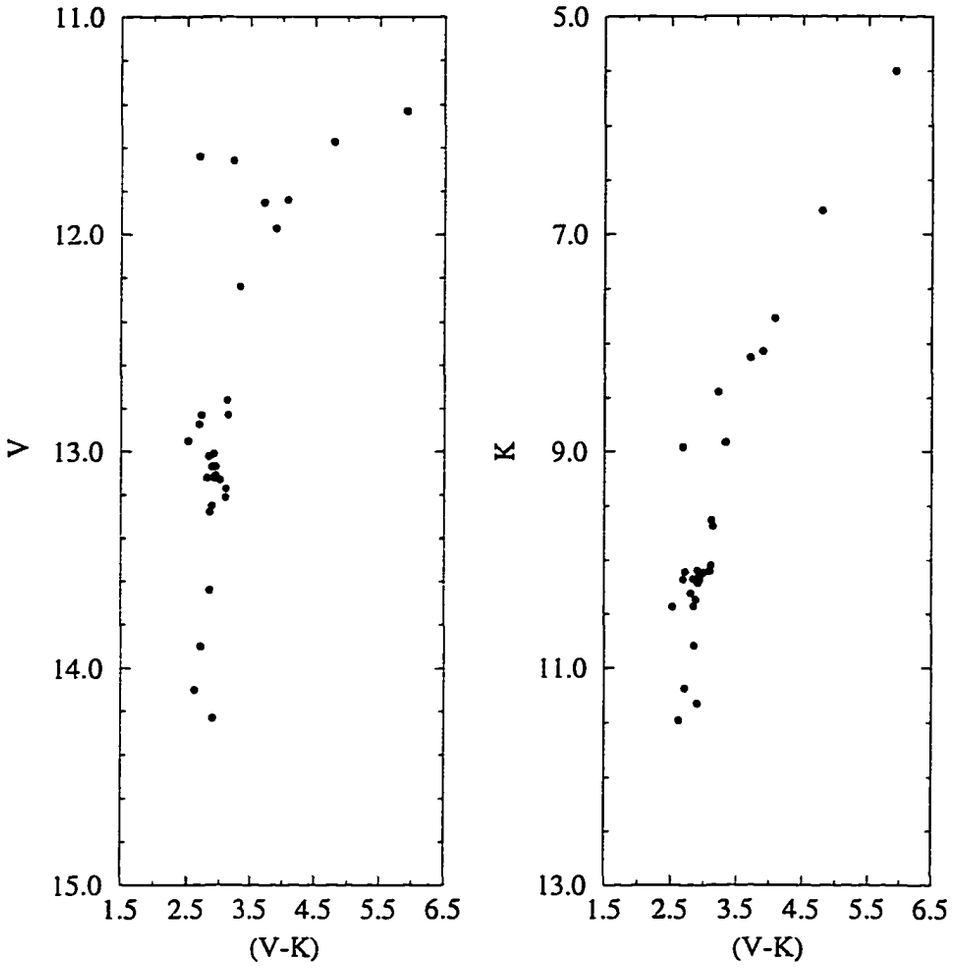

Figure 4.8: $(V, V-K)$ and $(K, V-K)$ CMDs of the giant branch of NGC 6819. All stars are members, based on a proper motion survey by Sanders (1972).

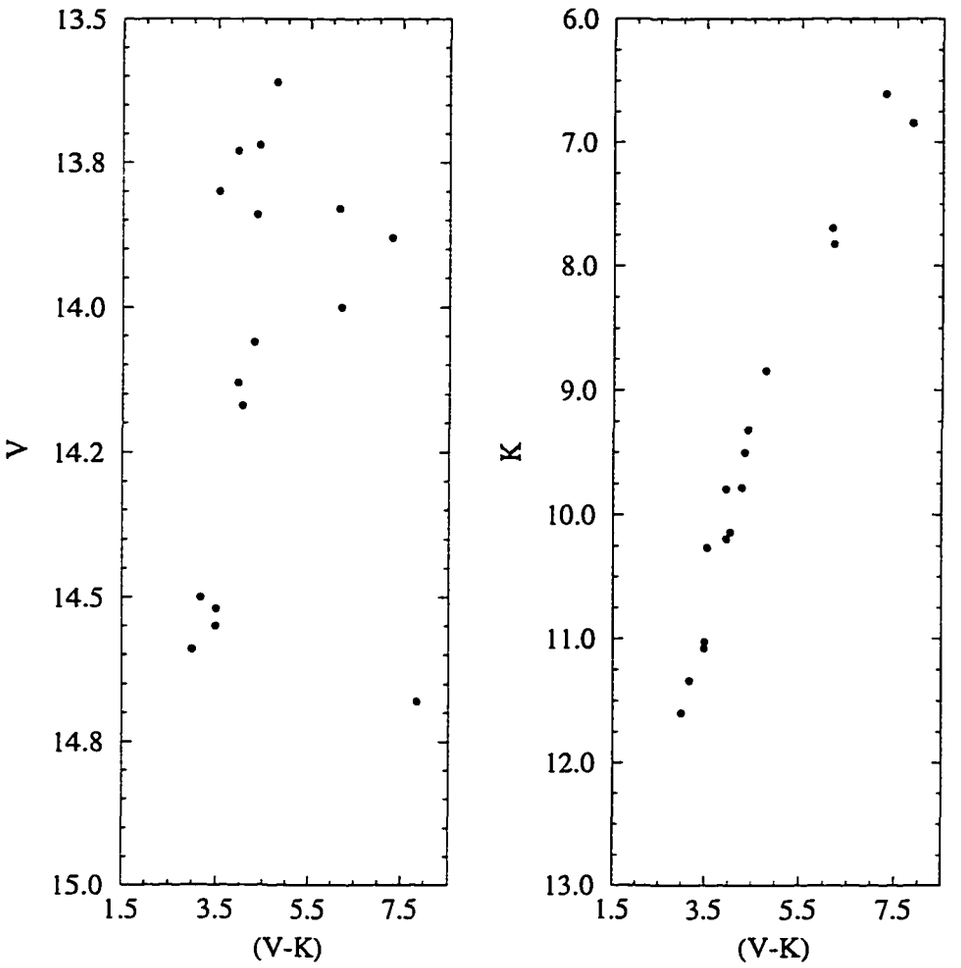

Figure 4.9: $(V, V-K)$ and $(K, V-K)$ CMDs of the giant branch of NGC 6791. All stars are members, as determined from radial velocities obtained by Garnavich et al. (1994).

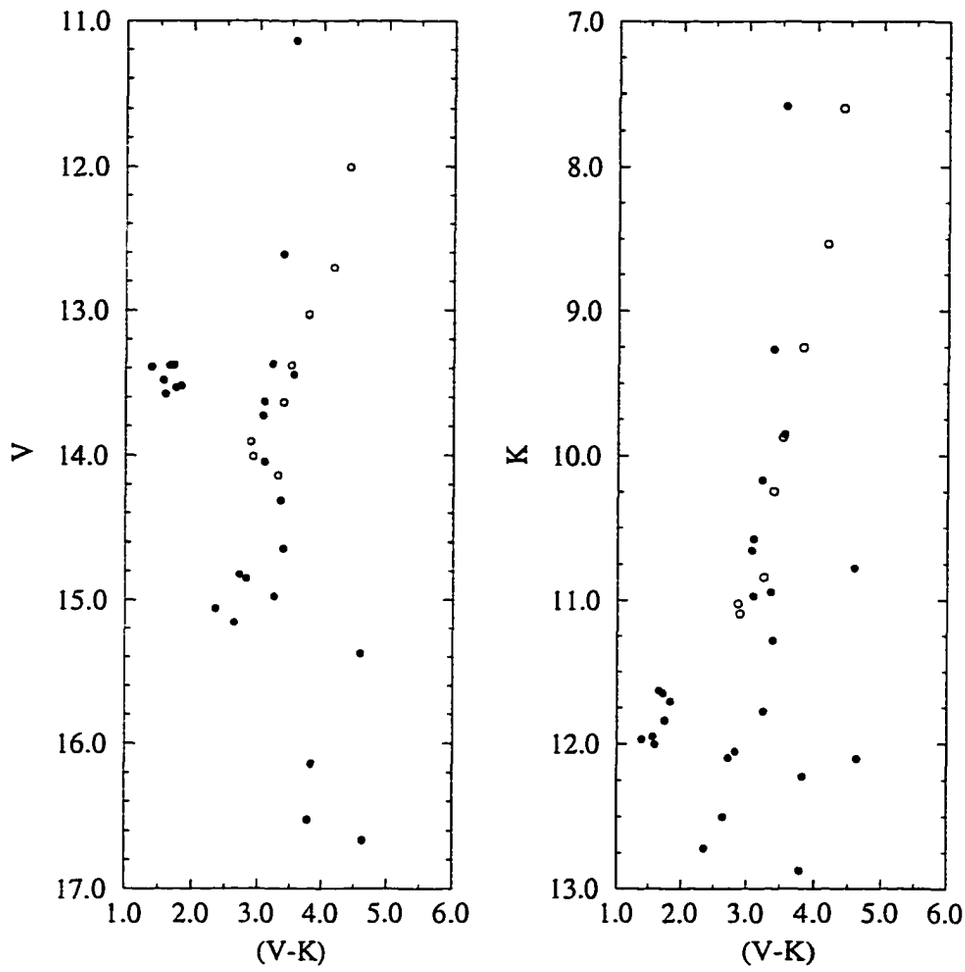

Figure 4.10: $(V, V-K)$ and $(K, V-K)$ CMDs of the giant branch of NGC 7142. Open circles denote radial velocity cluster members, as determined by Friel and Janes (1993).

practice, this is a difficult task. Two methods were utilised, as described below.

In the first method, field stars were generated from a model which used the bulge, disc and halo luminosity functions of Bahcall and Soneira (1980), weighted for each cluster's location in the galaxy according to those authors' prescription: given the galactic coordinates and reddening of the cluster, and the surface area covered by the observations, a luminosity function was computed, from which a model CMD was constructed [additions to the model which incorporated giants (Bahcall and Soneira, 1981; Bahcall and Soneira, 1983) and the means to generate transformations between colours (Bahcall and Soneira, 1982) were used as well]. Note that this model was not altered to take into account photometric errors. The model CMD was compared to that of the cluster, and cluster and model field stars which were nearly equal in magnitude and colour (within some tolerance of the order of the photometric errors) were removed in pairs, resulting in a final field star-subtracted data set.

In the second method, field stars from frames taken in the vicinity of each cluster were used to construct field CMDs, which were compared to the cluster CMD (even though it was assumed that these fields were far enough from the cluster to contain few cluster members, but still close enough to it to have the same field star density, there may still be cluster members present in the field frames). The field stars were removed as described above, and care was taken to ensure that the field and cluster areal coverage was the same. While the subtraction procedure used in both methods is rather simplistic, and possible cluster members may be removed while nonmembers remain, it serves to indicate roughly the amount of field star contamination.

It is important to check for completeness levels in the data for both the field and cluster frames, since varying observing conditions, different nights

of observations, different exposure times and so on can affect the magnitude limit of the field and cluster frames. Completeness levels usually are investigated by performing artificial star experiments. Artificial frames are generated by adding stars to real data frames. In most cases, several frames containing a few stars each (about 10% of the total number of real stars on the frame) are created. Photometry is performed as usual, and the number of artificial stars recovered is compared to the number originally added. A completeness fraction may be calculated by dividing the number of recovered stars by the number of input stars in some magnitude bin. Completeness fractions were calculated for the field and cluster frames for NGC 2141 and NGC 7142, and the conclusions from these are described below.

NGC 2141

Since the observing nights were clear enough to allow observations of regions of blank sky in the vicinity of the cluster, both correction methods could be applied. First, the blank frames were reduced in a manner identical to that for the program frames, and a field star CMD was produced (Figure 4.11, $\sim$ 600 stars). This CMD was compared to the cluster CMD as described above. The entire cluster and blank sky fields, as well the central cluster frame and one blank sky frame, were used in the field star subtraction, and results compared. It was found that the latter set of data produced the best results, presumably because the spatial coverage was identical and the majority of stars on the cluster frame were cluster members. Figure 4.12 shows the final CMD, corrected for field star contamination. Note that this involved a straight star-by-star subtraction (*i.e.* no completeness corrections were performed) since the data were taken on the same night, the integration times were the same for the cluster and field frames, the magnitude limits

were roughly the same in both the cluster and field CMDs, and artificial star tests showed the completeness fractions to be similar.

The galaxy model was applied next, but the results were unsuitable since the number of field stars was overestimated (1260 stars as compared with 600). This is not surprising, however, since the model has been compared to data only for galactic latitudes greater than 20°, and has been tested only to 10°. Figure 4.13 displays the model CMD, while Figure 4.14 shows the model field star subtraction. This may be compared to the previous one. The subtraction using actual data is preferred, since it appears to represent most accurately the number and location of field stars.

NGC 6819

Only the galaxy model was used to derive a field star CMD for this cluster (Figure 4.15), since there wasn't time to obtain blank sky fields near the cluster. The efforts of Sanders (1972) made it possible to compare the number of proper motion nonmembers above the CMD turnoff with the number of field stars generated from the model for the same area covered by the proper motion survey. 50 proper motion nonmembers compared with 60 model stars indicate the model provides a reasonable estimate of the number of giants brighter than $V \sim 14.5$. However there is no guarantee that an extrapolation to the main sequence will be valid. The results of the subtraction are presented in Figure 4.16.

NGC 7142

A CMD produced from the one blank field obtained near this cluster is shown in Figure 4.17. Only one frame (the centre one) of the cluster was used in the field star subtraction, and the result of the subtraction is given

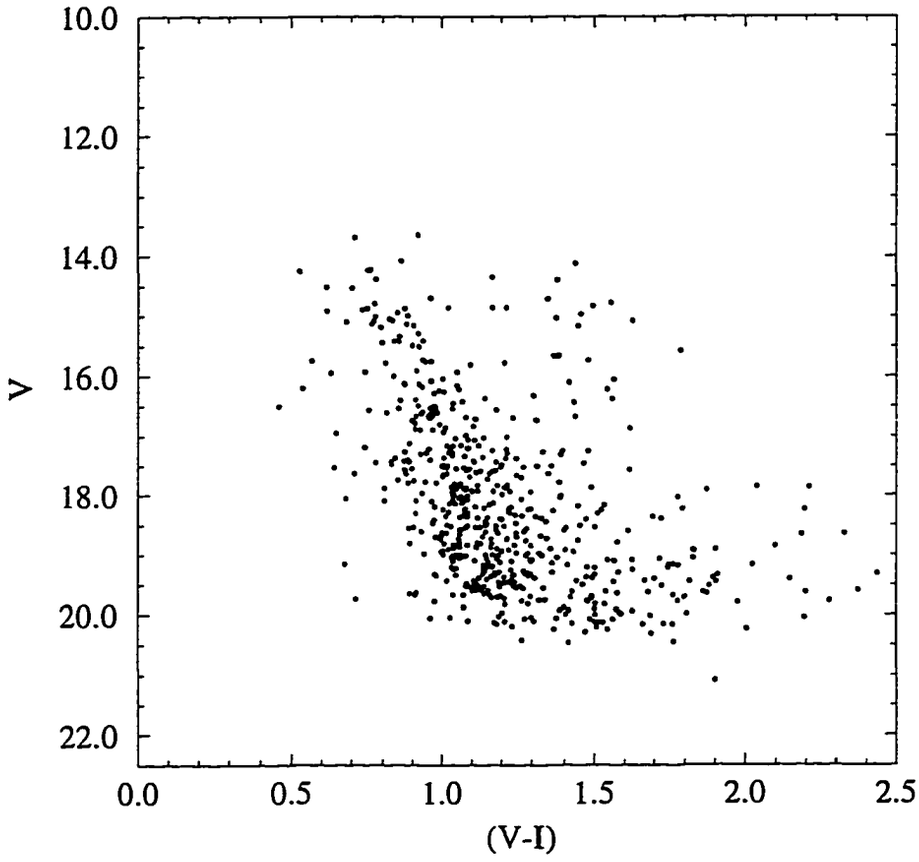

Figure 4.11: CMD of one frame near NGC 2141 containing field stars.

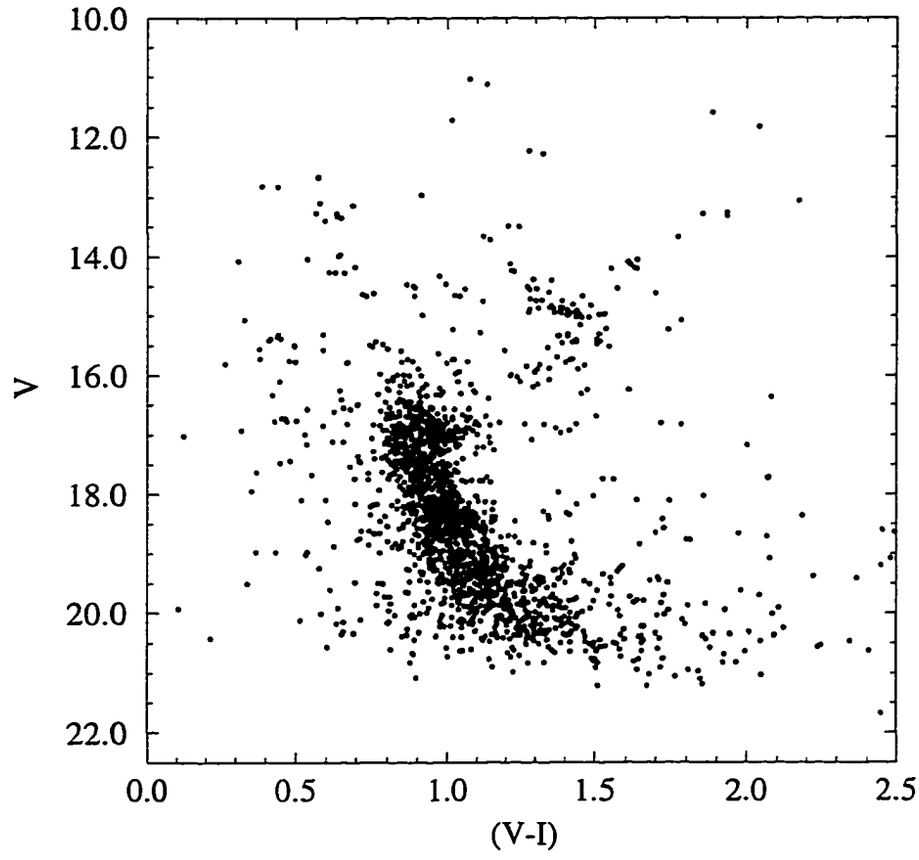

Figure 4.12: CMD of NGC 2141 with field stars subtracted as described in the text.

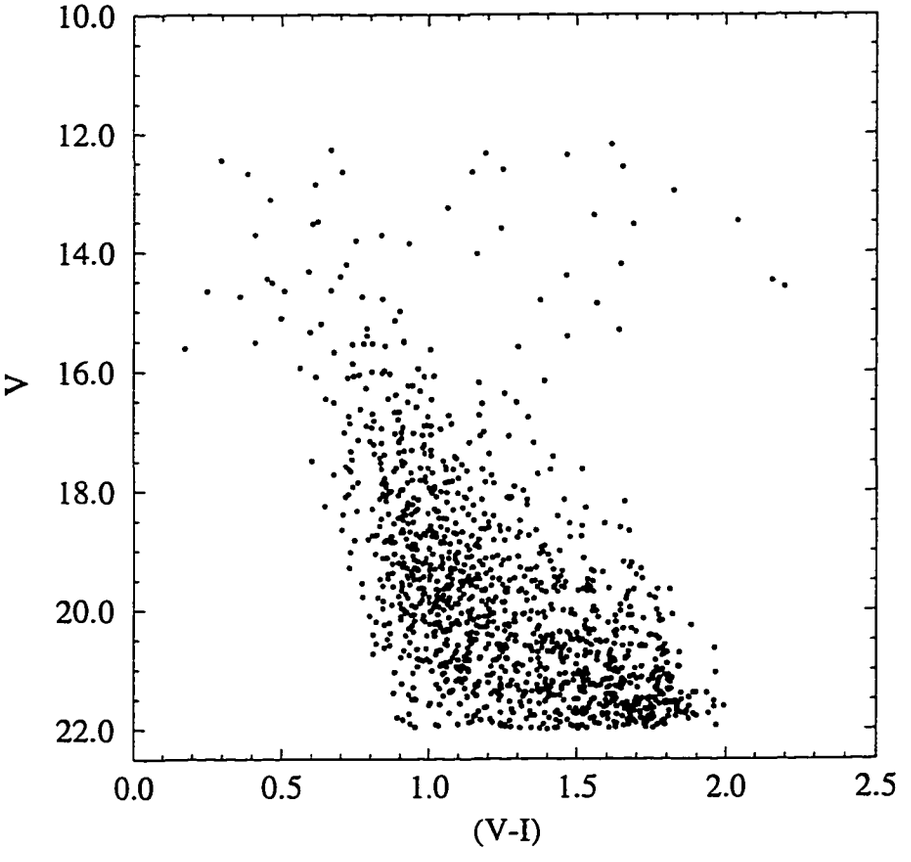

Figure 4.13: CMD of model field stars, for the region around NGC 2141.

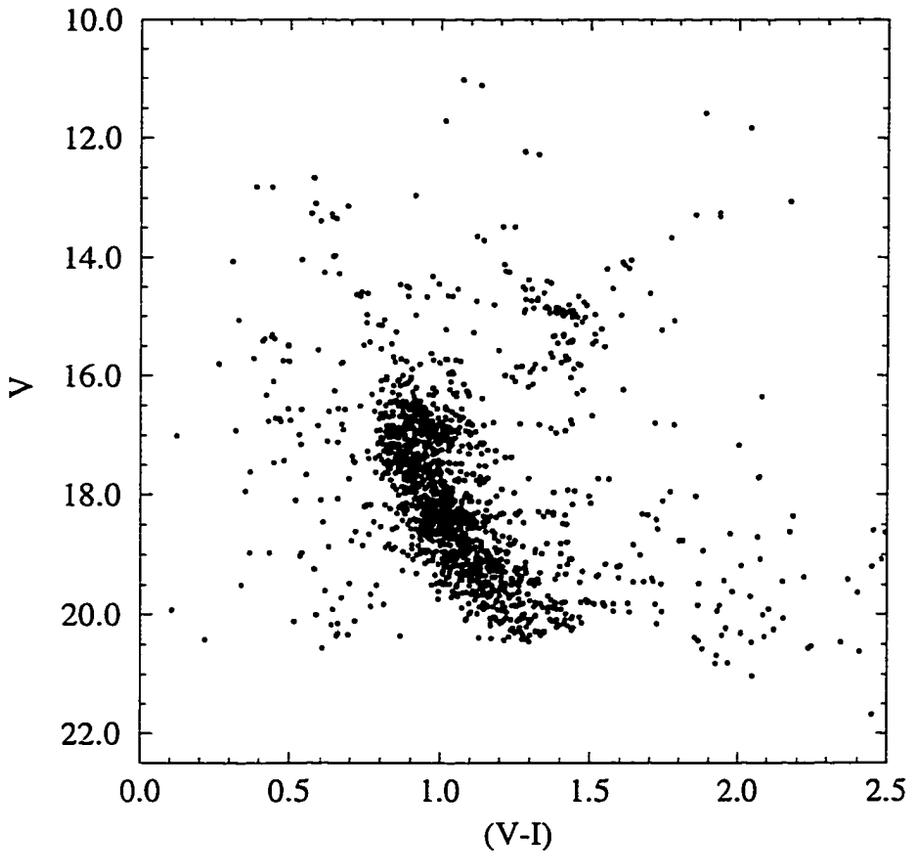

Figure 4.14: CMD showing results of the subtraction of the model field stars from the CMD of NGC 2141.

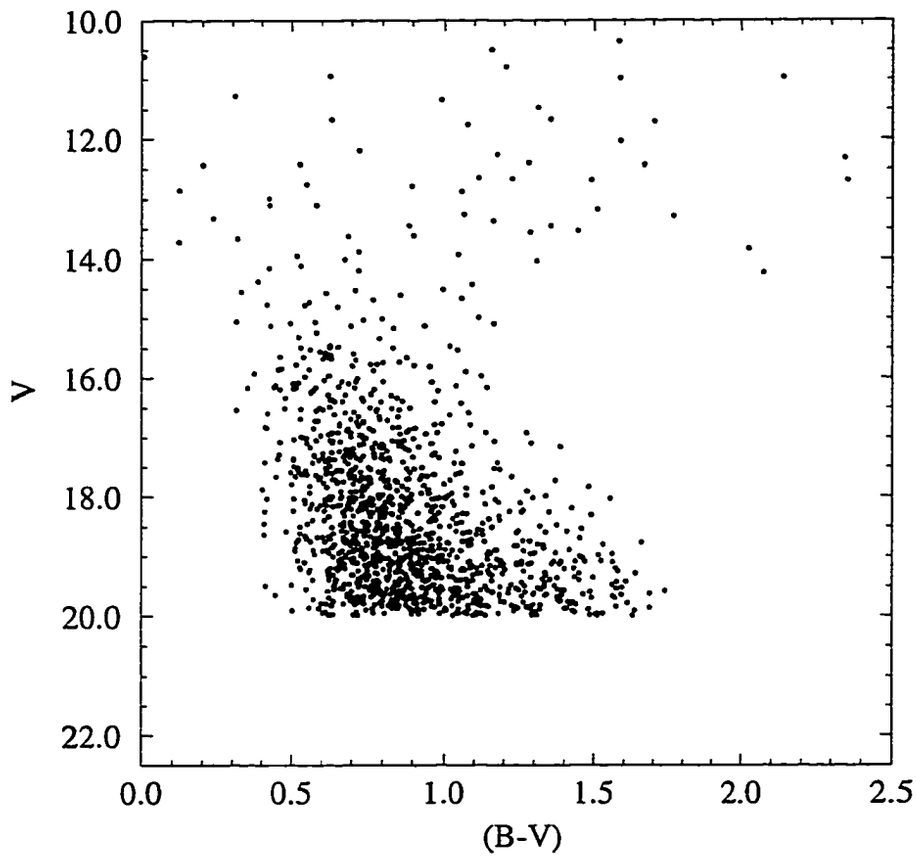

Figure 4.15: CMD of the model field stars in the vicinity of NGC 6819.

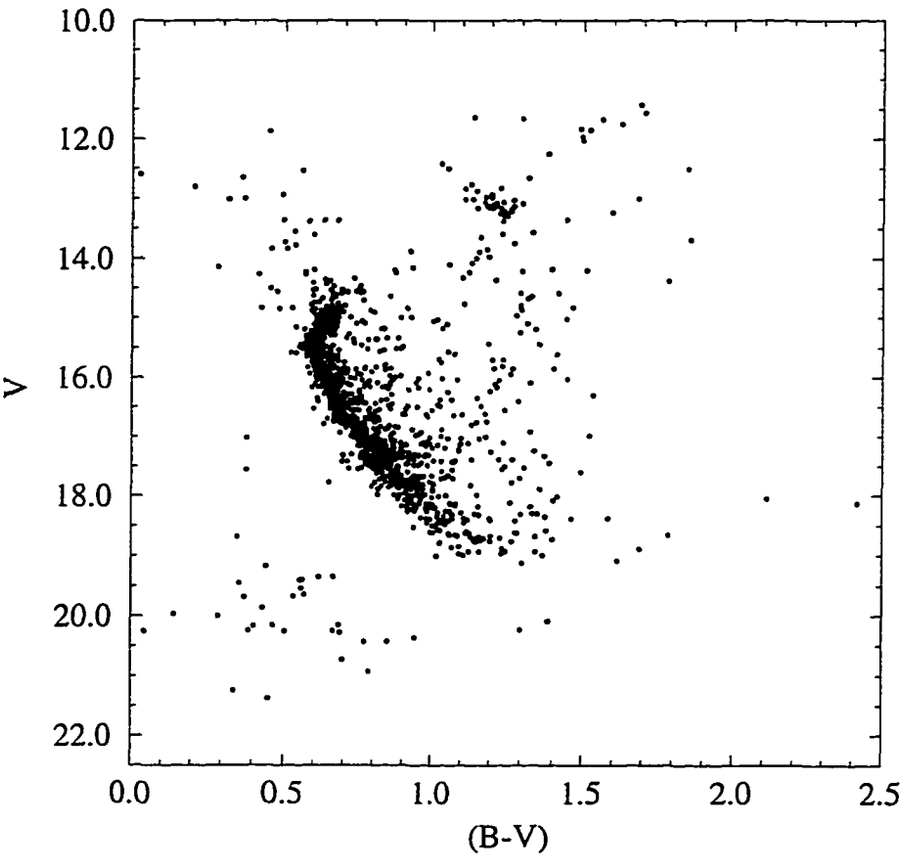

Figure 4.16: CMD showing results of the subtraction of the model field stars from the CMD of NGC 6819.

in Figure 4.18. Even though not many stars remain, the turnoff and giant branch are preserved. Completeness fractions were calculated for one cluster frame and the field frame, and were similar for the same magnitude bins, indicating that both regions exhibit the same level of "incompleteness" at the same magnitude. Hence completeness corrections were not done for this cluster.

The model field star CMD for an area of 73 square arcmin (one frame) is shown in Figure 4.19. The result of the subtraction of these stars is given in Figure 4.20. Both the field frame and the model produced about 700 stars, but in this case, the model star subtraction yielded results which looked more as expected.

NGC 6791

Since the turnoff, subgiant and giant regions are so well-defined in this cluster despite the number of field stars, no attempt was made to correct for field star contamination.

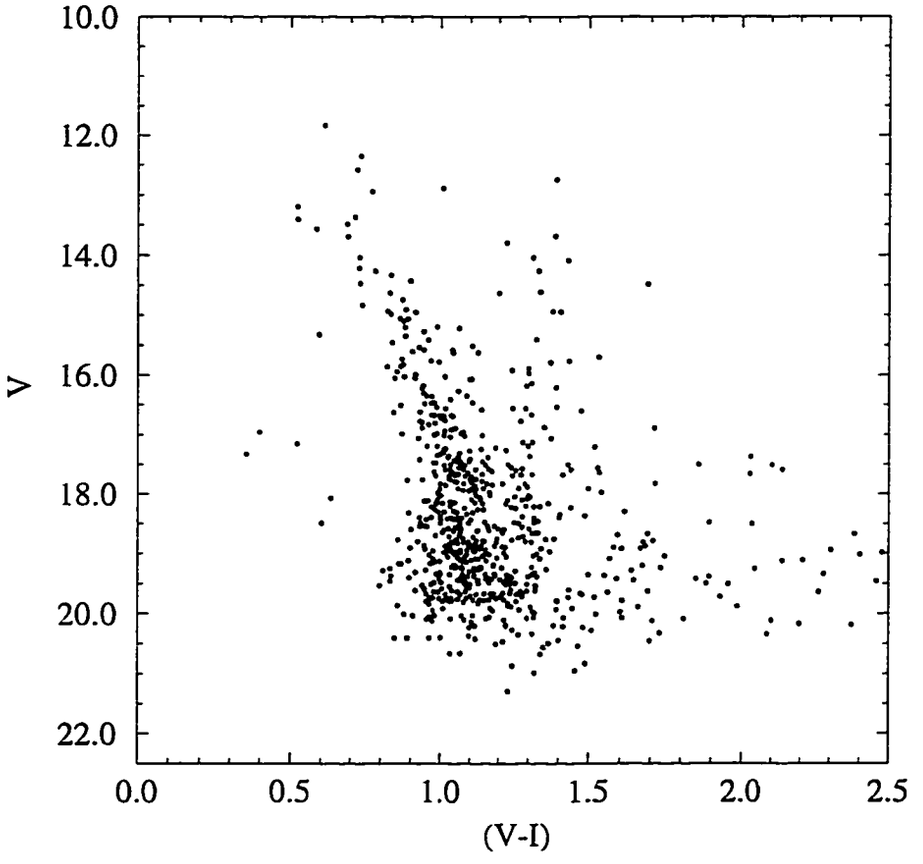

Figure 4.17: CMD of the field frame located near NGC 7142.

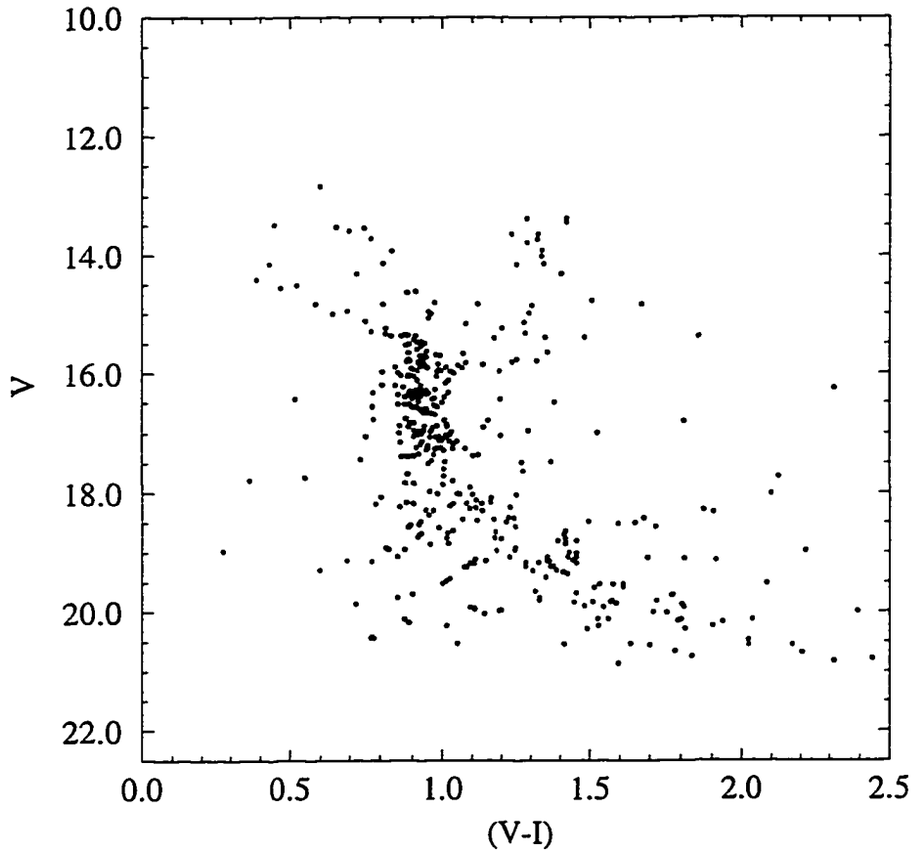

Figure 4.18: CMD showing results of the subtraction of the field stars from the CMD of the central frame of NGC 7142.

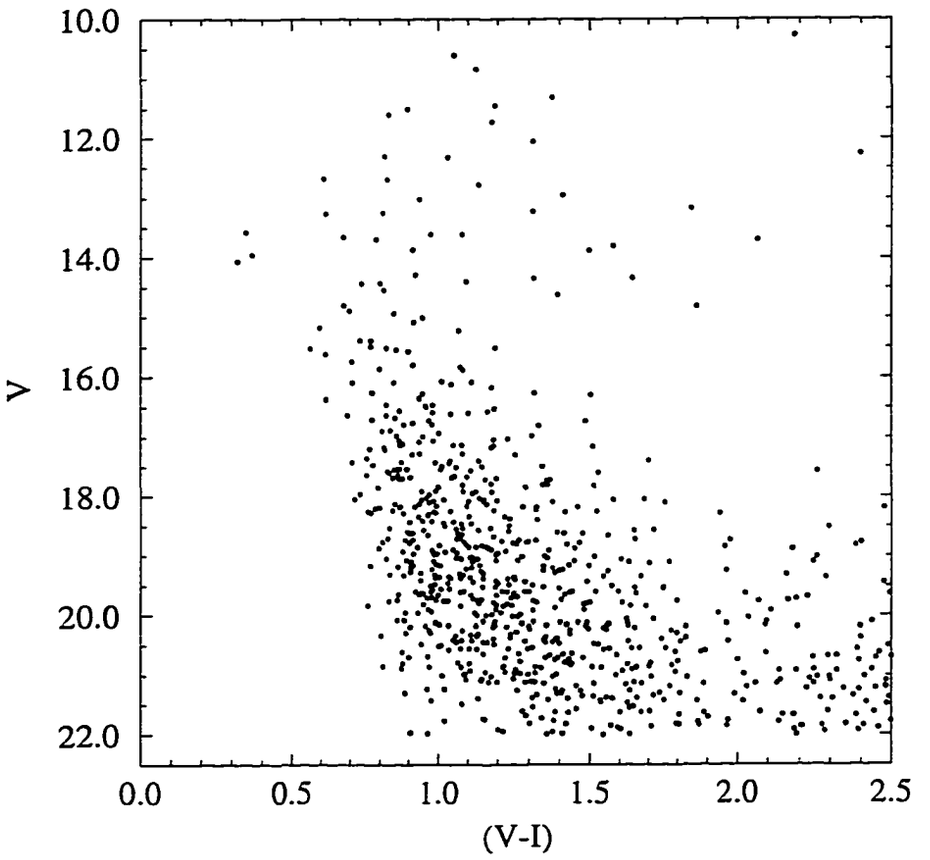

Figure 4.19: CMD showing the model stars in the vicinity of NGC 7142, for an area equal to that covered by one frame (73 square arcmin).

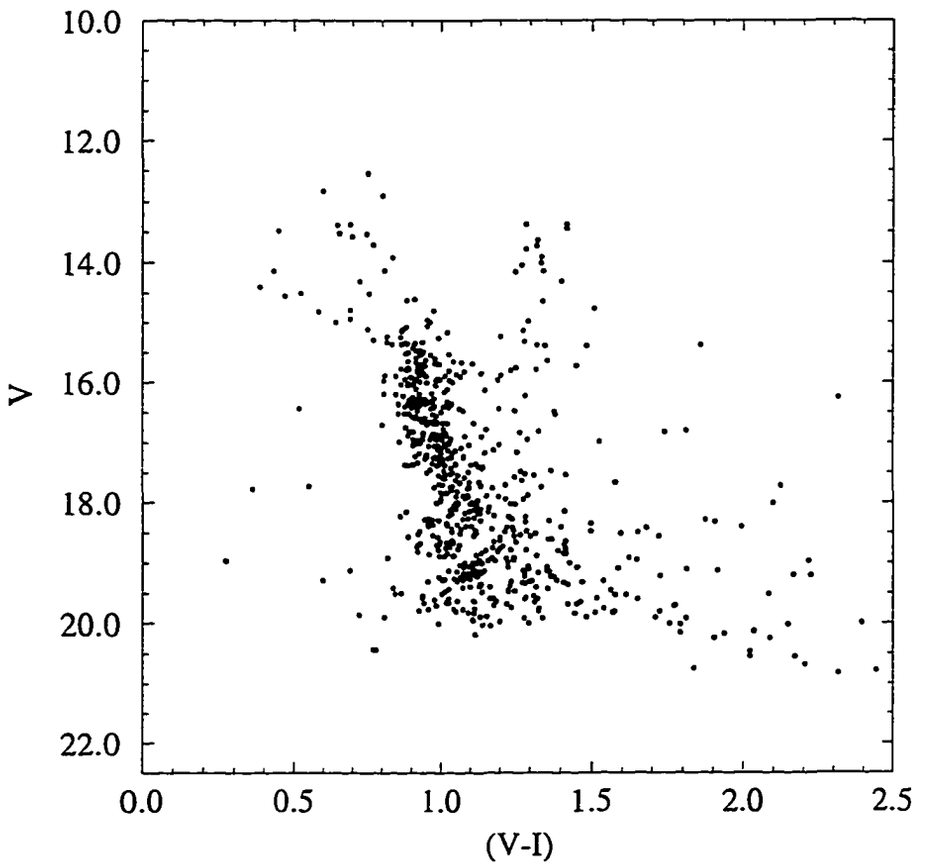

Figure 4.20: CMD showing results of the subtraction of the model field stars from the CMD of one frame of NGC 7142.

4.2 Cluster Parameters

4.2.1 Metallicity

Metal abundances, or metallicities, are expressed in terms of the stellar iron to hydrogen number abundance ratio compared to that of the sun, and are defined by

$$[Fe/H] \equiv \log[n(Fe)/n(H)]_* - \log[n(Fe)/n(H)]_\odot \tag{4.1}$$

The fraction by mass of metals is given by

$$Z = \frac{m(N > 2)}{m(H) + m(He) + m(N > 2)}, \tag{4.2}$$

where N is the atomic number. For the sun, $Z = 0.0188$ (Anders and Grevesse, 1989), and solar metallicity is given by $[Fe/H] = 0.0$.

There are several methods which are used to determine metal abundances (see Kraft (1979) for a general review). Three common methods utilise spectrum synthesis methods or photometric/spectrophotometric indices. Each is described briefly below.

In the first method, various stellar and atomic parameters such as temperatures, opacities and gravities are obtained by comparing line strengths and shapes in observed high-resolution spectra to those in theoretical ones (Cohen, 1978). Once the parameters are constrained, the number of absorbers of each element is determined, which gives individual elemental abundances in the star. This technique is applicable only for the brightest stars, for which high signal-to-noise ratio, high resolution spectra can be obtained.

Various photometric systems [*e.g.* Strömgren (1963), DDO (McClure and van den Bergh, 1968), UBV (Johnson and Morgan, 1953)] can be calibrated for dependences on metallicity at a given spectral type or colour. Note that

these methods yield relative abundances, and must be tied to an absolute scale of $[Fe/H]$ established by some other means (usually high-dispersion spectroscopy of bright stars).

Finally, methods utilising spectrophotometric indices involve the use of medium to low resolution spectra (Searle and Zinn, 1978). Abundances are obtained by measuring the integrated flux in a fixed narrow wavelength range centred on some feature relative to the flux in a region of nearby continuum. Values are calibrated against high-resolution spectra. This method works with individual stars (Faber et al., 1985) or integrated light from galaxies or distant star clusters (Burstein et al., 1984).

The metallicity estimates for the four clusters studied here were obtained from Friel and Janes (1993), who used medium resolution CCD spectroscopic observations obtained at Kitt Peak National Observatories (KPNO) and Cerro Tololo International Observatory (CTIO), and determined metallicities by calibration of spectroscopic indices which measured mainly neutral iron and iron blends (Friel, 1987).

For each cluster, they averaged the individual determinations of metallicity to yield a mean value. Stars judged to be nonmembers on the basis of disparate radial velocities and metallicities were excluded from the means. Table 4.5 lists the average metallicities along with the number of stars used in the determinations.

4.2.2 Distance Modulus

Independent estimates of the distance modulus may be made by comparing the cluster zero-age-main-sequence (hereafter ZAMS) with a semi-empirical ZAMS calibration or comparing the location in the CMD of the helium-burning clump stars of the cluster to that of a cluster of known distance

Table 4.5: Adopted mean metallicities from Friel and Janes (1993) for the program clusters. Number of stars used in each determination is indicated by n.

Cluster	$[Fe/H]$	n
NGC 2141	-0.39 ± 0.11	6
NGC 7142	-0.00 ± 0.06	11
NGC 6819	0.05 ± 0.11	7
NGC 6791	0.19 ± 0.19	9

modulus. VandenBerg and Poll (1989) defined the ZAMS for a solar abundance cluster (*i.e.* one for $Y = 0.27$, $[Fe/H] = 0.0$) to be

$$M_V(B-V) = 2.84-6.79(B-V)+31.77(B-V)^2-31.6(B-V)^3+10.57(B-V)^4 \tag{4.3}$$

and determined the following corrections for changes in the helium and metal abundances:

$$\delta M_V(Y) = 2.6(Y - 0.27) \tag{4.4}$$

and

$$\delta M_V([Fe/H]) = -[Fe/H](1.444 + 0.362[Fe/H]). \tag{4.5}$$

So, for any cluster,

$$V = M_V(B - V) + \delta M_V(Y) + \delta M_V([Fe/H]) + (m - M)_V. \tag{4.6}$$

An analagous $V, V - I$ relation was derived from the main sequence of the Hyades [$(m - M)_V = 3.35$ (Swenson et al., 1994), $E(B - V) = 0.0$, $[Fe/H] = 0.127$ (Boesgaard and Friel, 1990)]. V and I observations of the Hyades stars (Reid, 1993) and the cluster parameters given above were used to construct a CMD (M_V versus $(V - I)_0$). Some of the $(B - V)$ colours associated with the brighter V magnitudes were transformed to $(V - I)$ via a

statistical relation derived by Caldwell et al. (1993). The resulting CMD is shown in Figure 4.21. The ZAMS was derived by fitting the main sequence with the following quadratic polynomial:

$$M_V(V-I) = 3.08-13.09(V-I)+44.64(V-I)^2-39.6(V-I)^3+11.56(V-I)^4. \quad (4.7)$$

Note that the position of the main sequence has been adjusted in absolute magnitude by $\delta M_V = -0.19$ (Equation 4.5) to account for the metal abundance of the Hyades.

To determine the apparent distance moduli of the clusters in question, the average apparent magnitude of the clump stars in the well-studied open cluster M67 [$V_{clump} = 10.54 \pm 0.05$] (Montgomery et al., 1993) was compared with that of each cluster. The distance modulus of M67 [$(m-M)_V = 9.50 \pm 0.10$ for $E(B-V) = 0.04$] was obtained by comparing (by eye) Montgomery et al.'s (1993) $(V, B-V)$ CMD with VandenBerg and Poll's (1989) semi-empirical ZAMS calibration (Figure 4.22). Note that since clump absolute magnitude depends on the cluster metallicity, a value of $M_{Vclump} = 0.99$ for M67 is required, as described below.

This method has two advantages over the main-sequence fitting technique. First, it is independent of reddening; and second, it is much less sensitive to metallicity uncertainties [sensitivity of the clump to changes in metallicity, at a fixed colour, is at least a factor of 3 less than that of the ZAMS, according to VandenBerg and Poll (1989)]. In this comparison, the solar helium abundance was used, while an adjustment of 0.06 in M_V, obtained from Equation 4.4, was applied to account for the non-solar metallicity value of -0.04 for M67 (Hobbs and Thorburn, 1991).

The absolute magnitude of the clump changes with metallicity according

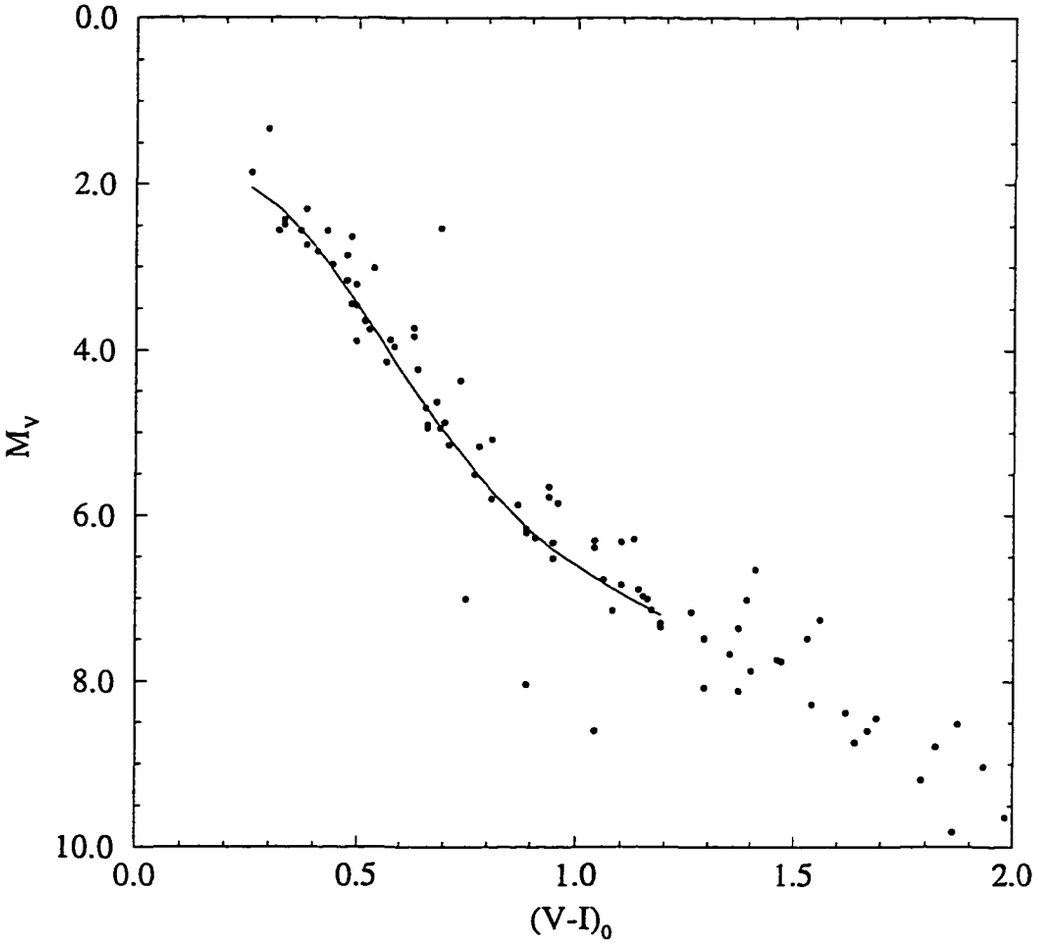

Figure 4.21: CMD for the Hyades (Reid, 1993). The solid line is the ZAMS calibration obtained as described in the text. The CMD has been adjusted in absolute magnitude by $\delta M_V([Fe/H]) = -0.19$ to account for the Hyades' metal abundance. A reddening value and distance modulus of $E(B-V) = 0.0$ and $(m - M)_V = 3.35$, respectively, were adopted.

to the relation

$$M_V = 0.19[Fe/H] + 1.0 \tag{4.8}$$

(Dorman, 1990; Dorman, 1993). Thus, the clump stars in solar metallicity clusters should reside at $M_V = 1.0$, while those in clusters more metal-poor or metal-rich than solar should possess absolute magnitudes brighter or fainter than 1.0, respectively (note that the above relation was derived from theoretical models). According to the above relation, the metallicity of M67 results in a clump absolute magnitude of $M_V = 0.99$.

A discussion of the uncertainty in derived ages from uncertainties in the cluster parameters, such as distance modulus, will be presented in Chapter 5. However, it is worth mentioning here that the uncertainties in the distance moduli given below, as determined from the uncertainties in the clump magnitudes, lead to uncertainties in the cluster ages of about 10%.

NGC 2141

The average magnitude of the clump for this cluster is $V_{clump} = 14.90 \pm 0.07$. Using the clump magnitude for M67 given above, a magnitude difference of $\Delta V_{clump} = 4.36 \pm 0.09$ was obtained. The distance modulus of M67 given above yielded an initial estimate of $(m - M)_V = 13.86 \pm 0.13$ for NGC 2141.

NGC 2141 and M67 differ in metallicity by about $\Delta[Fe/H] \sim 0.35$ dex. While the red giant clump is not very sensitive to differences in metallicity, there is enough difference between these two clusters to alter the clump absolute magnitude by a non-negligible amount. Equation 4.8 was used to obtain $M_{Vclump} = 0.92$ for NGC 2141. The actual apparent distance modulus was found by subtracting the difference between this value and the one derived for M67 from the initial estimate of the distance modulus. Thus,

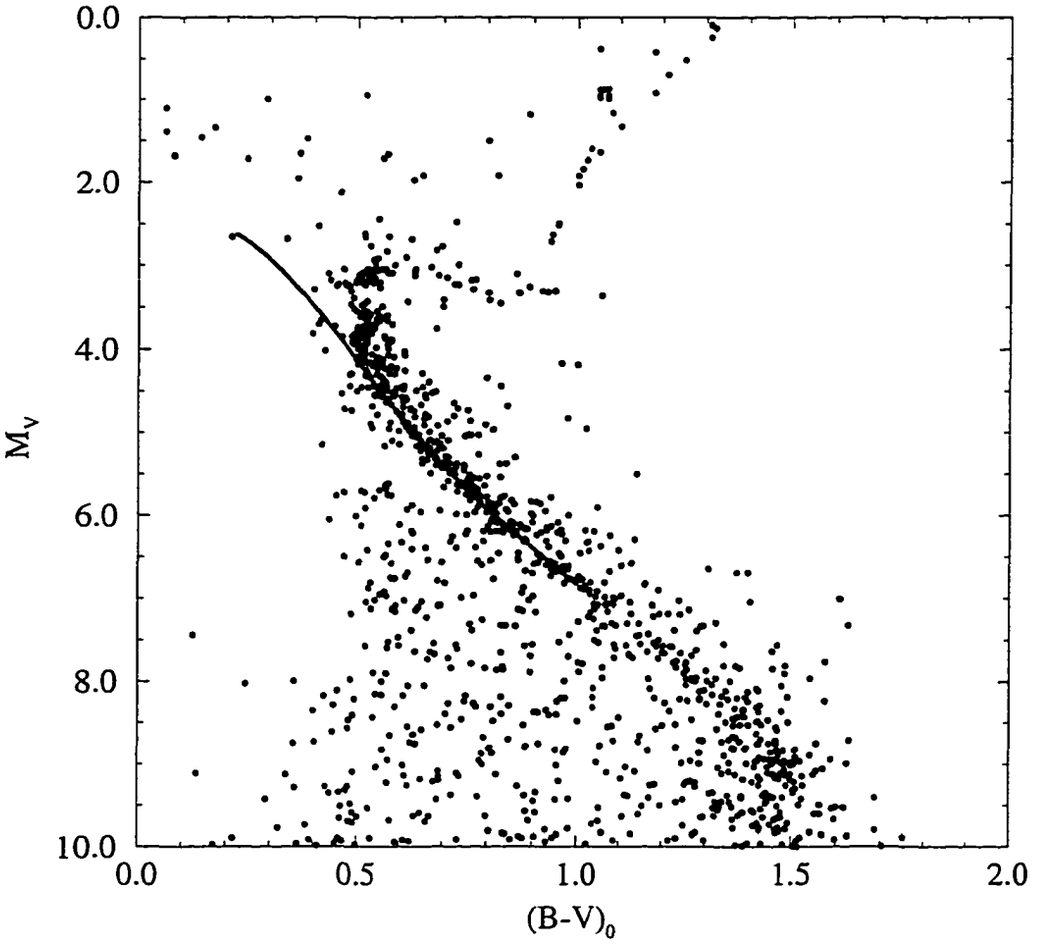

Figure 4.22: CMD for M67 (Montgomery et al., 1993). The solid line is the VandenBerg and Poll (1989) empirical ZAMS calibration, adjusted in absolute magnitude by $\delta M_V([Fe/H]) = 0.06$ to account for the metallicity of M67. The by-eye comparison yields a distance modulus for M67 of 9.50 ± 0.10 for a colour excess of $E(B-V) = 0.04$.

$(m - M)_V = 13.93 \pm 0.13$ for NGC 2141.

NGC 7142

As is apparent from its CMD (Figure 4.6), there is a paucity of clump stars, which makes the clump comparison method unreliable. Crinklaw and Talbert (1991) obtained a distance modulus for this cluster by fitting the cluster main sequence with Mermilliod's (1981) ZAMS. However, since the scatter in the CMD main sequence is so great, little confidence can be placed on their value of $(m - M)_0 = 11.4 \pm 0.9$ (note that the value they quote has been corrected for a colour excess of $E(B - V) = 0.41$).

Three cluster members observed by Friel and Janes (1993) reside at $V \sim 14$ in the cluster CMD. It was assumed that these stars (along with others not observed by the above authors) mark the location of the clump at $V = 14.0 \pm 0.1$. Comparison with M67's mean clump magnitude yielded a magnitude difference of $\Delta V_{clump} = 3.46 \pm 0.13$. Taking into account the distance modulus of M67 resulted in $(m - M)_V = 12.96 \pm 0.16$ for NGC 7142.

NGC 6819

The average clump magnitude for this cluster is $V_{clump} = 13.12 \pm 0.07$, yielding a magnitude difference between it and M67's clump of $\Delta V_{clump} = 2.58 \pm 0.09$ and an apparent distance modulus of 12.08 ± 0.13. The difference in clump absolute magnitude between this cluster and M67 was used to correct the apparent distance modulus above to the final value of $(m - M)_V = 12.10 \pm 0.13$.

NGC 6791

Garnavich et al. (1994) obtained a distance modulus of $(m-M)_V = 13.65$ by matching the average clump magnitude with the clump in M67. This value assumes the clump stars in both clusters have the same mean intrinsic luminosity, as well as the same metallicity. Given that the metal abundance of NGC 6791 is higher than that of M67 [recall $[Fe/H] = 0.19 \pm 0.19$ for NGC 6791, compared to $[Fe/H] = -0.04 \pm 0.12$ for M67 (Hobbs and Thorburn, 1991)], a value smaller by about 0.1 magnitudes was preferred.

A value of $(m-M)_V = 13.56$ is obtained if the apparent magnitude of the clump is assumed to be $V_{clump} = 14.6$ and the clump magnitude and distance modulus of M67 are as given above. Taking into account the change in clump absolute magnitude due to the metallicity of NGC 6791 yields a final value of $(m-M)_V = 13.52$, in good agreement with that found by Garnavich et al. (1994), and Tripicco et al. (1995) who obtain $(m-M)_V = 13.52$ and 13.49 from two independent data sets (Kaluzny and Udalski, 1992; Montgomery et al., 1994b).

4.2.3 Differential Reddening

Open clusters in certain regions near the Galactic plane may be subject to differential reddening. This effect manifests itself in a broadening of the main sequence, especially if the cluster is large in angular extent. Two clusters in this study, NGC 7142 and NGC 2141, show signs of differential reddening. In an attempt to quantify this effect, CMDs of the clusters' core regions were produced, then CMDs of various sections compared with them. Results for each cluster are discussed below.

NGC 2141

Burkhead et al. (1972) determined a mean colour excess from several stars which had been observed photoelectrically. All were assumed to be main-sequence stars unless their positions in the CMD and $(U-B)$ versus $(B-V)$ diagram indicated otherwise. Two stars (believed to be cluster members on the basis of their locations in the CMD and two-clour diagram) in one part of the cluster yielded a mean colour excess of $E(B-V) \sim 0.38$, while two other possible cluster members in another part yielded $E(B-V) \sim 0.24$, indicating possible differential reddening within the cluster.

An estimate of the amount of differential reddening was made using the present data's centre field. The central 47 arcmin^2 of the cluster was selected as the core, and quadrants of the centre field chosen as comparisons. Figure 4.23 plots mean (by-eye) fiducials of the core region (solid) as well as the four quadrants (long-dashed, dot-dashed and short-dashed for the upper-left, upper-right, lower-left and lower-right quadrants, respectively. Note that both the third and fourth quadrants are represented by the short-dashed line). A mean range of about 0.07 magnitudes in $\Delta(V-I)$ was evident, which is similar to the estimate of Burkhead et al. (1972). Differential reddenings and extinction corrections $[\Delta(V-I), \Delta V]$ were determined as follows: $(+0.05, +0.12)$, $(-0.02, -0.05)$, $(+0.02, +0.05)$ and $(+0.02, +0.05)$ for the upper-left, upper-right, lower-left and lower-right quadrants, respectively.

NGC 7142

Several authors have found indications of variable reddening across the

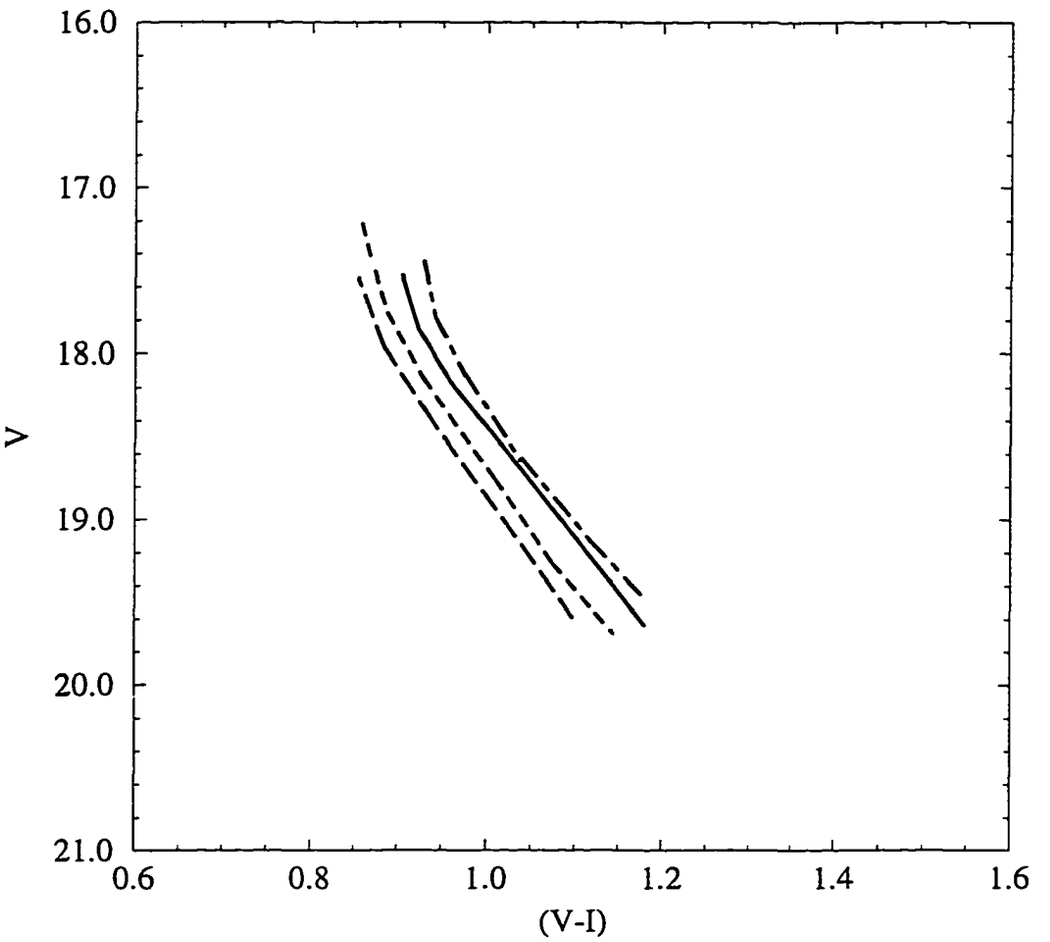

Figure 4.23: Fiducials of NGC 2141's core region (solid line) and upper-left (long-dashed), upper-right, (dot-dashed), lower-left and lower-right (short-dashed) quadrants.

face of this cluster (van den Bergh and Heeringa, 1970; Sharov, 1965; Jennens and Helfer, 1975). Crinklaw and Talbert's (1991) photometry indicates a differential reddening of $\Delta E(B-V) \approx 0.1$, and they suggest that the width of the main sequence could be due in part to a binary star main sequence. To test for differential reddening, they examined the colours of four galaxies present and near each other on their frames. While the colours for the elliptical galaxy were typical, the bright spiral seemed anomalously red, indicating some localized reddening difference. They also divided their main sequence stars into groups on the basis of their colours, and then examined the distribution of the stars in the cluster fields. They did not see a correlation between the colour and location in the cluster, which indicated no large-scale changes in absorption across the face of the cluster.

Several different approaches were taken to investigate the effect using the present data. First, quadrants about 4 arcmin on a side were chosen, and CMDs produced as for NGC 2141. Three quadrants were similar but the fourth showed a displacement of about 0.08 mag in $(V-I)$. Vertical strips 2 arcmin wide showed a spread of 0.08 mag, while horizontal strips 3 arcmin wide showed a spread of 0.08 mag as well. However, when the various sections were shifted appropriate amounts, the combined CMD did not look much better than the original one with unshifted data. It appeared that heavy field star contamination was creating the spread, so the size of the region being studied was reduced, and three segments, one core region 5 arcmin on a side, and two smaller regions displaced from the core by approximately 3 arcmin were used. One region needed adjustment of 0.02 mags in colour, but since the resulting CMD showed little improvement over the unshifted one, it was not used in subsequent analyses.

4.2.4 Mean Cluster Reddening

Initially, mean reddenings were redetermined for all four clusters using $(V-I)$ versus $(J-H)$ diagrams, Bessell and Brett's (1988) intrinsic colours for giants (obtained from observations of standard stars), and Rieke and Lebofsky's (1985) interstellar extinction law, in which $E(J-H) = 0.33E(B-V)$. Dean et al.'s (1978) $E(V-I) = 1.25E(B-V)$ relation was used as well. A conscious effort was made to select only member stars [mostly clump and upper giant branch stars observed by Friel and Janes (1993), Garnavich et al. (1994) and Sanders (1972)]. However, the reddenings all were too high when compared to other values published in the literature. Incorrect results were obtained even when other colour combinations were used. Since in all cases the reddening lines were nearly parallel to the intrinsic two-colour relations, the results were abandoned and the main sequence fitting method was used to obtain a reddening value for each cluster.

The main sequence fitting method uses the distance moduli obtained earlier and the ZAMS relations given above. Each cluster CMD was adjusted in apparent distance modulus, and then shifted horizontally to the blue until the cluster ZAMS coincided with the appropriate ZAMS relation. VandenBerg and Poll's (1989) semi-empirical ZAMS was used with the $(V, B-V)$ CMD of NGC 6819, while the ZAMS derived from the Hyades main sequence was used with the $(V, V-I)$ CMDs of the other three clusters. In each case, corrections to M_V for cluster metallicity according to Equation 4.5 were made. Table 4.6 contains the final reddenings as well as apparent distance moduli and corresponding true distances. Uncertainties in the reddening values were obtained by estimating (by eye) the amount of shift required to move the cluster main sequence about the ZAMS until a match no longer occurred, and factoring in the uncertainty in the distance modulus. Figure 4.24 displays

Table 4.6: Reddening determinations as described in the text. Apparent distance moduli obtained earlier, and corresponding true distances are included as well.

Cluster	$E(B-V)$	$(m-M)_V$	d (kpc)
NGC 2141	0.32 ± 0.04	13.93 ± 0.13	3.9 ± 0.3
NGC 7142	0.29 ± 0.04	12.96 ± 0.16	2.6 ± 0.2
NGC 6819	0.11 ± 0.03	12.10 ± 0.13	2.2 ± 0.2
NGC 6791	0.23 ± 0.03	13.52 ± 0.13	3.6 ± 0.2

the fits of the CMDs to the semi-empirical ZAMS relations.

The reddening values in Table 4.6 agree with those derived in previous studies. For example, Burkhead et al. (1972) found $E(B-V) = 0.30$, which agrees with the value (0.32) determined in this study, while the reddening for NGC 7142 found here ($E(B-V) = 0.29$) lies in the range stated in Chapter 1 (0.18 to 0.41). Canterna et al. (1986) obtained $E(B-V) = 0.15$ for NGC 6819, which is somewhat higher than that found here (0.11), yet still within the uncertainty. Finally, Tripicco et al. (1995) obtained a reddening in the range $0.19 < E(B-V) < 0.24$, in agreement with that found here (0.23), while Garnavich et al. (1994) derived a reddening of 0.19 for NGC 6791, somewhat lower than the value determined above.

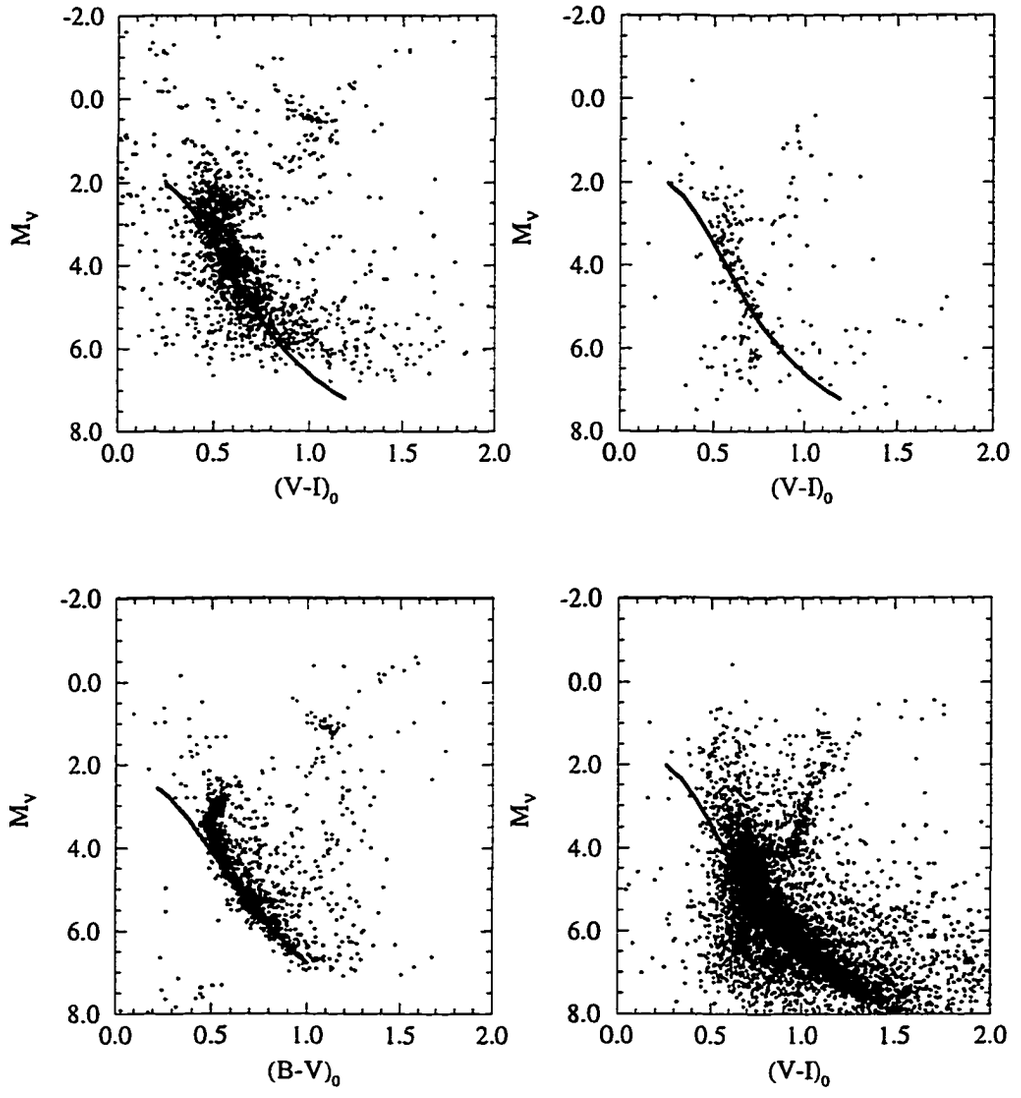

Figure 4.24: The CMD of each cluster has been fit to one of the semi-empirical ZAMS relations described in the text. The upper left and upper right plots correspond to NGC 2141 and NGC 7142, respectively, while the lower left and right are of NGC 6819 and NGC 6791, respectively. The ZAMS is shown as a solid line. In order to match the cluster main sequences to the ZAMS, the CMDs have been shifted by the following amounts: $\delta(V-I) = 0.40$, 0.37 and 0.29 for NGC 2141, NGC 7142 and NGC 6791, respectively, while $\delta(B-V) = 0.11$ for NGC 6819. These values correspond to the reddenings given in Table 4.6.

Chapter 5

Discussion

This chapter presents a brief description of stellar evolutionary theory, and its relation to the present work. Various methods of age determination will be discussed and applied to the cluster data. The $(V-K)$ photometry presented in the previous chapter will be used to obtain physical stellar parameters such as effective temperatures, bolometric corrections, absolute bolometric magnitudes and luminosities. These parameters will be used to transform the cluster giant branch CMDs to the theoretical (M_{bol}, T_{eff}) plane. The resulting HR diagrams will be compared to a selection of the ones constructed by Houdashelt et al. (1992). Finally, a brief discussion of how these observations tie in to the history of our galaxy will be given.

5.1 Stellar Evolutionary Theory

In order to obtain information about the relative evolutionary status of stars of different masses, the observed CMD is compared to sets of theoretical isochrones, which are constructed in the following manner. The equations of stellar structure, which describe the run of pressure, temperature, radius and luminosity in the star, are solved with certain boundary conditions: at $m = 0$, where m is the mass, both the radius and luminosity equal zero,

and the photospheric temperature and pressure must be consistent with the requirements imposed by a model stellar atmosphere. The chemical composition, mass of the star and the mixing length parameter α are required as initial conditions. The density, opacity, and energy generation rate, as functions of the temperature, pressure and chemical composition, complete the ingredients required for the calculations. In the past, simple analytic formulae for the opacity were used in the calculations, but high speed computers have allowed the computation of highly detailed opacity tables (Rogers and Iglesias (1992); Iglesias et al. (1992), for example), which are interpolated for any temperature, density and chemical composition. The solution of the equations yields a series of evolutionary sequences (VandenBerg, 1985) for stars of different masses (Figure 5.1, upper plot). These sequences plot a star's luminosity and effective temperature as it ages.

Theoretical isochrones representing the main sequence and later stages of evolution are obtained by connecting points on the evolutionary tracks at a specific time after the onset of core hydrogen burning (Figure 5.1, lower plot), and display the properties of the models for a range of mass at one particular time. The isochrones are calibrated by constructing a standard solar model [a one solar-mass star evolved to the present age of the sun (4.6 Gyr, from Stix (1989)) and matching it in effective temperature and luminosity]. Note that for a given metal abundance the main sequence (region 1 on Figure 5.1) location does not change, regardless of age, while the turnoff (region 2) and subgiant branch (region 3) are very sensitive to age. The subgiant branch's age sensitivity manifests itself in changes in slope and brightness.

For ease of comparison with observations, the isochrones may be transformed to the observational plane using predicted effective temperature/colour scales and bolometric corrections. Provided the observational CMD reaches

the main-sequence turnoff region, the isochrones may be used to obtain an age for the cluster. This will be discussed in greater detail in the next section. The isochrones as described above do not fit observed data perfectly, due in part to observational uncertainties, but also to problems in the theoretical models, some of which are described below. In old clusters the turnoff region, subgiant and giant regions are used in the comparison of theoretical isochrones, but the stars in these regions have convective envelopes, which still cause difficulties in model calculations due to the lack of suitable convection theory (VandenBerg, 1985). Recall the mixing length theory (Böhm-Vitense, 1958) is used for the treatment of envelope convection, and is a crude approximation at best. As well, different methods are used to obtain the surface pressure boundary condition for the solution of the stellar structure equations, which lead to differences in the models. Recently, Bell (1992) has shown that model atmospheres are unable to reproduce the near-infrared colours of giants, which may be due to uncertainties in the adopted opacities.

While IR data are not a panacea, reliable effective temperatures and bolometric corrections derived from the observations will provide accurate effective temperature/colour scales for use with the isochrones, important constraints on the construction of stellar models and checks on the consistency of the different models and evolutionary sequences available.

5.2 Methods of Determining Cluster Ages

Previous age estimates for the clusters in this study ranged from 2-12 Gyr. Recall NGC 2141 had no firm age estimate, but was suspected to be of intermediate age (*i.e.* 4 Gyr) based on CMD morphology, while estimates by several authors of the age of NGC 6791 ranged from 7-12 Gyr. The age of NGC 6819 varied from 2 Gyr (Lindoff, 1972) to about 4 Gyr via the

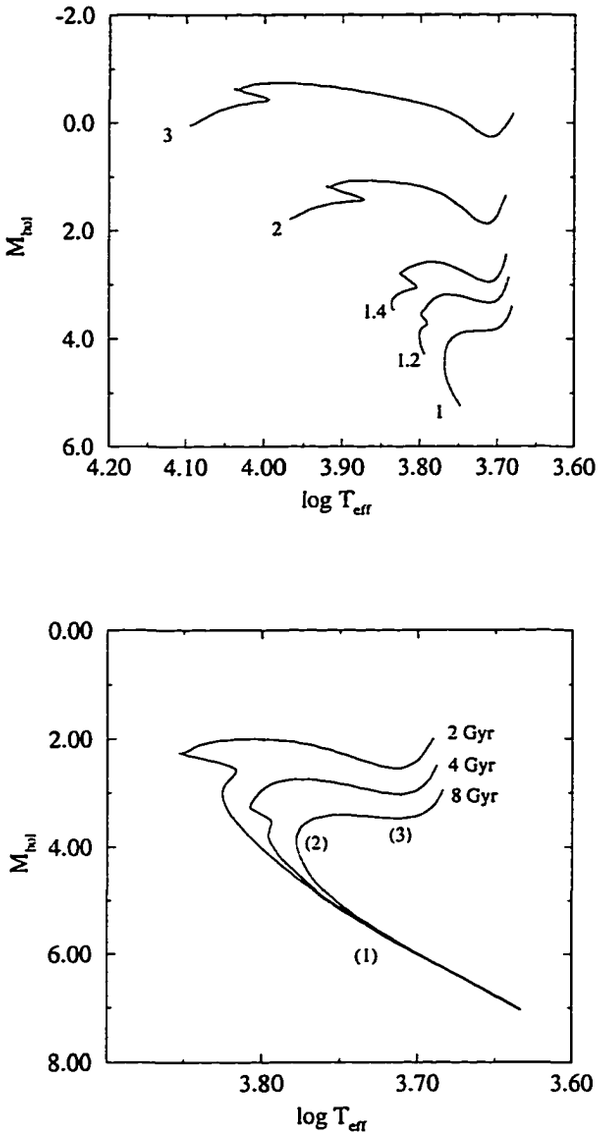

Figure 5.1: Evolutionary tracks for stars having masses (in units of solar mass) as indicated (upper plot), and 2, 4, and 8 Gyr theoretical isochrones for solar metallicity. Bracketed numbers refer to key locations as described in the text. Both figures are adapted from VandenBerg (1985).

MAR method (described below) developed by Anthony-Twarog and Twarog (1985). Finally, NGC 7142's age was estimated at 4 Gyr via the MAR method (Crinklaw and Talbert, 1991). The ages of the clusters are redetermined below via two different methods.

5.2.1 Isochrones and Cluster Ages

In this method, theoretical isochrones, which have been transformed to the observational plane (*i.e.* $M_V, (V-I)_0$, for the majority of this work), are compared to cluster CMDs. Various observational parameters are needed to establish an estimate of the age – the distance modulus $(m-M)$, colour excess $E(B-V)$, heavy element abundance Z and helium abundance Y. The distance modulus and colour excess adjust the cluster CMD to the $M_V, (V-I)_0$ plane of the isochrone, while Y and Z dictate which set of isochrones are appropriate. Note that this method does not really "fit" the isochrones to the observations; the isochrone which best matches the main sequence, giant branch and the slope of the subgiant branch yields the age of the cluster. Current evolutionary tracks make use of later stages of evolution also, and thus the locations of the red giant clump and asymptotic giant branch are available for comparison as well (Castellani et al., 1992; Bertelli et al., 1994).

Each observational parameter introduces uncertainty in the final age, with the uncertainties in the distance modulus and colour excess as the major contributors. It is difficult to measure the colour excess to better than ± 0.02 mag, and systematic differences between methods used to determine metallicity result in $\delta[Fe/H] \sim 0.25$ dex (Kraft, 1979). Solar Y values range from 0.24 to 0.27 while stellar models have varied Y from 0.2 to 0.3 (VandenBerg, 1983; VandenBerg, 1985). A breakdown of the effect of varying each parameter on the age is given in Table 5.1.

Table 5.1: Typical systematic uncertainties found in each parameter, and their contribution to the total uncertainty in the age. For example, an increase of 0.3 mag in the distance modulus will decrease the age estimate by 20%. Age uncertainties are from VandenBerg (1983), VandenBerg (1985) and Flannery and Johnson (1982).

Parameter	δ	δ age (%)
$(m-M)_V$	+0.3 mag	−20
$E(B-V)$	+0.02 mag	−10-15
$[Fe/H]$	+0.2 dex	−7
Y	+0.03 dex	−10

In addition, the presence of a binary star main sequence may introduce uncertainties in the derived age of the cluster. A binary pair consisting of two main sequence stars of equal mass will reside 0.75 mag above the single star main sequence in the CMD, and an entire sequence of such stars will run parallel to the single star sequence and continue up through the turnoff region populated by single stars. This effect may cause confusion in ascertaining the true location of the turnoff, and may lead the investigator to choose an isochrone of younger age, especially if the scatter in the main sequence is enough to hide the distinction between the single and binary star populations.

The applicability of different sets of isochrones was investigated in this study. The ones by Castellani et al. (1992) were inappropriate since they were derived for $(B-V)$ only, and did not have ages or metal abundances suitable for the clusters being studied here. The VandenBerg (1985) isochrones produced poor results for the younger clusters since they were not precisely normalized to the sun and thus needed correction before they could be used, and did not have appropriate metallicities for some of the clusters. The isochrones which fit the cluster CMDs best are by Bertelli et

al. (1994). These isochrones cover a wide range of chemical compositions ($0.008 \leq Z \leq 0.05$) and ages. Also, they have been developed for use in several passbands ($UBVRIJHK$), and include the location of the red giant clump and other late stages of evolution. Finally, they make use of improved physics such as new radiative opacities and a treatment of convective overshooting. Isochrones derived by Dowler and VandenBerg (1996) were used as well, since some of them also allow for convective overshooting as well as viscous dissipation (which limits the amount of overshooting). The overshooting isochrones fit equally as well as the Bertelli et al. (1994) ones, for two of the clusters.

5.2.2 The MAR Method

The MAR (morphological-age-ratio) method was developed by Anthony-Twarog and Twarog (1985), and makes use of BV CMD morphology (refer to Figure 5.2). The MAR parameter is defined as

$$\mathrm{MAR} \equiv \frac{\Delta V}{\Delta(B-V)}, \tag{5.1}$$

where ΔV is the difference in magnitude between the red giant branch clump (point "a" on Figure 5.2) and the brightest point of the cluster turnoff ("b"), and $\Delta(B-V)$ is the difference in colour between the red giant branch at the magnitude of the clump ("c") and the bluest part of the turnoff ("d"). Anthony-Twarog and Twarog (1985) note that in some of the clusters used for calibration, a hook feature in the CMD and the presence of a small number of stars above the actual turnoff caused some ambiguity as to which magnitude should be used. In those cases, the hook and upper stars were ignored. The ratio defined above is reddening free, and only weakly dependent on metallicity (affecting both differences in the same sense). It also makes

maximum use of the age effect since ΔV increases while $\Delta(B-V)$ decreases with increasing age.

Once the MAR parameter is determined, the age t, in Gyr, is given by

$$t = 1.4\text{MAR}. \tag{5.2}$$

Anthony-Twarog and Twarog (1985) used seven well-studied open clusters having reliable main-sequence photometry and accurate giant branch data, and ages derived from main-sequence fitting to (arbitrarily chosen) theoretical isochrones (which did not allow for convective overshooting). The calibration constant given above was obtained by estimating (by eye) the slope of a straight line drawn through the data. They stress that the MAR parameter should be used to obtain relative ages only, since actual ages will change if different isochrones are used in the calibration. Also, this method should be used only for clusters with ages within the range of the calibration clusters.

5.3 Cluster Ages

5.3.1 Ages via the MAR Method

The MAR parameter and age were determined for each cluster (except NGC 6791, for reasons which will be explained later). Since only NGC 6819 was observed through the B filter, observations found in the literature were used to calculate the MAR parameter and age for the other clusters.

Crinklaw and Talbert (1991) estimated the age of NGC 7142 as between 3.5 and 4.5 Gyr. The uncertainty arises from the fact that this cluster's CMD lacks a distinct red giant clump. In an effort to ascertain the location of the clump, the $(V, V-K)$ and $(K, V-K)$ CMDs were examined. It was assumed the three member stars which reside at $V \sim 14$ mark the location

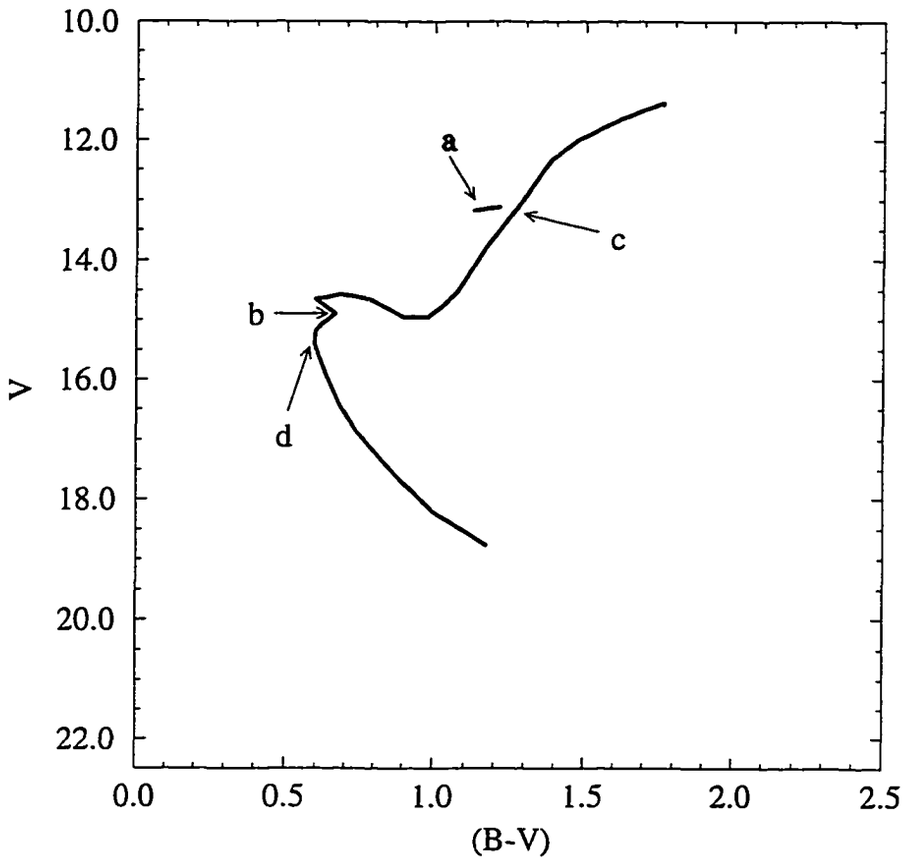

Figure 5.2: Schematic diagram of a cluster CMD, complete with blue hook near the turnoff and a red giant clump. The features used in the determination of the MAR parameter are indicated by the letters.

of the clump. Thus, from Crinklaw and Talbert's (1991) CMD, the colour of the giant branch at the level of the clump is $(B-V) \sim 1.5$. Adopting 15.5 and 0.9 mag for the turnoff magnitude and bluest part of the turnoff, respectively, yields 2.5 for the MAR parameter and an age of 3.5 Gyr. If the apparent magnitude of the clump is brighter (relative to the turnoff) by 0.5 mag, and the turnoff magnitude and colour are adjusted to 15.75 and 0.85 mag, respectively, the age increases to 4.2 Gyr.

NGC 6819's *BV* CMD, presented in Chapter 4, was used to determine the age. With a clump magnitude and giant branch colour of 13.2 and 1.28 mag, respectively, a turnoff magnitude of 14.8 and a turnoff colour of 0.6 mag, MAR = 2.35, yielding an age of 3.3 Gyr. Again, if extremes in the values above are taken (clump magnitude of 13.0, turnoff magnitude and colour of 14.5 and 0.55, respectively) the age decreases to 2.8 Gyr.

The only *BV* CMD of NGC 2141 was constructed by Burkhead et al. (1972) from photographic and photoelectric photometry. In this CMD, the clump is well-defined at $V \sim 14.8$ and while the giant branch is sparse, its colour at the level of the clump was assumed to be $(B-V) \sim 1.5$. A great deal of scatter was present at the location of the turnoff. Hence it was difficult to ascertain the correct turnoff magnitude and bluest part; estimates were made at 16.7, and 0.70, respectively. These values resulted in a MAR parameter of 2.4 and an age of 3.3 Gyr. If the clump magnitude is fainter by 0.2 mag, and turnoff magnitude and colour changed to 16.5 and 0.6, respectively, an age of 2.5 Gyr is obtained. Clearly, the uncertainty of the location of the turnoff is the major source of uncertainty in the age in this case.

The MAR method was not attempted for NGC 6791, since the cluster is believed to be older than the oldest cluster (Melotte 66, with an age of 6.5 Gyr) used in the calibration, and the metal abundance of NGC 6791 is

higher (+0.19, compared to an average of −0.2 for the calibration clusters).

As stated before, while this method shouldn't be used to determine absolute ages, since it is dependent on the isochrones used to derive the ages of the calibration clusters, it is useful in ranking the clusters according to age, and it will be interesting to see how the ages and ranking found here compare with those as determined from isochrone fitting.

5.3.2 Ages from Isochrones

After examining the options available for comparing the CMDs to theory, the Bertelli et al. (1994) and Dowler and VandenBerg (1996) isochrones were used. Metal abundances, colour excesses and distance moduli adopted were those given in the previous chapter. In all cases, the cluster CMD was shifted according to $E(B-V)$ and $(m-M)_V$, and the isochrones plotted as is on the shifted CMDs.

NGC 6791

The paucity of greater-than-solar metallicity isochrones made comparison of the cluster CMD with theory difficult. The usual procedure involves fitting solar metallicity isochrones and then making allowances for the metal abundance of the cluster. Of course, this produces large uncertainties in the derived age of the cluster. Initially, Bertelli et al. (1994) isochrones having ages of 8 and 10 Gyr and metallicities of $Z = 0.02$ (solar) and $Z = 0.05$ were compared with the CMD of NGC 6791. All the fits were unsatisfactory, and greater-than-solar metallicity isochrones by Dowler and VandenBerg (1996) ($Z = 0.03$) were not old enough to work with this cluster.

Tripicco et al. (1995) have contributed to the solution of the above prob-

lem by generating 8, 10 and 12 Gyr isochrones for $[Fe/H] = 0.15$. They compared their isochrones to two independent sets of observations (Kaluzny and Udalski, 1992; Montgomery et al., 1994b) and found an age of 10 Gyr from both sets, for distance moduli of $(m - M)_V = 13.52$ and 13.49, respectively, and a colour excess of $0.19 < E(B - V) < 0.24$, provided the metal abundance is in the range $0.44 > [Fe/H] > 0.27$, somewhat higher than has been found in previous studies. One of their plots (Figure 5.3) has been included here for completeness. The data consist of 445 stars from Kaluzny and Udalski's (1992) sample whose probabilities for membership, based on proper motions (Cudworth, 1994), are greater than 50%. The 10 Gyr isochrone matches the turnoff, subgiant branch and unevolved main sequence well, and the location of the zero-age horizontal branch forms a lower boundary to the clump stars. The distance modulus and reddening required for the fit provide a good check on the consistency of the results, and support the results obtained in this study.

NGC 6819

The Bertelli (1994) isochrones for ages ranging from 2 to 4 Gyr and a metal abundance of $Z = 0.02$ were superposed on the CMD of NGC 6819. The best fit, shown in Figure 5.4, is for a 2.5 Gyr isochrone. Even though the isochrone appears to be too red by 0.03 mag, the turnoff and red giant clump are matched well by this isochrone. Presumably this is due to the inclusion of overshooting in the models.

A 3 Gyr solar metallicity isochrone was obtained from Dowler and VandenBerg (1996) and compared to the $M_V, (B-V)_0$ CMD of NGC 6819. This isochrone treats convective overshooting as well, but whereas the Bertelli isochrones use a fixed value for the extension of the convective core (in terms

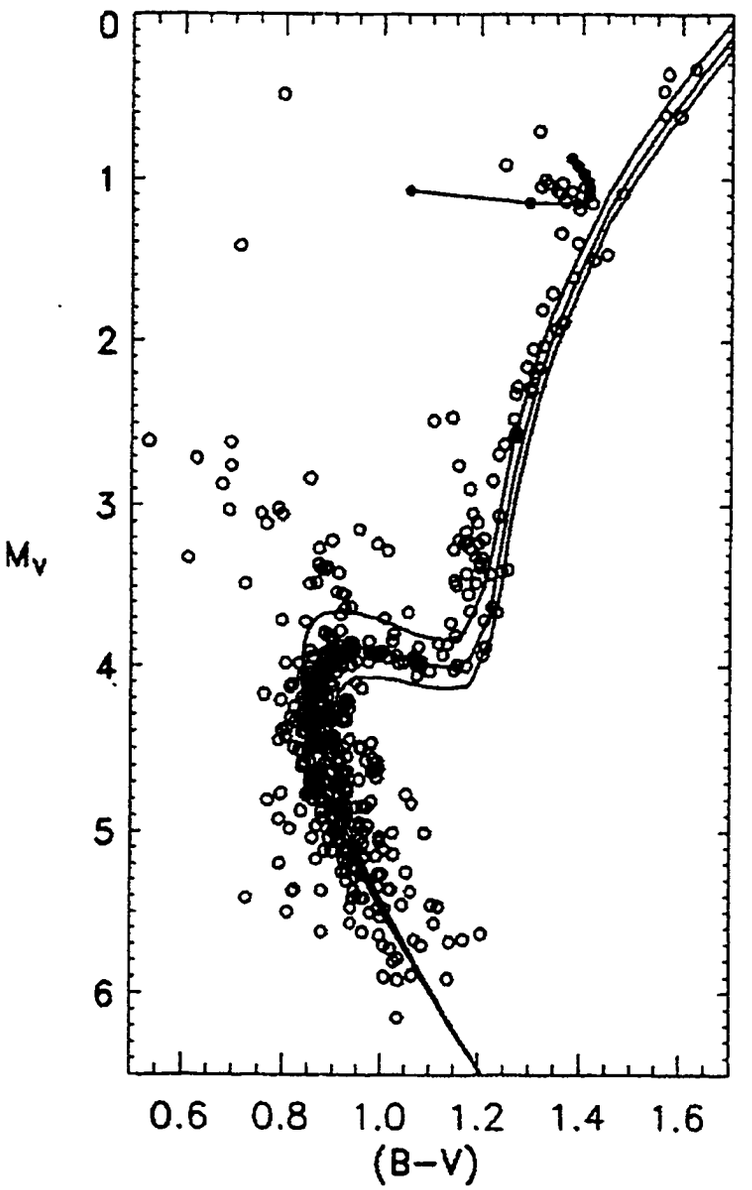

Figure 5.3: 8, 10 and 12 Gyr isochrones and zero-age horizontal branch for $[Fe/H] = 0.15$, superposed on the CMD of NGC 6791. From Tripicco et al. (1995).

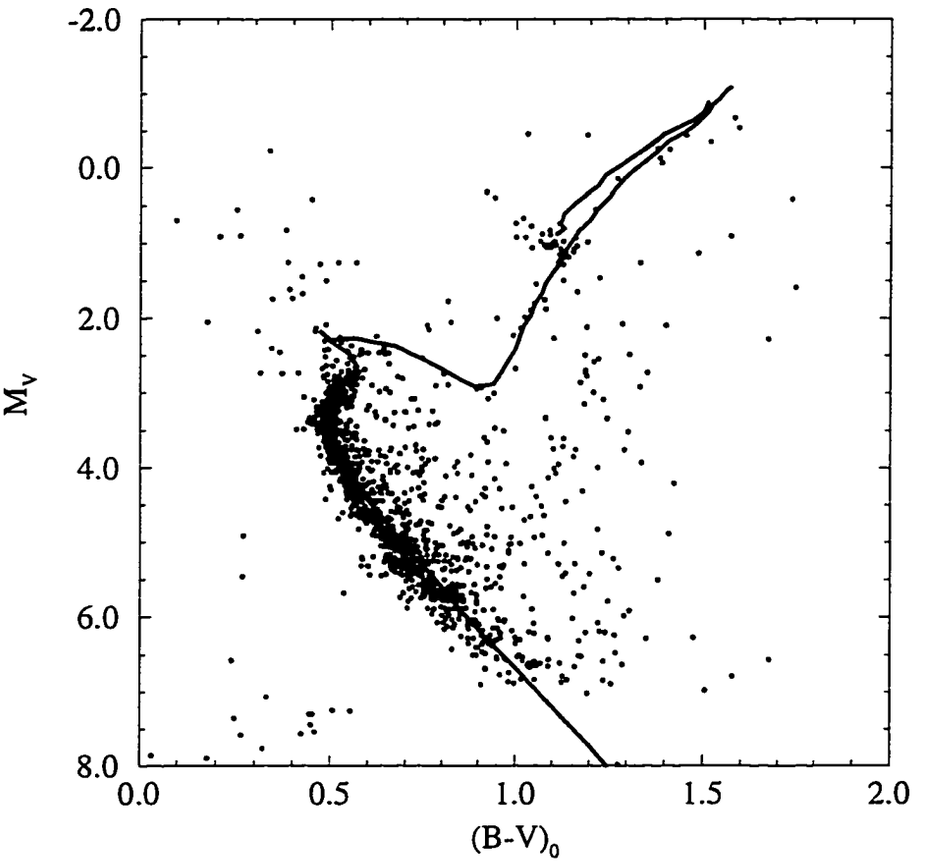

Figure 5.4: A 2.5 Gyr isochrone ($Z = 0.02$, $Y = 0.28$) from Bertelli et al. (1994) is plotted on the CMD of NGC 6819. The turnoff and red giant clump are fit well by this isochrone.

of the pressure scale height), the Dowler isochrone varies in the amount of overshooting. Note that the subgiant branch does not extend to sufficiently red colours and the lower main sequence is not fit well. The comparison is shown in Figure 5.5.

The turnoff region was enlarged and a solar metallicity, 2.5 Gyr canonical isochrone [dashed line, from Dowler and VandenBerg (1996)] was plotted with the overshooting isochrone (solid line) used in the previous plot (Figure 5.6). Clearly the overshooting isochrone provides a superior fit throughout the turnoff region.

A plot of the comparison between the Bertelli et al. (1994) and Dowler and VandenBerg (1996) models is shown in Figure 5.7. The upper plot compares the evolutionary tracks (luminosity in solar units versus the logarithm of the effective temperature in Kelvin). The tracks agree at the termination of the main sequence, and throughout most of the subgiant branch after the overshooting hook, but neither the turnoff between $\log T_{eff} = 3.8$ and 3.85 nor the hook itself coincide. As well, the base of the giant branch occurs at different temperatures. These discrepancies are translated to the isochrones on the observational plane (lower plot of Figure 5.7). The difference in the main sequence locus presumably is due to uncertainties in the colour transformation.

NGC 2141

The Bertelli et al. (1994) isochrone which best fits the data, based on a reddening and distance modulus of $E(V-I) = 0.4$ and $(V-M_V) = 13.93$, has a chemical composition of $Z = 0.008$ and an age of 2.5 Gyr. Figure 5.8 displays the CMD and the isochrone. A comparison with a canonical isochrone

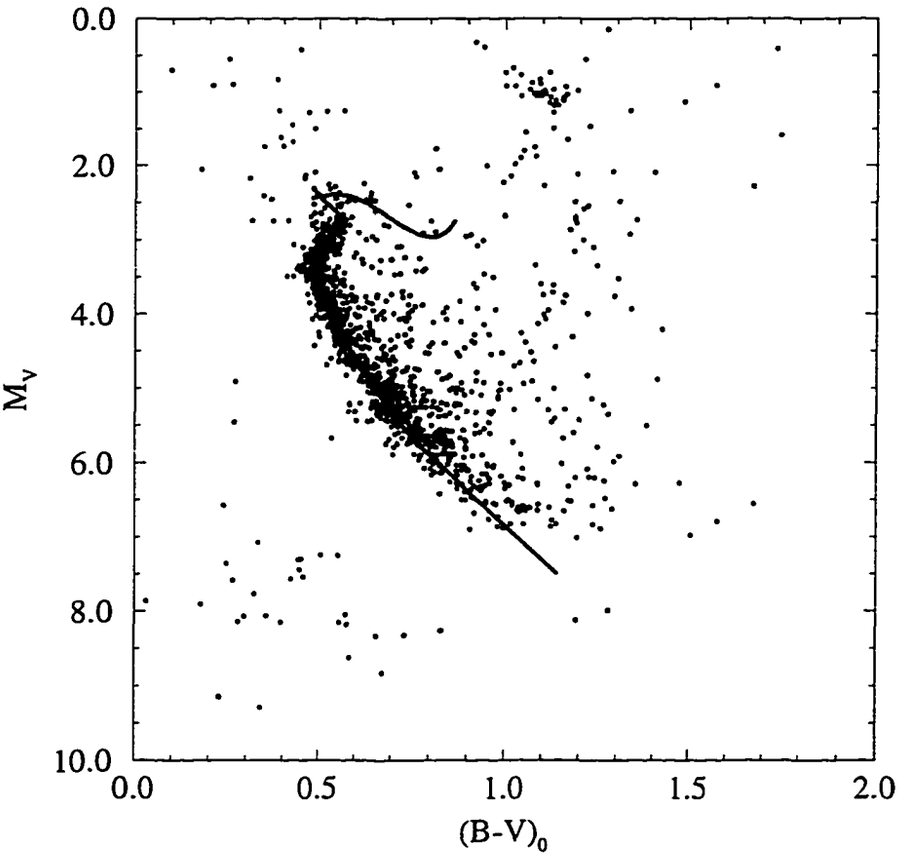

Figure 5.5: A 3 Gyr solar metallicity isochrone from Dowler and VandenBerg (1996) is superposed on the CMD of NGC 6819. This fit is comparable to that obtained with the Bertelli et al. (1994) isochrones through the main sequence and subgiant phases.

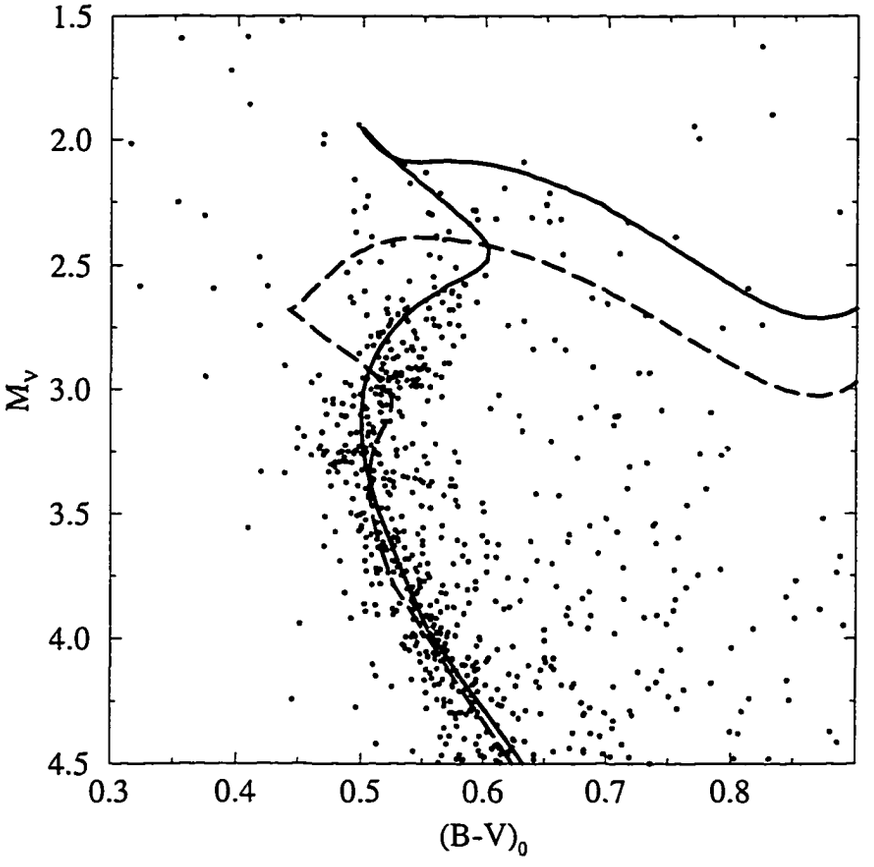

Figure 5.6: Solar metallicity overshooting (solid line) and canonical (dashed line) isochrones having ages of 3 and 2.5 Gyr, respectively, from Dowler and VandenBerg (1996) are superposed on the CMD of NGC 6819. Note the superior match between the overshooting isochrone and the CMD.

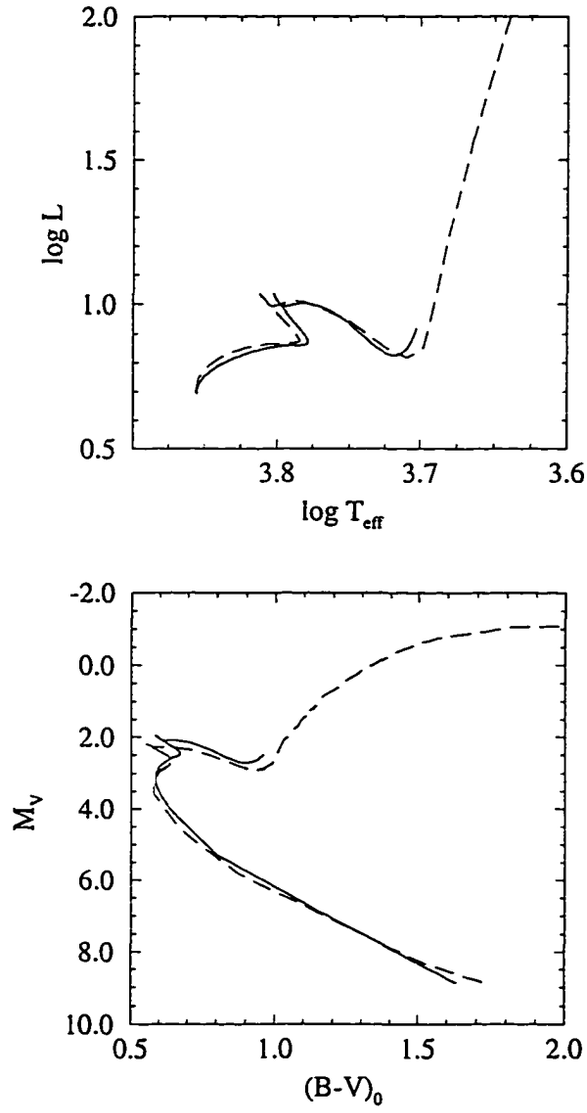

Figure 5.7: A comparison of the evolutionary tracks (upper plot) and corresponding isochrones (lower plot) from Dowler and VandenBerg (1996, solid line) and Bertelli et al. (1994, dashed line).

is not included since one with the correct metallicity could not be found, and comparisons with ones close to the metallicity of NGC 2141 were unsuitable.

NGC 7142

Since this cluster is subject to heavy field star contamination and possibly differential reddening, only the central 3x3 arcmin, corrected for field star contamination via the Bahcall and Soneira (1980) models, was used in the comparison with the isochrones. A colour excess of $E(V-I) = 0.37$ and a distance modulus modulus of $(m-M)_V = 12.96$ were used. A solar metallicity Bertelli et al. (1994) isochrone at 2.5 Gyr provided a very good fit to all the key regions in the CMD (Figure 5.9).

The CMD also was compared to a 2.6 Gyr solar metallicity isochrone by Dowler and VandenBerg (1996), and is shown in Figure 5.10. Note that the isochrone appears to be 0.01 – 0.02 magnitudes too red. Most likely this is due to the colour transformation (those authors used the Bessell and Brett (1988) colours as initial estimates).

NGC 7142's turnoff portion of the CMD was enlarged, and solar metallicity overshooting and canonical isochrones (ages of 2.6 and 2.5 Gyr, respectively) compared with it (Figure 5.11). As was the case with NGC 6819, the overshooting isochrone provides a superior fit through the turnoff.

5.3.3 Comparison of the Two Methods

The Bertelli et al. (1994) isochrones appear to be too red by 0.03 magnitudes. Presumably this is due to uncertainties in the colour transformations. The Dowler and VandenBerg (1996) overshooting isochrones also appear to be too red by 0.01 to 0.02 magnitudes. However, these isochrones are still

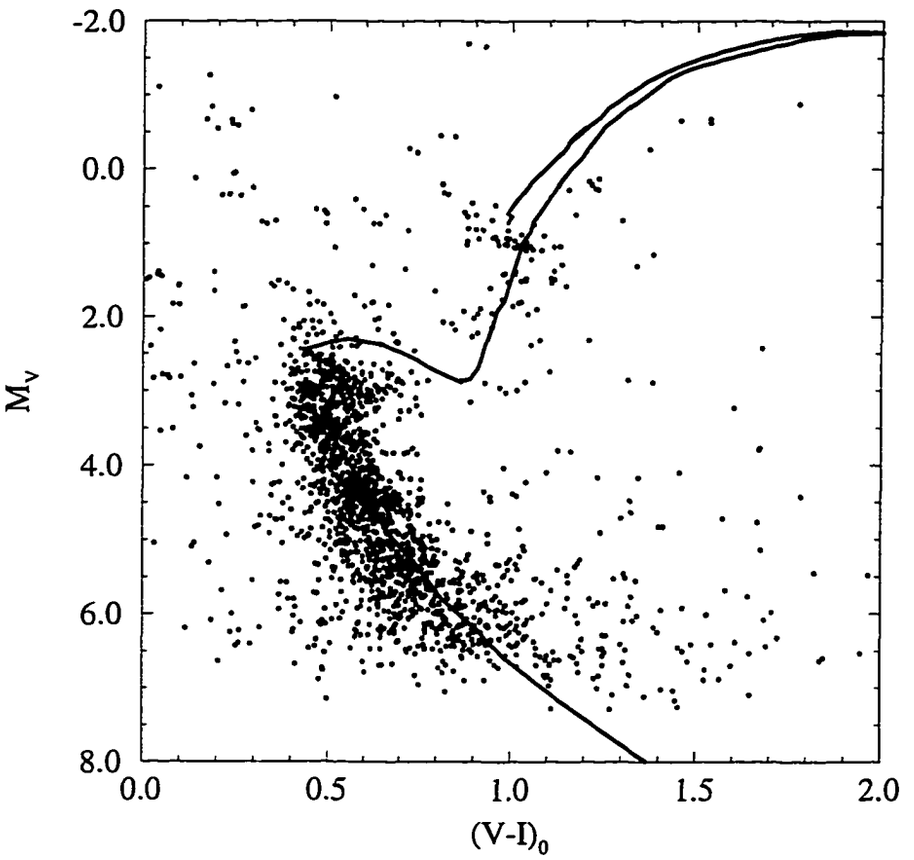

Figure 5.8: An isochrone having an age of 2.5 Gyr and metal abundance of $Z = 0.008$ from Bertelli et al. (1994) is plotted on the CMD of NGC 2141.

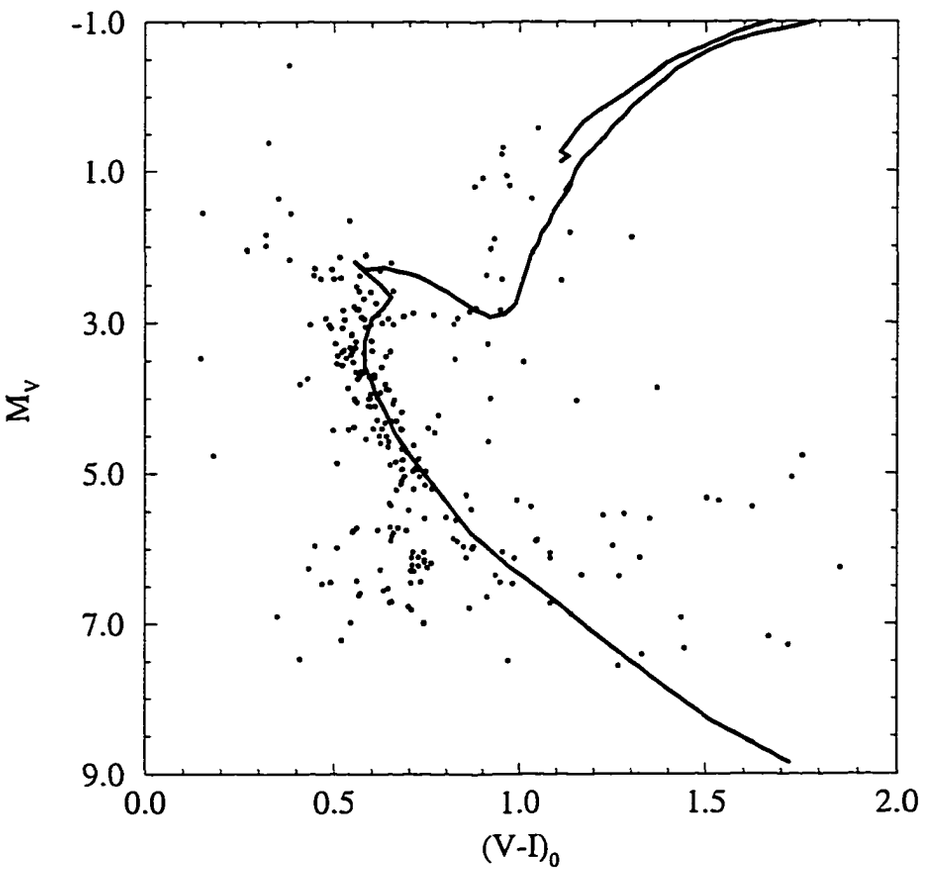

Figure 5.9: A 2.5 Gyr solar metallicity isochrone from Bertelli et al. (1994) is plotted with the field star-subtracted CMD of NGC 7142. The turnoff is fit well in this plot.

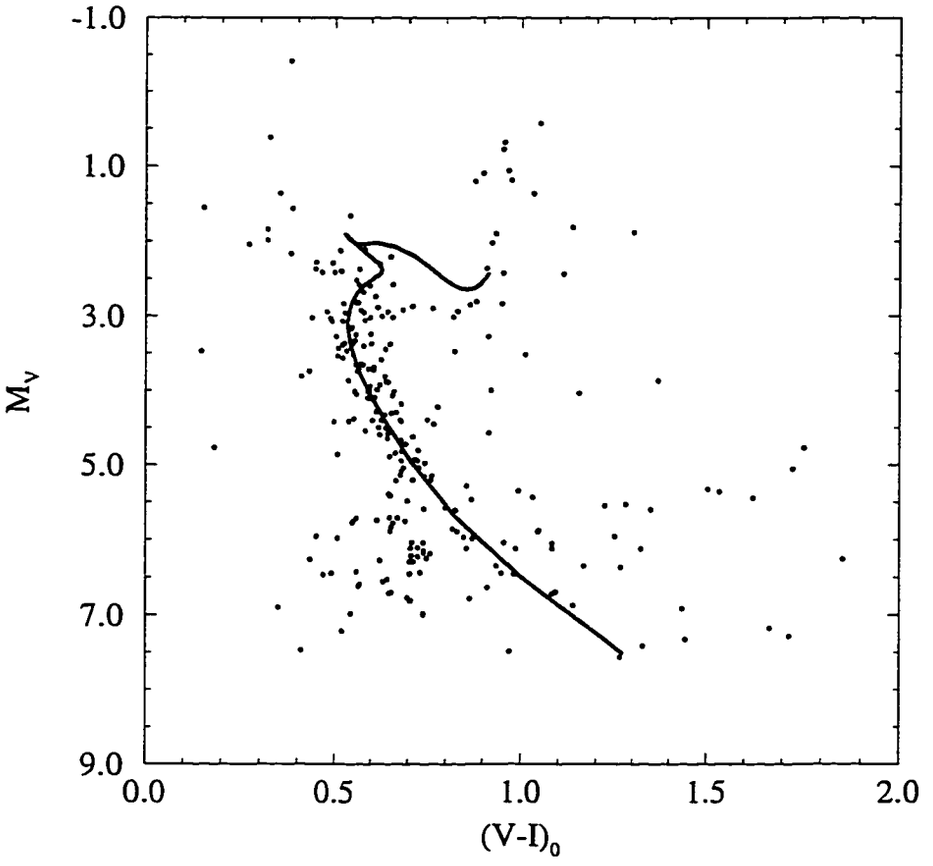

Figure 5.10: A solar metallicity isochrone from Dowler and VandenBerg (1996) having an age of 2.6 Gyr is superposed on the CMD of NGC 7142.

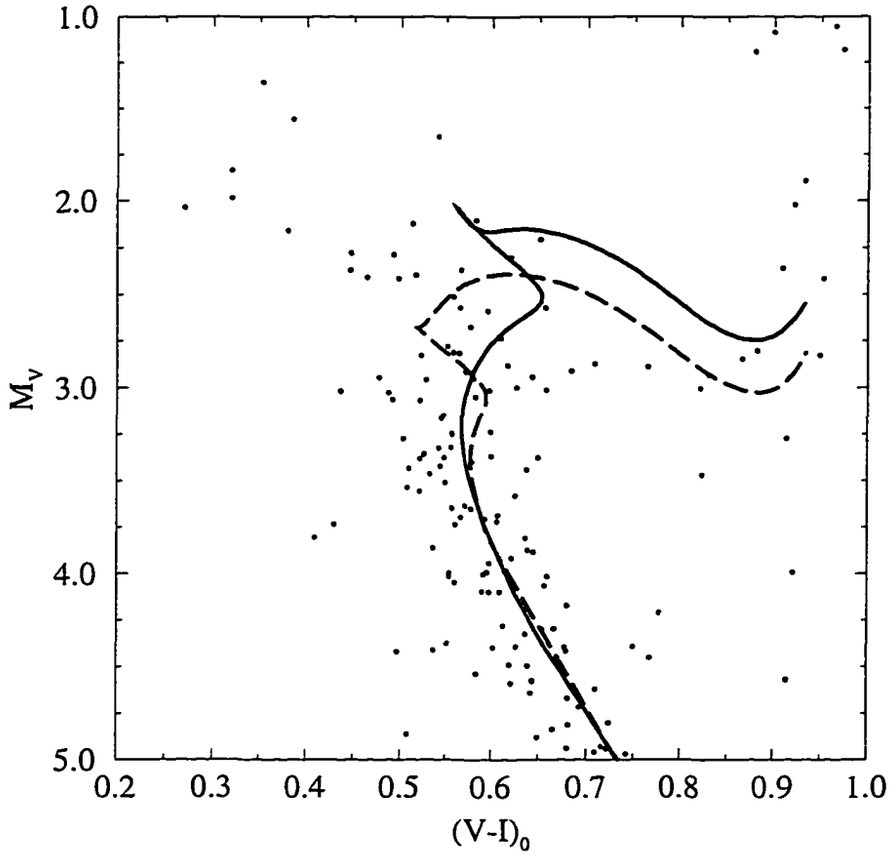

Figure 5.11: Solar metallicity overshooting (solid line) and canonical (dashed line) isochrones [2.6 and 2.5 Gyr, respectively, both from Dowler and VandenBerg (1996)] are superposed on the CMD of NGC 7142. As was the case for NGC 6819, the overshooting isochrone provides a superior match to the CMD.

preliminary, and the colour transformations which were used will be revised in the future (Dowler and VandenBerg, private communication). The Bertelli et al. (1994) isochrones also do not match the location of the clump exactly. They use Sandage's (1993) $M_V - [Fe/H]$ relation ($M_V = 0.30[Fe/H] + 0.94$, from observations of RR Lyrae stars) for the clump, which differs from the one used in this work in both the slope and zeropoint. However, since the uncertainty in the zeropoint is as much as 0.1 magnitudes, there is general agreement between the two relations.

It is apparent from the comparison of the fits provided by the two sets of isochrones that convective overshooting is an important factor to consider in determining ages of intermediate-age open clusters. As there is still controversy regarding the amount of overshooting which is appropriate (see references in Chapter 1), further observations will help to provide constraints.

Recall that the MAR method was used only to rank the clusters in age, not determine absolute ages, and that it indicated that the three younger clusters were similar in age. Both the CMD morphology and the isochrones support this claim. An additional question arises from the fact that given the effects of overshooting are substantial at young and intermediate ages, and become negligible for old clusters, one would suspect that the MAR calibration (which presumably does not include overshooting) will not give accurate differential ages. However, discussion with Dowler (private communication) indicated that even at an age of 7 Gyr (Dowler, 1994), overshooting may be important, and that the age ranking should still be valid even if the ages of the calibration clusters change once overshooting is taken into account.

5.4 Applications of $(V-K)$ Photometry

Cohen et al. (1978) began a program several years ago to establish a library of IR magnitudes for stars in globular and open clusters spanning a wide range in metal abundance. They hoped that these data would be useful in the construction of stellar synthesis models for cluster systems covering a range in total mass and metal abundance. This pioneer paper, and others which followed (Frogel et al. (1983), and references therein), established calibrations of $(V-K)$ colours and effective temperatures which were independent of metal abundance or surface gravity g. Empirical bolometric magnitudes and luminosities were derived as well, which made it possible for them to transform their observations to the theoretical (L_{bol} versus T_{eff}) plane and compare them directly to sets of evolutionary tracks.

Figure 5.12 is adapted from Table 3 of Cohen et al. (1978), and plots $(V-K)_0$ versus T_{eff} for several different values of g and $[Fe/H]$ (upper plot). Cohen et al. (1978) obtained the plot from comparisons between star cluster observations (at optical and near-infrared observations) and model atmospheres. It is clear from this plot that, for the range in temperature given, $(V-K)$ is an excellent indicator of temperature, and the calibration is independent of g and $[Fe/H]$, due to H^- absorption dominating the opacity in both passbands. The reason for this is as follows. An H^- ion is formed when an electron passes sufficiently close to a neutral H atom and is attracted, due to incomplete shielding of the proton charge by the single electron of the atom. The second electron may become attached, but with a low binding energy (0.7 eV). In cool stars, H^- produces most of the continuous absorption via bound-free (energy quanta in the visual and near-infrared regions of the spectrum photodissociate the H^- ion into a neutral H atom

and a free electron) and free-free (interaction of the neutral H atoms with free electrons) transitions. The bound-free absorption has a limiting wavelength of about 1.7 μm, reaches a maximum at about 8000 $\AA$ and then falls off again towards shorter wavelengths, while the free-free absorption minimum occurs at about 1.6 μm and rises towards longer wavelengths.

Contrast the figure described above with the lower plot of Figure 5.12, which shows a substantial dependence on g and $[Fe/H]$. The derived typical uncertainty in $(V-K)$ of 0.05 mag yields an uncertainty in T_{eff} of only $\pm$70 K. $(J-K)$ is a good temperature indicator as well, although this colour spans only 0.6 mag over the same temperature range, and the uncertaintites in temperature due to a slight dependence on g and $[Fe/H]$ increase to $\pm$100 K (Cohen et al., 1978). The advantages of using $(J-K)$ are that this colour is less affected by reddening, and both magnitudes may be measured on the same night using the same equipment, ensuring good observational accuracy.

The calibration between the bolometric correction and effective temperature produced by Cohen et al. (1978) is shown in Figure 5.13, which displays a slight dependence on gravity and metal abundance. Because of this, an error of $\pm$200 K in the effective temperature yields an uncertainty of $\pm$0.1 mag in the bolometric correction.

Ridgway et al. (1980) established a new $T_{eff}, (V-K)$ relation based on lunar occultations of field giants of spectral type ranging from K0 to M6. All these stars have solar or near-solar metal abundance. Since effective temperature is fixed by the star's luminosity and radius, a direct determination can be made only when the angular size of the stellar disk is known. Nearly 100 stars having radii determined by lunar occultations were used in this study. Ridgway made use of these data, and obtained V and K photometry for each star. Observations at other passbands were obtained from the liter-

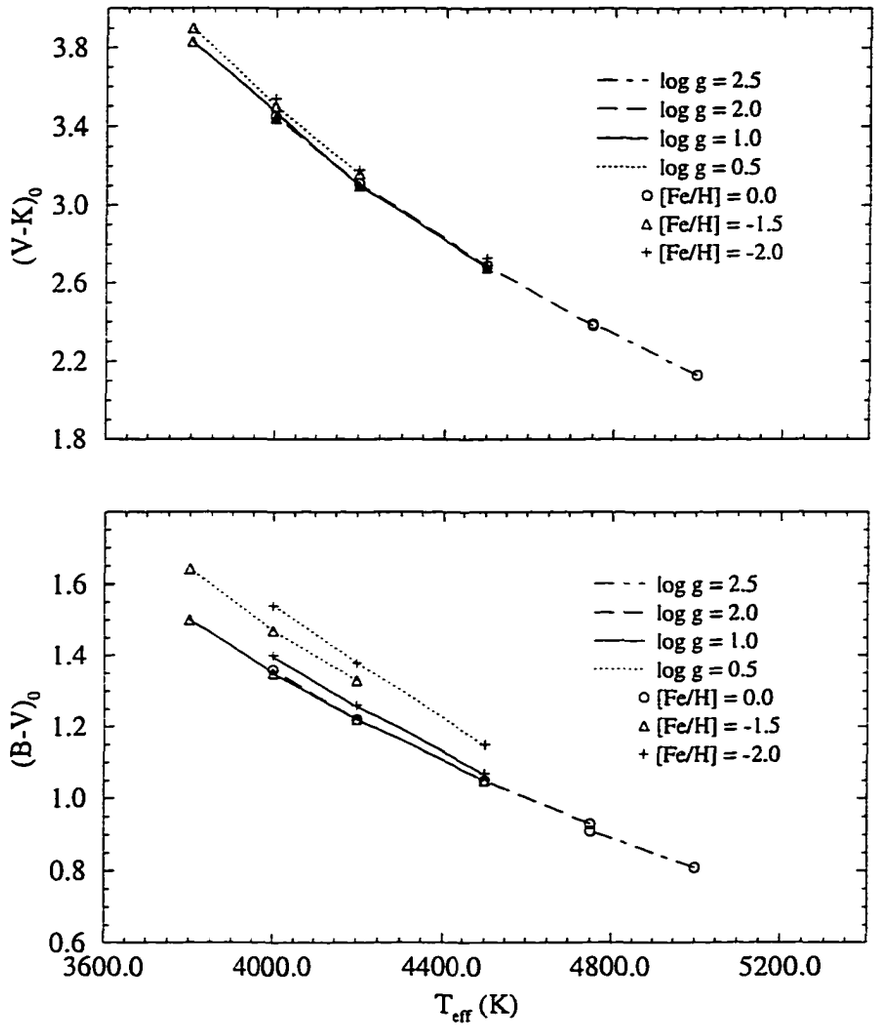

Figure 5.12: Both figures plot colour (corrected for reddening) versus effective temperature (in Kelvin). The upper plot illustrates the effectiveness of using $(V-K)$ as a temperature indicator, independent of gravity and metal abundance, for the temperature range given. The lower plot shows the dependence on gravity and metallicity for $(B-V)$. Both plots are adapted from Cohen et al. (1978).

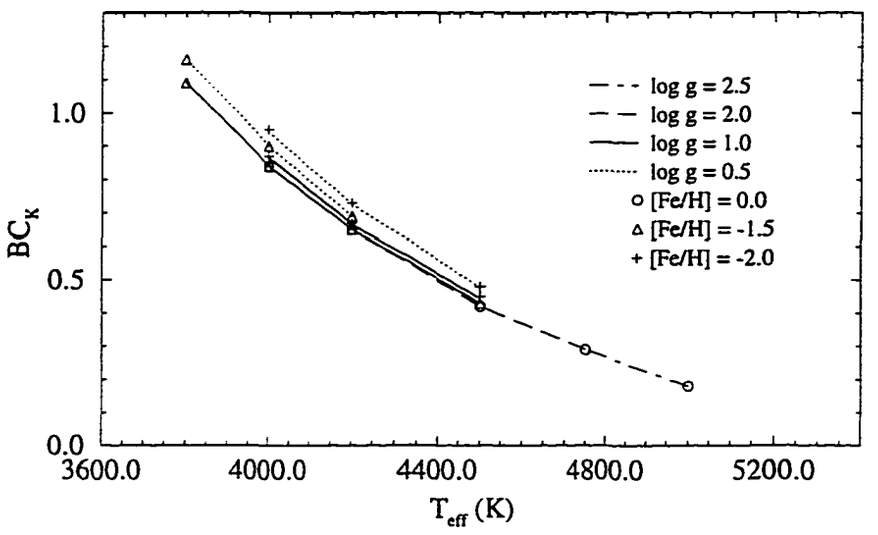

Figure 5.13: Bolometric correction (K) versus effective temperature. There is a slight dependence on gravity and metallicity in this relation. From Frogel et al. (1981).

ature, and used to create spectral energy distributions which were integrated numerically to obtain bolometric fluxes. Figure 5.14 compares the resulting $T_{eff}, (V-K)$ relation with one from Cohen et al. (1978). The agreement between the two is good, and the discrepancy is less than the uncertainty in Ridgway et al.'s (1980) data (for a given colour, $\Delta T_{eff} \sim 50 - 100$ K).

Houdashelt et al. (1992) have conducted the only open cluster survey in the manner of Cohen et al. (1978). They obtained IR data for eight old open clusters, and obtained effective temperatures and bolometric luminosities for the cluster giants. It is intended that the results presented below for the clusters studied here will complement this survey.

5.4.1 Effective Temperatures and Bolometric Corrections

Effective temperatures were determined for the giants and clump stars. In all cases, only those stars deemed to be members on the basis of location in the CMD, metallicities, radial velocities or proper motion surveys were used. Ridgway's (1980) scale was used in all cases.

The $(V-K)$ colours from Tables 4.3 to 4.6 first were corrected for reddening using the colour excesses given in Chapter 4 transformed via

$$E(V-K) = 2.744E(B-V) \tag{5.3}$$

(Rieke and Lebofsky, 1985). The effective temperatures were derived by simply reading them off an expanded version of Figure 5.14. Typical uncertainties in $(V-K)_0$ resulting from photometric and reddening uncertainties range from 0.05 to 0.15 mag, resulting in a maximum error in the temperature of ~ 200 K.

Frogel et al. (1981) observed several giants in the clusters M3, M13, M67, M71, M92 and 47 Tuc (all but M67 are globular clusters). They obtained

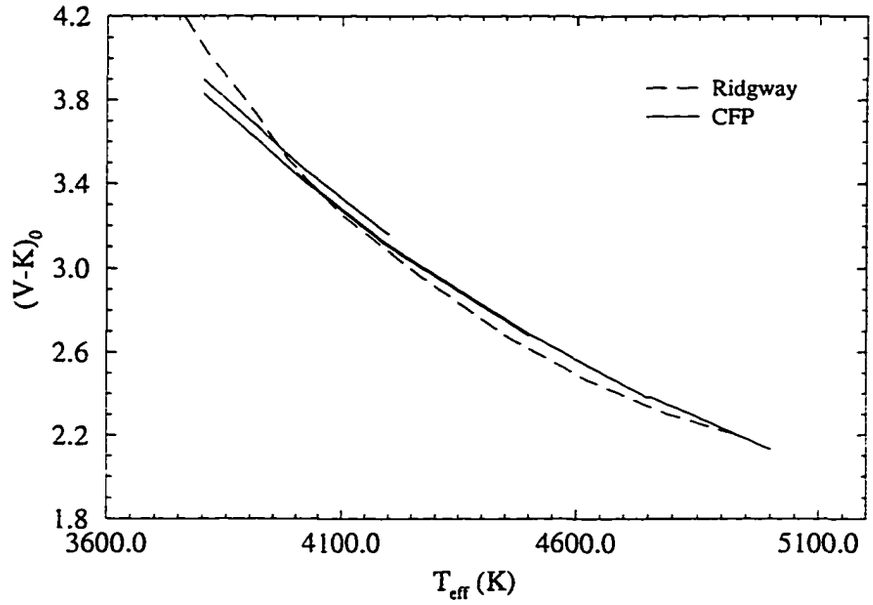

Figure 5.14: Plot comparing Ridgway et al.'s (1980) relation with some from Cohen et al. (1978). Except for some deviation at the cool end, the agreement between the models is good. Adapted from Frogel et al. (1981).

bolometric corrections by integrating the spectral energy distribution as described above and calibrating the energy distribution using information by Johnson (1966) for $UBVRI$ and Wilson et al. (1972) for JHK. They assumed a bolometric correction for the Sun to establish a scale. The results were used to construct a calibration of $(V-K)_0$ versus BC_K.

It is appropriate to derive bolometric corrections to the K magnitude since the stars in question are cool giants which have the peak in their spectral energy distribution near the K filter. Thus, the following relations are obtained:

$$m_{bol} = V + BC_V = K + BC_K \tag{5.4}$$

and

$$BC_K = BC_V + (V-K)_0. \tag{5.5}$$

The present data consist of observations for V and I (and B for NGC 6819), and JHK. Literature searches yielded additional data in U and B for some of the other clusters, but failed to provide observations in the R or L filters. These gaps in the energy distribution, as well as only fair quality data in the others, warranted abandoning the derivation of bolometric corrections from first principles, since a fair amount of extrapolation would have been required. Instead, the scale determined by Frogel et al. (1981), and illustrated in Figure 5.13, was used with the $(V-K)_0$ colours to obtain BC_K. Tables 5.2 to 5.5 list suspected member giants for each cluster, their $(V-K)$ and $(V-K)_0$ colours, the effective temperatures in Kelvin, and the bolometric corrections BC_K.

In preparation for the calculation of bolometric magnitudes and luminosities, the K magnitudes were corrected for absorption using

$$A_K = 0.112 A_V \tag{5.6}$$

Table 5.2: Effective temperatures and bolometric corrections for NGC 6791. ID numbers are those adopted by Garnavich et al. (1994). Adopting $E(B-V) = 0.23$ gives $E(V-K) = 0.63$. Blanks indicate the star was too red for the bolometric correction scale.

ID	$(V-K)$	$(V-K)_0$	T_{eff}	BC_K
1	7.28	6.65	3285	—
2	4.40	3.77	3895	2.58
3	4.28	3.65	3940	2.54
4	6.18	5.55	3485	—
7	6.14	5.51	3490	—
8	3.54	2.91	4305	2.26
9	3.94	3.31	4075	2.42
10	3.49	2.86	4335	2.23
11	2.99	2.36	4730	1.99
12	4.34	3.71	3915	2.56
14	4.77	4.14	3775	2.67
16	3.94	3.31	4075	2.42
17	3.48	2.85	4340	2.23
19	4.03	3.40	4035	2.45
22	3.16	2.53	4570	2.07

Table 5.3: Effective temperatures and bolometric corrections for NGC 2141. ID numbers are those adopted by Burkhead et al. (1972). Adopting $E(B-V) = 0.32$ gives $E(V-K) = 0.88$. Blanks indicate the star was either too blue or too red for the bolometric correction or temperature scale. The temperatures have been rounded to the nearest five degrees Kelvin.

ID	$(V-K)$	$(V-K)_0$	T_{eff}	BC_K
3-2-18	4.72	3.84	3870	2.59
4-32	3.85	2.97	4265	2.28
4-25	3.84	2.96	4265	2.28
4-26	2.85	1.97	—	1.77
4-21	4.21	3.33	4060	2.42
2-2-10	3.71	2.83	4350	2.22
4-28	3.30	2.42	4660	2.03
4-27	3.28	2.40	4685	2.02
2-3-13	3.66	2.78	4385	2.19
2-3-29	3.49	2.61	4495	2.11
2-3-33	3.66	2.78	4385	2.19
2-2-18	2.00	1.12	—	—
3-2-20	6.72	5.84	3435	—
4-23	3.25	2.37	4720	2.00
3-2-40	4.48	3.60	3950	2.53
4-19	4.12	3.24	4105	2.38
3-2-52	3.65	2.77	4395	2.19
3-2-53	3.53	2.65	4475	2.14
3-2-45	3.48	2.60	4505	2.11
4-24	3.20	2.32	4765	1.98
5-31	3.32	2.44	4650	2.03
5-30	3.13	2.25	4850	1.95
5-34	2.90	2.02	—	1.80
50060	3.35	2.47	4615	2.05
1-3-7	4.45	3.57	3965	2.51
1-3-21	3.82	2.94	4280	2.27
1-4-5	4.01	3.13	4170	2.35
2-3-42	1.25	0.37	—	—
3-2-34	3.42	2.54	4560	2.08
2-2-62	3.58	2.70	4435	2.15

Table 5.4: Effective temperatures and bolometric corrections for NGC 6819. ID numbers are those adopted by Sanders (1972). All stars have proper motion probabilities greater than 80%. Adopting $E(B-V) = 0.11$ gives $E(V-K) = 0.30$. The blank indicates the star was too blue for the temperature scale. Temperatures have been rounded to the nearest five degrees Kelvin.

ID	$(V-K)$	$(V-K)_0$	T_{eff}	BC_K
147	3.10	2.80	4370	2.21
74	2.91	2.61	4495	2.12
77	2.90	2.60	4505	2.12
94	3.90	3.60	3950	2.52
89	2.88	2.58	4520	2.10
85	2.81	2.51	4590	2.07
150	2.94	2.64	4475	2.13
148	2.94	2.64	4475	2.13
130	3.11	2.81	4360	2.21
131	2.84	2.54	4560	2.08
126	3.12	2.82	4360	2.21
118	2.91	2.61	4495	2.12
124	3.14	2.84	4345	2.22
116	2.85	2.55	4550	2.08
96	2.94	2.64	4475	2.13
87	2.85	2.55	4550	2.08
86	2.71	2.41	4680	2.03
106	2.52	2.22	4925	1.94
110	4.08	3.78	3895	2.58
97	2.69	2.39	4705	2.01
108	5.93	5.63	3475	—
78	2.68	2.38	4710	2.01
98	2.88	2.58	4520	2.10
114	2.62	2.32	4765	1.98
111	2.72	2.42	4660	2.03
93	3.72	3.42	4020	2.45
141	3.33	3.03	4230	2.30
79	3.22	2.92	4300	2.24
119	3.01	2.71	4430	2.16
83	4.79	4.49	3680	2.75

Table 5.5: Effective temperatures and bolometric corrections for NGC 7142. ID numbers are those adopted by van den Bergh and Sher (1960). Adopting $E(B-V) = 0.29$ gives $E(V-K) = 0.80$. Blanks indicate the star was too blue for the temperature scale. Temperatures have been rounded to the nearest five degrees Kelvin.

ID	$(V-K)$	$(V-K)_0$	T_{eff}	BC_K
52	4.39	3.59	3955	2.52
91	3.25	2.45	4640	2.04
98	3.53	2.73	4415	2.17
120	2.86	2.06	—	1.82
D	3.37	2.57	4540	2.09
E	4.17	3.37	4050	2.44
G	3.81	3.01	4240	2.30
O	3.45	2.65	4475	2.13
P	2.89	2.09	—	1.84

(Rieke and Lebofsky, 1985), where $A_V = 3.09E(B-V)$. Apparent bolometric magnitudes were obtained from

$$m_{bol} = K_0 + BC_K, \tag{5.7}$$

and absolute bolometric magnitudes from

$$M_{bol} = m_{bol} - (m-M)_0 \tag{5.8}$$

using distances derived in this work. Finally, bolometric luminosities, in units of solar luminosity, were derived using

$$log(\frac{L_{bol}}{L_{\odot bol}}) = 0.4(M_{\odot bol} - M_{bol}), \tag{5.9}$$

where $M_{\odot bol} = 4.75$ (Allen, 1973). Tables 5.6 to 5.9 list these quantities for each cluster.

The effective temperatures and bolometric magnitudes may be used to construct HR diagrams. Figure 5.15 displays the HR diagram of the giants

Table 5.6: Absolute bolometric magnitudes and luminosities for NGC 6791. ID numbers are those adopted by Garnavich et al. (1994). Adopting $E(B-V) = 0.23$ gives $A_K = 0.08$.

ID	K	K_0	M_{bol}	$\log(\frac{L_{bol}}{L_{\odot bol}})$
2	9.32	9.24	−0.99	2.30
3	9.78	9.70	−0.57	2.13
8	10.26	10.18	−0.37	2.05
9	10.19	10.11	−0.28	2.01
10	11.03	10.95	0.37	1.75
11	11.60	11.52	0.60	1.62
12	9.50	9.42	−0.83	2.23
14	8.84	8.76	−1.38	2.45
16	9.79	9.71	−0.68	2.17
17	11.07	10.99	0.41	1.74
19	10.14	10.06	−0.30	2.02
22	11.34	11.26	0.52	1.69

for each cluster. The HR diagrams are compared to the giant branch loci of two open clusters (M67 and NGC 2204, from Houdashelt et al. 1992) and two globular clusters (M92 and 47 Tuc, from Frogel et al. 1981). In this figure, the cluster mean loci are located on the HR diagram according to both age and metallicity. For example, the more metal-rich globular cluster (47 Tuc) lies to the right of M92 [$[Fe/H] \sim -2.0$ from Stetson and Harris (1988)]. Even though the open cluster NGC 2204 is more metal-rich than 47 Tuc (a literature average derived by Houdashelt et al. (1994) gives $[Fe/H] \sim -0.4$), its younger age places it between the two globular clusters. The data in this study form loci which agree with those defined by the clusters of near solar (M67) and metal-poor [47 Tuc, with $[Fe/H] \sim -0.8$ from Hesser and Bolte (1992)] metallicities. It is interesting to note that NGC 6791's giant branch lies so far to the right of M67's, even though it is older. Again, the infrared photometry obtained for NGC 6791 is very valuable, since it is the most

Table 5.7: Absolute bolometric magnitudes and luminosities for NGC 2141. ID numbers are those adopted by Burkhead et al. (1972). Adopting $E(B-V) = 0.32$ gives $A_K = 0.11$.

ID	K	K_0	M_{bol}	$\log(\frac{L_{bol}}{L_{\odot bol}})$
3-2-18	8.33	8.22	−2.13	2.75
4-32	10.20	10.09	−0.57	2.13
4-25	10.29	10.18	−0.48	2.09
4-26	10.80	10.69	−0.48	2.09
4-21	10.86	10.74	0.22	1.81
2-2-10	11.27	11.16	0.44	1.72
4-28	11.40	11.29	0.38	1.75
4-27	11.22	11.11	0.19	1.82
2-3-13	11.30	11.19	0.44	1.72
2-3-29	11.42	11.31	0.48	1.71
2-3-33	11.79	11.68	0.93	1.53
4-23	8.98	8.87	−2.07	2.73
3-2-40	8.77	8.66	−1.75	2.60
4-19	9.54	9.43	−1.13	2.35
3-2-52	10.88	10.77	0.02	1.89
3-2-53	11.37	11.26	0.46	1.72
3-2-45	11.61	11.50	0.67	1.63
4-24	11.65	11.54	0.58	1.67
5-31	10.56	10.45	−0.46	2.08
5-30	10.50	10.39	−0.50	2.14
5-34	10.88	10.77	−0.37	2.05
50060	11.45	11.34	0.45	1.72
1-3-7	8.85	8.74	−1.69	2.58
1-3-21	10.37	10.26	−0.41	2.06
1-4-5	10.60	10.49	−0.10	1.94
3-2-34	11.58	11.47	0.61	1.66
2-2-62	11.36	11.25	0.46	1.72

Table 5.8: Absolute bolometric magnitudes and luminosities for NGC 6819. ID numbers are those adopted by Sanders (1972). All stars have proper motion probabilities greater than 80%. Adopting $E(B-V) = 0.11$ gives $A_K = 0.04$.

ID	K	K_0	M_{bol}	$\log(\frac{L_{bol}}{L_{\odot bol}})$
147	10.11	10.07	0.52	1.69
74	10.21	10.17	0.53	1.69
77	11.33	11.29	1.65	1.24
94	8.07	8.03	−1.21	2.38
89	10.19	10.15	0.49	1.70
85	10.31	10.27	0.58	1.67
150	10.17	10.13	0.50	1.70
148	10.13	10.09	0.46	1.72
130	10.06	10.02	0.47	1.71
131	10.18	10.14	0.46	1.72
126	9.64	9.60	0.05	1.88
118	10.10	10.06	0.42	1.73
124	9.69	9.65	0.11	1.86
116	10.79	10.75	1.07	1.47
96	10.18	10.14	0.51	1.70
87	10.43	10.39	0.71	1.62
86	11.19	11.15	1.42	1.37
106	10.43	10.39	0.57	1.67
110	7.76	7.72	−1.46	2.48
97	10.18	10.14	0.39	1.74
78	8.96	8.94	−0.81	2.22
98	10.37	10.92	1.26	1.40
114	11.48	11.44	1.66	1.24
111	10.11	10.07	0.34	1.76
93	8.13	8.09	−1.22	2.39
141	8.91	8.77	−0.69	2.18
79	8.44	8.40	−1.12	2.35
119	10.12	10.08	0.48	1.71
83	6.78	6.74	−2.27	2.81

Table 5.9: Absolute bolometric magnitudes and luminosities for NGC 7142. ID numbers are those adopted by van den Bergh and Sher (1960). Adopting $E(B-V) = 0.29$ gives $A_K = 0.10$.

ID	K	K_0	M_{bol}	$\log(\frac{L_{bol}}{L_{\odot bol}})$
52	7.61	7.51	−2.03	2.71
91	10.89	10.79	0.77	1.59
98	9.86	9.76	−0.13	1.95
120	11.05	10.95	0.71	1.62
D	9.26	9.16	−0.81	2.22
E	8.54	8.44	−1.18	2.37
G	9.22	9.12	−0.64	2.16
O	10.19	10.09	0.16	1.84
P	11.13	11.03	0.81	1.58

metal-rich cluster observed to date.

Figure 5.16 compares the cluster HR diagrams with theoretical ones from Bertelli et al. (1994) showing the location of the giant and asymptotic giant branches and red giant clump. Solar metallicity tracks are used for NGC 6819, NGC 7142 and NGC 6791, while a metal-poor one ($Z = 0.008$) is compared with NGC 2141. In general, the location of the cluster giant branches agree with the theoretical ones (except for NGC 2141). Those data which lie redward of the giant branches may indicate that the models are too hot (assuming the bolometric magnitudes of the cluster giants are correct).

5.5 Galactic Evolution

This work would not be complete without a brief discussion on the relevance of the results to our understanding of galactic evolution. Several authors have examined the relationship between various parameters such as age, metal abundance, height above the plane and distance from the galactic centre. A few of the more important relations will be discussed here, beginning with

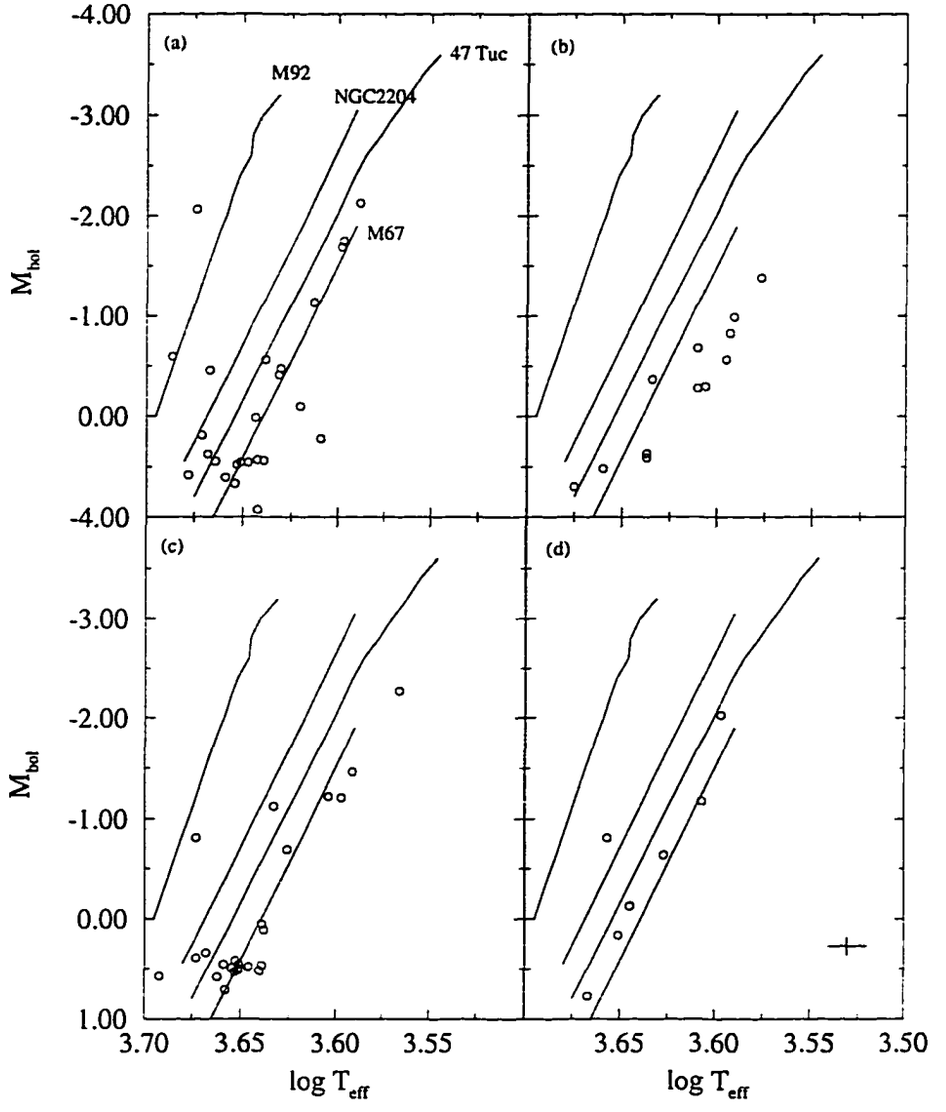

Figure 5.15: HR diagrams of (a) NGC 2141, (b) NGC 6791, (c) NGC 6819 and (d) NGC 7142. Included are the giant branches of M67, NGC 2204, M92 and 47 Tuc from Houdashelt et al. (1992) and Frogel et al. (1981). A typical error bar is shown in the corner of the lower right plot.

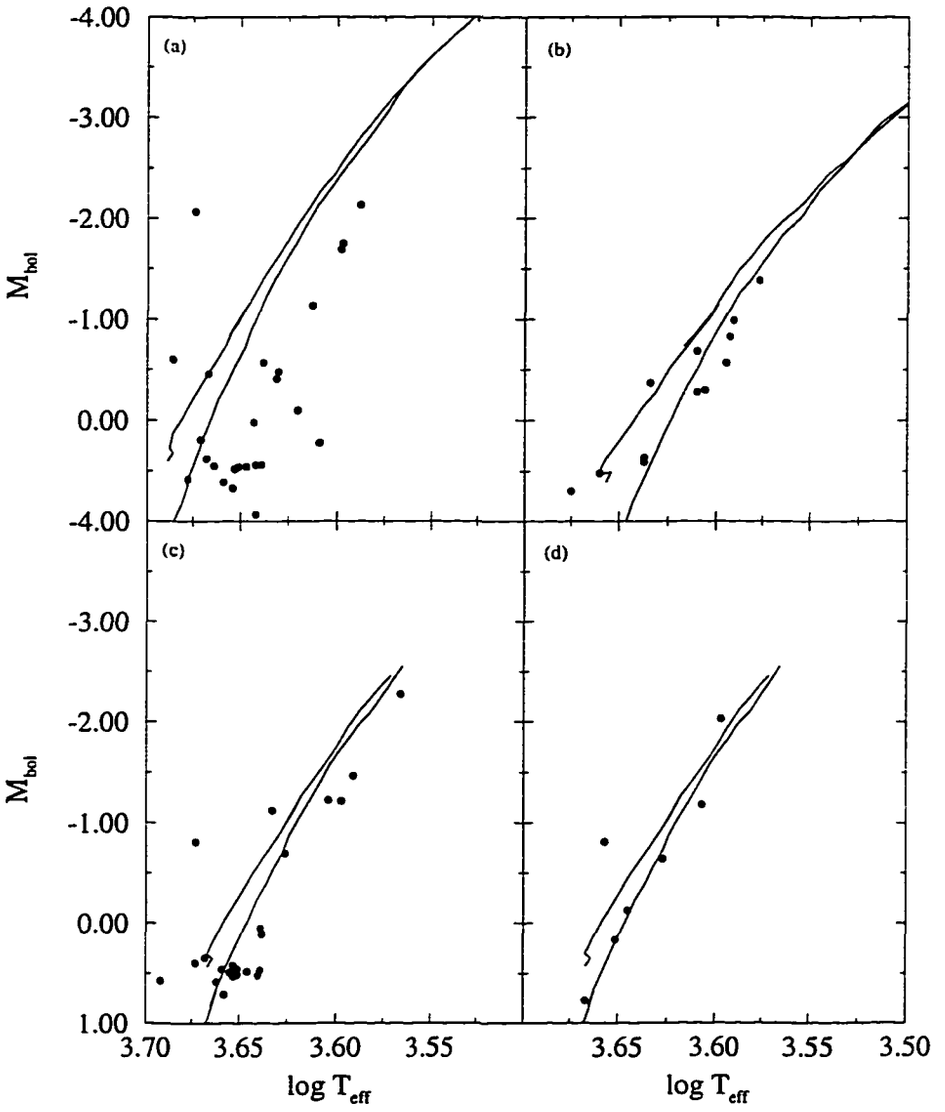

Figure 5.16: HR diagrams of (a) NGC 2141, (b) NGC 6791, (c) NGC 6819 and (d) NGC 7142. Superposed are theoretical HR diagrams from Bertelli et al. (1994) for $Z = 0.008$, 0.02, 0.02 and 0.02, respectively.

the age-metallicity relation.

Friel and Janes (1993) found a well-defined radial abundance gradient for a sample of 33 old open clusters located in the galactic disk. Figure 5.17 displays their data. The four clusters studied in this work (and in Friel and Janes' (1993) paper) are represented by open circles, and are important to the plot since three of them have low values of R_{gc} and serve to populate the upper left corner of the plot. Note that the values for the galactocentric radius R_{gc}, taken from Table 1.1, have been derived from the distances determined in Chapter 4. Figure 5.17 indicates a gradient of ~ -0.09 dex kpc^{-1} in good agreement with other survey results [-0.08 dex kpc^{-1} from Janes (1979), -0.11 dex kpc^{-1} from Cameron (1985) and -0.09 dex kpc^{-1} from Panagia and Tosi (1981)]. Janes et al. (1988) used all the clusters in the Lyngå (1987) catalogue which had metallicity determinations and derived a global gradient of -0.11 dex kpc^{-1}, but found that subsets of younger (age < 0.2 Gyr) and older (age > 0.2 Gyr) clusters defined gradients of -0.07 and -0.14 dex kpc^{-1}, respectively. This discrepancy was due to the fact that a few clusters (Berkeley 19, NGC 2141, 2158, 2204, 2243 and 2506) had metallicities around -0.6 dex. The revision of these metal abundances yielded comparable gradients for the two subsets.

Friel and Janes (1993) also mention that their value for the abundance gradient agrees with that as predicted by Matteucci and François (1989) for their models of galactic chemical evolution, who find abundance gradients ranging from -0.05 to -0.09 dex kpc^{-1} for a variety of model parameters.

Houdashelt et al. (1992) used their sample of eight open clusters to examine the relationship between cluster age (as determined from canonical isochrones) and metallicity. They found a correlation of $[Fe/H] \propto -0.135\tau$, where τ is the age in Gyr, which agreed roughly with that found for clusters

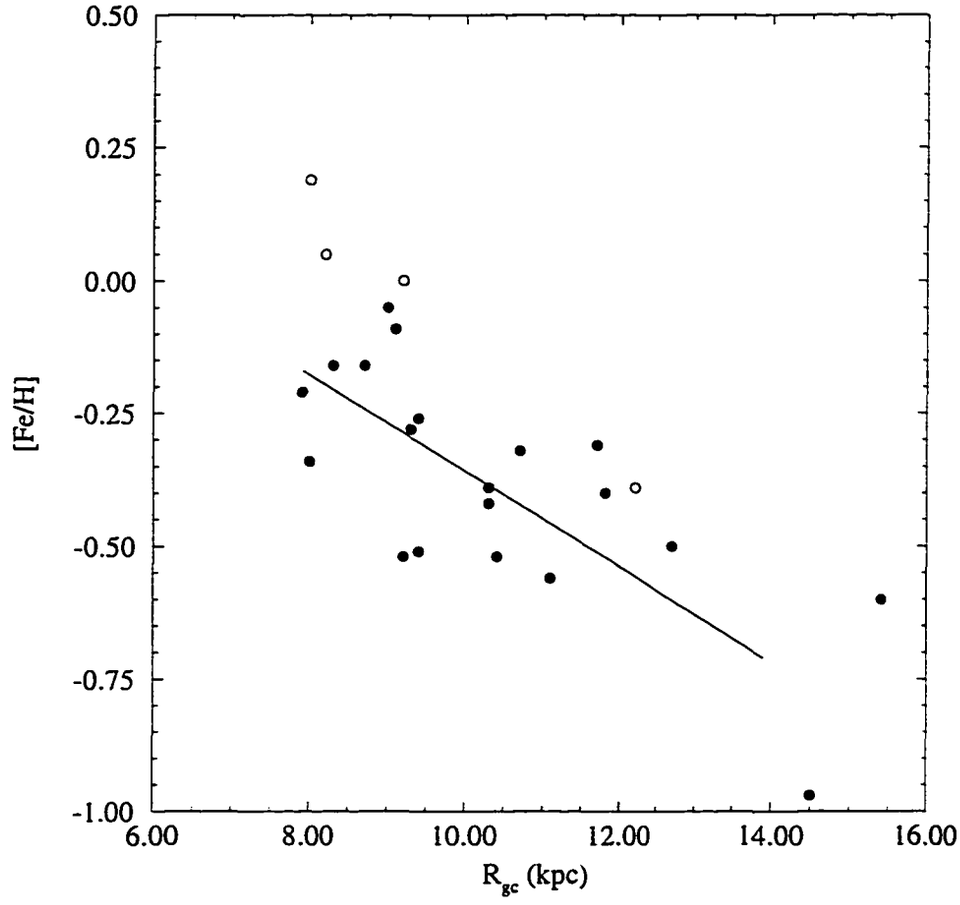

Figure 5.17: Disk radial abundance gradient from Friel and Janes (1993). The four clusters studied in the present work are indicated by open circles. Note that the new values of the galactocentric radius do not alter the conclusions made by the above authors.

in the Large Magellanic Cloud (Cohen, 1982; Mateo, 1988), but was lower than that found in the solar neighbourhood [Twarog (1980) found a value of $[Fe/H] \propto -0.04\tau$ from Strömgren and Hβ photometry of F dwarfs, while Carlberg et al. (1985) obtained $[Fe/H] \propto -0.02\tau$ from a subset of Twarog's (1980) data.] Adjusting their metallicity values to those appropriate for the solar galactocentric radius ($R_\circ$), they found a shallower value for the slope (-0.09). Figure 5.18 displays their data (filled circles); the age-metallicity relation is indicated by a dashed line. For comparison purposes, the four clusters studied in the present work are included as open circles.

Caution must be exercised, however, whenever attempts at drawing conclusions from a small sample are made. Indeed, Friel and Janes (1993) constructed age-metallicity relationships for their sample of clusters, and found that no correlation existed, regardless of whether the observed metal abundances, or those corrected to $R_\circ$, were adopted. Figure 5.18 also contains a selection of Friel and Janes' (1993) data (indicated by plus signs). If all the data are examined together, the lack of an age-metallicity correlation is obvious.

Since Friel and Janes (1993) plotted their data in a manner so as to separate the clusters in the outer and inner disk (*i.e.* inside or beyond $R_\circ$), they did find that the clusters in the outer disk tended to have lower metallicities than those in the inner disk. The important conclusion is that the place of formation in the galaxy, and not age, dictates the metallicity of the cluster.

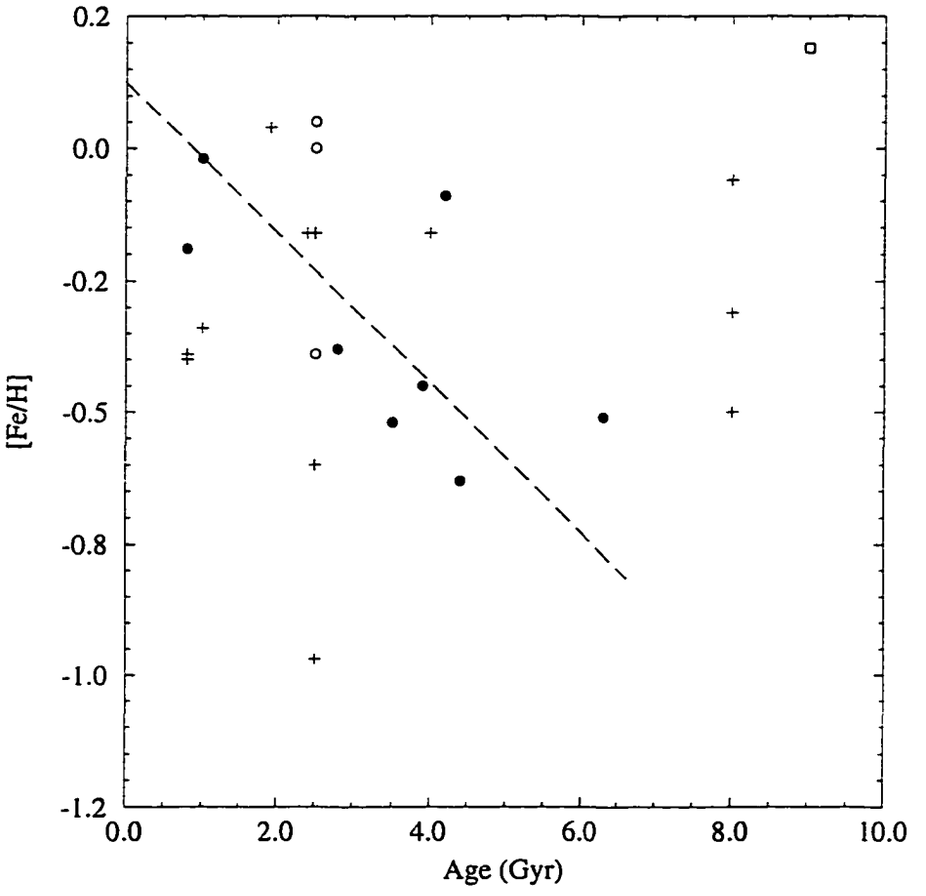

Figure 5.18: The age-metallicity relation from Houdashelt et al. (1992) is defined by their data (filled circles) and indicated by the dashed line. The four clusters studied in the present work are denoted by open circles. Plus signs represent clusters observed by Friel and Janes (1993) and show that no correlation exists when the entire sample is taken into account.

Chapter 6

Summary and Future Work

This dissertation has presented the first VI and near-infrared data for the four galactic clusters NGC 2141, NGC 6819, NGC 7142 and NGC 6791, and in the case of NGC 2141, the first CCD observations. The photometric data were used to produce optical and infrared colour-magnitude diagrams (CMDs). The CMDs of NGC 2141, NGC 6819 and NGC 6791 exhibited red giant clumps and clearly defined (although at times sparsely populated) red giant branches. The exception is NGC 7142, which showed a paucity of clump stars. The main sequences for all the cluster CMDs except NGC 6819 were rather wide, indicating substantial field star contamination, differential reddening and somewhat poor quality data reflecting the observing conditions and an instrument problem for NGC 2141. The presence of many field stars and differential reddening is not surprising considering the proximity of these clusters to the galactic plane.

6.1 The Results

The field star contamination was substantial for NGC 2141 and NGC 7142, and attempts to correct for it for all the clusters were made via two different methods. A field star model by Bahcall and Soneira (1980) estimated the

number of field stars. The two clusters mentioned above also had observations of blank sky which were made in their vicinity, and so field stars from these frames could be used to estimate the level of contamination. In these cases, the actual stellar data provided the best representation of field stars, which is not surprising since the model is valid only for galactic latitudes greater than 10°.

NGC 2141 and NGC 7142 exhibit signs of differential reddening, and various tests were performed to quantify the amount. For NGC 2141, it was found that the reddening varied by $\sim$ 0.07 mag, while for NGC 7142 it was so little (0.02 mag) that the scatter caused by observational errors overshadowed the effect.

In preparation for estimating the ages of the clusters via comparison with theoretical isochrones, colour excesses $E(B-V)$ and apparent distance moduli $(m-M)_V$ were redetermined for all four clusters. In general, the values obtained here agreed with those published previously. The distance moduli were obtained by comparison of the mean magnitude of the clusters' red giant clump with that of M67. Reasonable values were determined, although in the case of NGC 7142 the scatter in the main sequence and lack of a recognisable clump made it difficult to ascertain an accurate distance.

Three of the clusters were ranked in age via the MAR method, which is based on CMD morphology, and confirmed that they all have an age of about 3 Gyr (the MAR method was not applied to NGC 6791, since it was believed to be older than the oldest cluster used in the method calibration, and was more metal-rich than the clusters used).

The cluster CMDs were compared to theoretical isochrones to ascertain ages, and shed light on the controversy regarding the applicability of canonical and overshooting isochrones. Comparison with both sets of isochrones supported the growing body of evidence that models which treat convective

overshooting in the stellar core best represent real stars. NGC 6819, NGC 7142 and NGC 2141 all have ages of 2.5 Gyr, while NGC 6791 has an age of 10 Gyr according to a recent study by Tripicco et al. (1995).

Finally, VK photometry was used to obtain various stellar parameters such as effective temperature, bolometric corrections and luminosities for the cluster giants. HR diagrams (M_V, T_{eff}) were constructed and compared with those of other clusters in the literature, as well as HR diagrams from stellar models. The former indicated good agreement, while the latter showed that the model temperatures may be too high.

6.2 Final Comments

This work has broadened the infrared photometry database of open clusters, thus providing theorists with more observations to use as constraints for stellar models and colour transformations. The support for convective overshooting in the cores of intermediate mass (and age) stars is extremely important in ascertaining which kinds of stellar models are most appropriate, and it is reassuring to see that two different sets of overshooting models predicted the same ages for the cluster studied here, indicating that the parameters involved in constructing the models are becoming more constrained.

So far, rigorous tests of canonical/overshooting models have focused on open clusters younger than 3 Gyr. In order to define more clearly the role convective overshooting has for stars older (and more massive) than this, more observations of clusters up to ages of 7 Gyr (the age at which convective overshooting is still believed to be important) should be made.

Bibliography

Allen, C.: 1973, *Astrophysical Quantities, 3rd. Edition*, p. 162, The Athlone Press, London

Anders, E. and Grevesse, N.: 1989, *Geochim. Cosmochim. Acta* **53**, 197

Anthony-Twarog, B., Heim, E., Twarog, B., and Caldwell, N.: 1991, *Astron. J.* **102**, 1056

Anthony-Twarog, B. and Twarog, B.: 1985, *Astrophys. J.* **291**, 595

Auner, G.: 1974, *Astron. & Astrophys. Supp.* **13**, 143

Bahcall, J. and Soneira, R.: 1980, *Astrophys. J. Supp.* **44**, 73

Bahcall, J. and Soneira, R.: 1981, *Astrophys. J.* **246**, 122

Bahcall, J. and Soneira, R.: 1982, *Astrophys. J.* **255**, 181

Bahcall, J. and Soneira, R.: 1983, *Astrophys. J.* **272**, 627

Becker, S. and Mathews, G.: 1983, *Astrophys. J.* **270**, 155

Bell, R.: 1992, *Mon. Not. Roy. Astron. Soc.* **257**, 423

Bergbusch, P., VandenBerg, D., and Infante, L.: 1991, *Astron. J.* **101**, 2102

Bertelli, G., Bressan, A., Chiosi, C., and Angerer, K.: 1986, *Astron. & Astrophys. Supp.* **66**, 191

Bertelli, G., Bressan, A., Chiosi, C., Fagotto, F., and Nasi, E.: 1994, *Astron. & Astrophys. Supp.* **106**, 275

Bessell, M. and Brett, J.: 1988, *Publ. Astron. Soc. Pacific* **100**, 1134

Boesgaard, A. and Friel, E.: 1990, *Astrophys. J.* **351**, 467

Boyle, W. and Smith, G.: 1970, *Bell Systems Tech. Journal* **49**, 587

Böhm-Vitense, E.: 1958, *Zs. Ap.* **46**, 108

Böhm-Vitense, E.: 1989, *Introduction to Stellar Astrophysics, Volume 2. Stellar Atmospheres*, pp 174–189, Cambridge University Press, Cambridge

Bressan, A., Bertelli, G., and Chiosi, C.: 1981, *Astron. & Astrophys.* **102**, 25

Burkhead, M., Burgess, R., and Haisch, B.: 1972, *Astron. J.* **77**, 661

Burstein, D., Faber, S., Gaskell, C., and Krumm, N.: 1984, *Astrophys. J.* **287**, 586

Caldwell, J., Cousins, A., Ahlers, C., van Wamelen, P., and Maritz, E.: 1993, *SAAO Circ.* (15)

Cameron, L.: 1985, *Astron. & Astrophys.* **147**, 47

Canterna, R., Geisler, D., Harris, H., Olszewski, E., and Schommer, R.: 1986, *Astron. J.* **92**, 79

Carlberg, R., Dawson, P., Hsu, T., and VandenBerg, D.: 1985, *Astrophys. J.* **294**, 674

Carraro, G., Chiosi, C., Bressan, A., and Bertelli, G.: 1994, *Astron. & Astrophys. Supp.* **103**, 375

Castellani, V., Chieffi, A., and Straniero, O.: 1992, *Astrophys. J. Supp.* **78**, 517

Cohen, J.: 1978, *Astrophys. J.* **223**, 487

Cohen, J.: 1982, *Astrophys. J.* **258**, 143

Cohen, J., Frogel, J., and Persson, S.: 1978, *Astrophys. J.* **222**, 165

Cohen, J. and Sleeper, C.: 1995, *Astron. J.* **109**, 242

Cousins, A.: 1976, *Mem. Roy. Astron. Soc.* **81**, 25

Crinklaw, G. and Talbert, F.: 1991, *Publ. Astron. Soc. Pacific* **103**, 536

Cudworth, K.: 1994, *Bull. Amer. Astron. Assoc.* **25**, 1454

Daniel, S., Latham, D., Mathieu, R., and Twarog, B.: 1994, *Publ. Astron. Soc. Pacific* **106**, 281

Davidge, T., Côté, P., and Harris, W.: 1996, *Astrophys. J.* **468**, 641

Dean, J., Warren, P., and Cousins, A.: 1978, *Mon. Not. Roy. Astron. Soc.* **183**, 569

DeMarque, P., Guenther, D., and Green, E.: 1992, *Astron. J.* **103**, 151

Dorman, B.: 1990, *Ph.D. thesis*, The University of Victoria

Dorman, B.: 1993, in G. Smith and J. Brodie (eds.), *The Globular Cluster-Galaxy Connection*, Vol. 48 of *ASP Conference Series*, p. 198, Astronomical Society of the Pacific

Dowler, P.: 1994, *Master's thesis*, The University of Victoria

Dowler, P. and VandenBerg, D.: 1996, *in preparation*

Eggleton, P.: 1983, *Mon. Not. Roy. Astron. Soc.* **204**, 449

Elias, J., Frogel, J., Matthews, K., and Neugebauer, G.: 1982, *Astron. J.* **87**, 1029

Faber, S., Friel, E., Burstein, D., and Gaskell, C.: 1985, *Astrophys. J. Supp.* **57**, 711

Ferraro, F., Pecci, F. F., Montegriffo, P., Origlia, L., and Testa, V.: 1995, *Astron. & Astrophys.* **298**, 461

Flannery, B. and Johnson, B.: 1982, *Astrophys. J.* **263**, 166

Friel, E.: 1987, *Astron. J.* **93**, 1388

Friel, E.: 1993, in G. Smith and J. Brodie (eds.), *The Globular Cluster-Galaxy Connection*, Vol. 48 of *ASP Conference Series*, p. 273, Astronomical Society of the Pacific

Friel, E.: 1995, *Ann. Rev. Astron. Astrophys.* **33**, 381

Friel, E. and Janes, K.: 1993, *Astron. & Astrophys.* **267**, 75

Frogel, J., Persson, S., Aaronson, M., and Matthews, K.: 1978, *Astrophys. J.* **220**, 75

Frogel, J., Persson, S., and Cohen, J.: 1981, *Astrophys. J.* **246**, 842

Frogel, J., Persson, S., and Cohen, J.: 1983, *Astrophys. J. Supp.* **53**, 713

Garnavich, P., VandenBerg, D., Zurek, D., and Hesser, J.: 1994, *Astron. J.* **107**, 1097

Geisler, D.: 1987, *Astron. J.* **94**, 84

Glass, I.: 1974, *Mon. Not. Astr. Soc. South Africa* **33**, 53, 71

Harris, W. and Canterna, R.: 1981, *Astron. J.* **86**, 1332

Hoag, A., Johnson, H., Iriarte, B., Mitchell, R., Hallam, K., and Sharpless, S.: 1961, *Publ. U.S. Naval Obs.* **XVII**, part VII

Hobbs, L. and Thorburn, J.: 1991, *Astron. J.* **102**, 1070

Houdashelt, M., Frogel, J., and Cohen, J.: 1992, *Astron. J.* **103**, 163

Iglesias, C., Rogers, F., and Wilson, B.: 1992, *Astrophys. J.* **397**, 717

Janes, K.: 1979, *Astrophys. J. Supp.* **39**, 135

Janes, K.: 1984, *Publ. Astron. Soc. Pacific* **96**, 977

Janes, K.: 1988, in A. Phillip (ed.), *Calibration of Stellar Ages*, p. 59, L. Davis Press, Schenectady

Janes, K. and Adler, D.: 1982, *Astrophys. J. Supp.* **49**, 425

Janes, K. and Phelps, R.: 1994, *Astron. J.* **108**, 1773

Janes, K., Tilley, C., and Lyngå, G.: 1988, *Astron. J.* **95**, 771

Janesick, J. and Elliott, T.: 1992, in S. Howell (ed.), *Astronomical CCD Observing and Reduction Techniques*, Vol. 23 of *ASP Conference Series*, p. 1, Astronomical Society of the Pacific

Jennens, P. and Helfer, H.: 1975, *Mon. Not. Roy. Astron. Soc.* **172**, 681

Johnson, H.: 1965, *Lunar Planet Lab., Arizona* **3**, 73

Johnson, H.: 1966, *Ann. Rev. Astron. Astrophys.* **4**, 193

Johnson, H., Hoag, A., Iriarte, B., Mitchell, R., and Hallam, K.: 1961, *Lowell Obs. Bull.* **5**, 133

Johnson, H. and Morgan, W.: 1953, *Astrophys. J.* **117**, 313

Joyce, R.: 1992, in S. Howell (ed.), *Astronomical CCD Observing and Reduction Techniques*, Vol. 23 of *ASP Conference Series*, p. 258, Astronomical

Society of the Pacific

Kaluzny, J.: 1990, *Mon. Not. Roy. Astron. Soc.* **243**, 492

Kaluzny, J. and Shara, M.: 1988, *Astron. J.* **97**, 785

Kaluzny, J. and Udalski, A.: 1992, *Acta Astron.* **42**, 29

Kaufmann, W.: 1987, *Discovering the Universe*, p. 209, W.H. Freeman and Company, New York

Kraft, R.: 1979, *Ann. Rev. Astron. Astrophys.* **17**, 309

Kron, G., White, H., and Gascoigne, S.: 1953, *Astrophys. J.* **118**, 502

Lada, C. and Lada, E.: 1991, in K. Janes (ed.), *The Formation and Evolution of Star Clusters*, Vol. 13 of *ASP Conference Series*, p. 3, Astronomical Society of the Pacific

Landolt, A.: 1992, *Astron. J.* **104**, 340

Langer, N.: 1986, *Astron. & Astrophys.* **164**, 45

Leonard, P.: 1996, in E. Milone and J.-C. Mermilliod (eds.), *The Origins, Evolution and Destinies of Binary Sters in Clusters*, Vol. 90 of *ASP Conference Series*, p. 337, Astronomical Society of the Pacific

Liebert, J., Saffer, R., and Green, E.: 1994, *Astron. J.* **107**, 1408

Lindoff, U.: 1972, *Astron. & Astrophys. Supp.* **7**, 497

Lyngå, G.: 1987, *Distributed by Centre de Donnes Stellaires, Strasbourg*

Maeder, A.: 1975, *Astron. & Astrophys.* **40**, 303

Maeder, A. and Mermilliod, J.-C.: 1981, *Astron. & Astrophys.* **93**, 136

Maeder, A. and Meynet, G.: 1989, *Astron. & Astrophys.* **210**, 155

Mateo, M.: 1988, in J. Grindlay and A. Phillip (eds.), *The Harlow-Shapley Symposium on Globular Clusters, IAU Symposium 126*, p. 557, Kluwer, Dordrecht

Matteucci, F. and Francois, P.: 1989, *Mon. Not. Roy. Astron. Soc.* **239**, 885

Mazzei, P. and Pigatto, L.: 1988, *Astron. & Astrophys.* **193**, 148

McClure, R. and van den Bergh, S.: 1968, *Astron. J.* **73**, 313

Mermilliod, J.-C.: 1981, *Astron. & Astrophys.* **97**, 235

Mermilliod, J.-C. and Maeder, A.: 1986, *Astron. & Astrophys.* **158**, 45

Mihalas, D. and Binney, J.: 1988a, *Galactic Astronomy: Structure and Kinematics*, p. 130, W.H. Freeman and Co., New York

Mihalas, D. and Binney, J.: 1988b, *Galactic Astronomy: Structure and Kinematics*, p. 103, W.H. Freeman and Co., New York

Mihalas, D. and Binney, J.: 1988c, *Galactic Astronomy: Structure and Kinematics*, p. 78, W.H. Freeman and Co., New York

Mihalas, D. and Binney, J.: 1988d, *Galactic Astronomy: Structure and Kinematics*, p. 116, W.H. Freeman and Co., New York

Montgomery, K., Janes, K., and Phelps, R.: 1994a, *Astron. J.* **108**, 585

Montgomery, K., Janes, K., and Phelps, R.: 1994b, *Astron. J.* **107**, 1408

Montgomery, K., Marschall, L., and Janes, K.: 1993, *Astron. J.* **106**, 181

Ortolani, S., Barbuy, B., and Bica, E.: 1990, *Astron. & Astrophys.* **236**, 362

Panagia, N. and Tosi, M.: 1981, *Astron. & Astrophys.* **96**, 306

Perry, D.: 1992, in E. Dereniak and R. Simpson (eds.), *Infrared Detectors and Focal Plane Arrays II*, Vol. 1685, p. 50, SPIE

Phelps, R., Janes, K., and Montgomery, K.: 1994, *Astron. J.* **107**, 1079

RCA Corporation: 1974, *RCA Electro-Optics Handbook, Technical Series EOH-11*, Commercial Engineering, RCA Corporation, Harrison, NJ

Reid, N.: 1993, *Mon. Not. Roy. Astron. Soc.* **265**, 785

Ridgway, S., Joyce, R., White, N., and Wing, R.: 1980, *Astrophys. J.* **235**, 126

Rieke, G. and Lebofsky, M.: 1985, *Astrophys. J.* **288**, 618

Rogers, F. and Iglesias, C.: 1992, *Astrophys. J. Supp.* **79**, 507

Rosvick, J.: 1995, *Mon. Not. Roy. Astron. Soc.* **277**, 1379

Sandage, A.: 1993, *Astron. J.* **106**, 703

Sanders, W.: 1972, *Astron. & Astrophys.* **19**, 155

Sarajedini, A. and Demarque, P.: 1990, *Astrophys. J.* **365**, 219

Searle, L. and Zinn, R.: 1978, *Astrophys. J.* **225**, 357

Sharov, A.: 1965, *Soviet A.J.* **8**, 780

Stetson, P.: 1987, *Publ. Astron. Soc. Pacific* **99**, 191

Stetson, P.: 1990, *Publ. Astron. Soc. Pacific* **102**, 932

Stetson, P. and Harris, W.: 1988, *Astron. J.* **96**, 909

Stix, M.: 1989, *The Sun: An Introduction*, p. 19, Springer-Verlag, Berlin

Strobel, A.: 1989, *Astron. Nachr.* **310**, 367

Strom, K., Strom, S., and Merrill, K.: 1993, *Astrophys. J.* **412**, 233

Strömgren, B.: 1963, *Q. J. Roy. Astr. Soc.* **4**, 8

Swenson, F., Faulkner, J., Rogers, F., and Iglesias, C.: 1994, *Astrophys. J.* **425**, 286

Tripicco, M., Bell, R., Dorman, B., and Hufnagel, B.: 1995, *Astron. J.* **109**, 1697

Twarog, B.: 1980, *Astrophys. J.* **242**, 242

van den Bergh, S. and Heeringa, R.: 1970, *Astron. & Astrophys.* **9**, 209

van den Bergh, S. and Sher, D.: 1960, *The David Dunlop Observatory* 2(7)

VandenBerg, D.: 1983, *Astrophys. J. Supp.* **51**, 29

VandenBerg, D.: 1985, *Astrophys. J. Supp.* **58**, 711

VandenBerg, D., Bolte, M., and Stetson, P.: 1990, *Astron. J.* **100**, 445

VandenBerg, D. and Poll, H.: 1989, *Astron. J.* **98**, 1451

Wainscoat, R. and Cowie, L.: 1992, *Astron. J.* **103**, 332

Wilking, B., Giblin, T., McCaughrean, M., Raynor, J., Burton, M., and Zinneker, H.: 1994, in I. McLean (ed.), *Infrared Astronomy with Arrays: The Next Generation*, Vol. 190 of *Astrophysics and Space Science Library*, p. 17, Kluwer Academic Publishers, Dordrecht

Wilson, W., Schwartz, P., Neugebauer, G., Harvey, P., and Becklin, E.: 1972, *Astrophys. J.* **177**, 523

Zahn, J.-P.: 1983, *Astrophysical Processes in Upper Main Sequence Stars*, Technical report, Geneva Observatory

Zinn, R.: 1991, in K. Janes (ed.), *The Formation and Evolution of Star Clusters*, Vol. 13 of *ASP Conference Series*, p. 532, Astronomical Society of the Pacific

Appendix A

This Appendix presents $(J-K, V-K)$ and $(J-H, H-K)$ diagrams of the cluster giants (Figures A.1 and A.2). Although it was found that these data were not very useful to the cluster analysis, they were included here for completeness' sake.

The cluster giants have been corrected for colour excess as given in Section 4.2. Also plotted are field relations for giants and dwarfs from Frogel et al. (1978), and the globular cluster giant relation given by Frogel et al. (1983). This relation uses the mean values for the globular clusters M3, M13 and M92.

The $(J-K, V-K)$ diagram (Figure A.1) is not very useful in determining cluster membership, since the reddening line is nearly parallel to the curve, and the globular cluster and field giant relations are not well separated in the region where most of the stars are located. Thus, it is impossible to tell which cluster giants are members and which are not, since all giants should be expected to lie in the vicinity of these loci.

The $(J-H, H-K)$ diagram (Figure A.2) is quite scattered, and the giants of NGC 6819 and NGC 6791 also appear to be offset from the field giant relation. Two effects may be producing the offset and scatter.

First, the presence of binary companions could introduce some scatter since the magnitude and colour of the binary pair would be different from

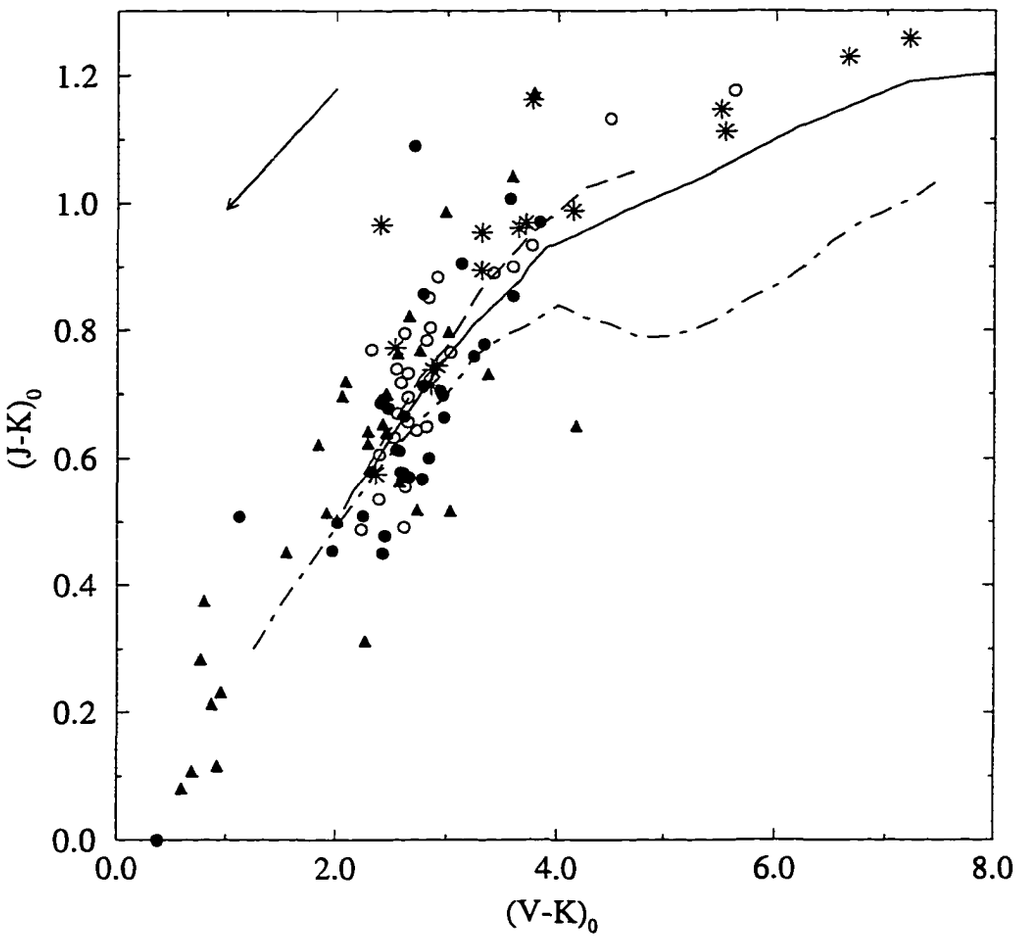

Figure A.1: $(J-K, V-K)$ diagram for the cluster giants. Symbols are as follows: filled circles = NGC 2141, open circles = NGC 6819, filled triangles = NGC 7142 and stars = NGC 6791. The solid and dot-dashed lines are from Frogel et al. (1978) and represent field giants and dwarfs, respectively. The globular cluster relation, shown as a dashed line, is the mean relation of M3, M13 and M92 from Frogel et al. (1983). The reddening line is indicated in the upper left corner.

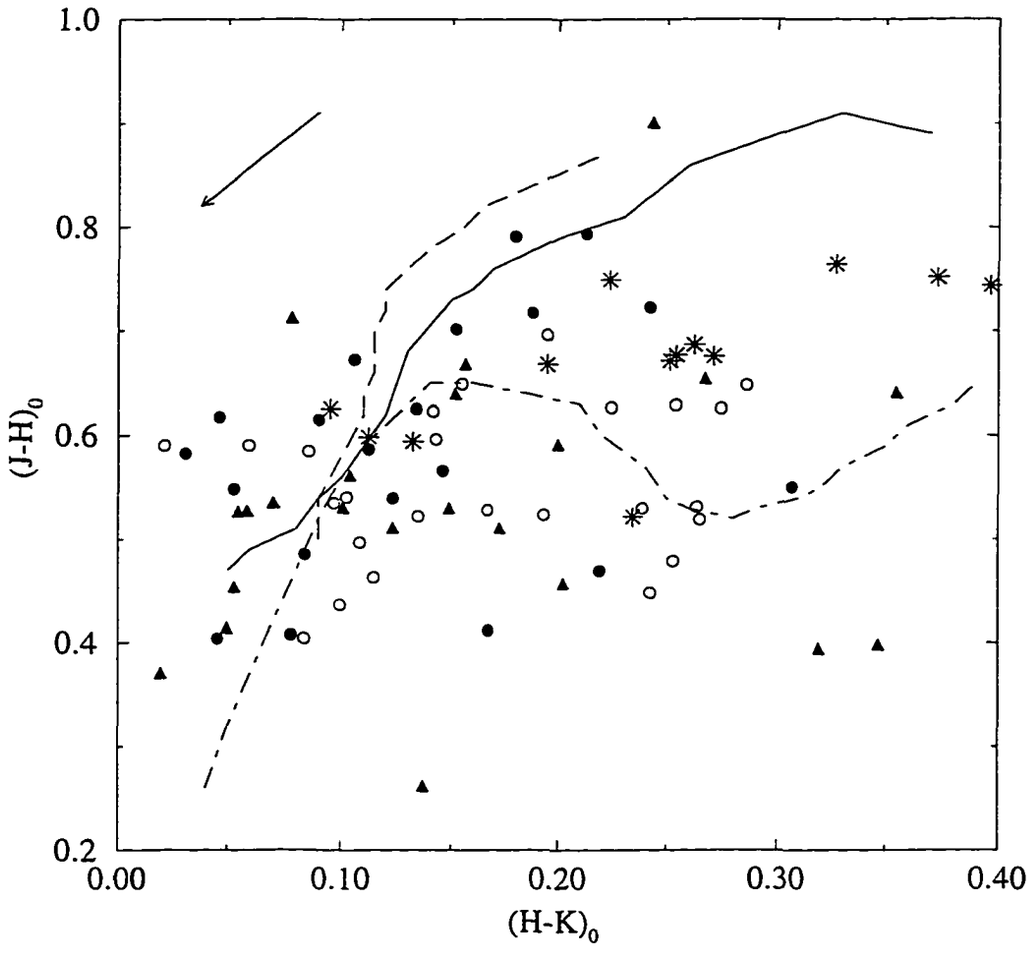

Figure A.2: $(J-H, H-K)$ diagram for the cluster giants. All symbols and lines are as in the previous figure.

what would be expected for a single giant. However, this depends on the magnitude of the companion, and the colours at infrared wavelengths would not be expected to change that much since the giant branch in an IR CMD is nearly vertical, and the clump stars do not span a wide range of colour. Also, a mass ratio of $q \sim 1$ would be required to avoid having main sequence or white dwarf companions. Thus, the presence of binary companions is not expected to contribute very much to the problem.

Water vapour absorption in the line of sight to the clusters, terrestrial in origin, is believed to be the major contributor to both the scatter and the offset. Even though the sky may appear photometric, moisture in the atmosphere from an approaching or receding weather system may be substantial. As a result, water vapour bands which are present near the windows occupied by the IR passbands may become saturated and encroach upon the IR windows. In particular, a water vapour band at 1.9 μm is known to fall into both the H and K passbands (see Figure 2.3). Since several of the observing nights were either hazy, partly cloudy, or clear but bracketed by overcast nights, this seems a plausible explanation. The offset in Figure A.2 is in the sense that $(J - H)$ becomes bluer while $(H - K)$ becomes redder, which indicates that the H filter is subjected the most to water vapour absorption. Presumably this is due to an additional absorption band at 1.4 μm interfering with the wing of the H passband.

Appendix B

This Appendix contains details of the reduction process from instrumental to standard magnitudes via Peter Stetson's (private communication) set of programs available at the University of Victoria, and is meant to be used in conjunction with the documentation file written by Peter Stetson. I have included some of this file (shown here in slanted text), which accompanies the executable programs and is called *ccdpck.man*. Throughout this document, program names will be capitalized to avoid confusion, even though on Unix systems they should be typed in lower case letters. Note that the programs are untidy and complicated since they were written at different times, and what's recorded in output files is not always what the Fortran program file says should be there. Presumably this is due to the executable versions of the program being derived from different versions of the code, to which we have no access. However, I have tried to explain as much as I can, in those cases.

The Exposure Information File

The first file to create is the one containing the exposure information. This file must have the extension .inf (I have found that the root name chosen doesn't matter, as long as that name is kept as the root name for all subsequent files). Included below are the first few lines from one of my files:

```
f906              1   2 58  1.529  60.010  2449385.6234       test
f907              1   3 00  1.495 600.010  2449385.6281       test
f908              2   3 11  1.478 600.010  2449385.6362       test
f909              2   3 23  1.441  60.010  2449385.6411       test
```

This file contains the name of the frame, the filter identification, the UT in hours, the UT in minutes, the airmass, the exposure time in seconds, the Julian Date and the root name of the calibration (.clb) file (more on this file later).

The filters are numbered consecutively from 1 through N. In this case, $1 = V$ while $2 = I$. This convention must be maintained throughout all subsequent files. The exposure time must contain the fraction 0.010 seconds, because of a problem with the shutter timing on the KPNO 4-m prime-focus canera which existed when Peter Stetson wrote the programs.

The format of the above file is as follows:

```
format(1x,a30,i3,f4.0,f3.0,f7.3,f8.1,f14.4,1x,a30)
```

This format must be adhered to strictly when the exposure information is typed in.

Fetch files, DAOMATCH and DAOMASTER

The next step involves creating "fetch" files for each field. Peter Stetson explains this file in the following manner:

> *I have written some programs that make life easier when you have several frames for a field. First, you want to choose your "best" frame of each field, whether that be the deepest frame, or the most centered frame, or whatever. The first thing you want to do is associate the real-world names of the objects contained within that frame with their positions in the frame. This information*

> *is contained in what I call a "fetch" file, filename.fet ... Note that the only things that matter in this file are the object name in columns 2-13 of the first line, and the x,y coordinates in columns 7-24 of the second line for each object. Anything else is optional.*

In order to choose good fetch file stars, I suggest you look at your images, decide which frame is the best (I found myself using the most centred, long-exposure V frame the most), and select stars which are bright (but not saturated in any of the other frames) and fairly isolated. I took appropriate lines from the .als files (the output file from ALLSTAR) and created a temporary file which was passed as input to a simple program I wrote to create fetch files with the correct format. I include a few lines from one of my fetch files:

```
0n2141-28
    28   670.95   866.11   10.684    0.002
0n2141-34
    34   387.12   964.83   10.868    0.002
0n2141-39
    39   583.62   430.89   10.953    0.002
0n2141-40
    40   285.13   388.67   10.971    0.002
0pg0231-B
     3   511.90   506.81   13.672    0.007
0pg0231-0
     1   608.85   365.95   15.133    0.018
0pg0918-B
     8   576.85   671.26   12.711    0.005
0pg0918-A
     9   414.82   773.19   13.259    0.006
```

The first line contains the star name preceded by "0" (this character is nec-

essary for the subsequent programs, since it tells the programs that that star is a bona fide standard star), while the second contains the star's ID number (from the .als file), the coordinates, the magnitude and the magnitude error. The star name given in this file must be identical to that given in the library file (.lib extension). Creation of the library file will be explained later.

The programs DAOMATCH and DAOMASTER are used to create a large coordinate system grid based on the frame for which the fetch file is defined, and cross-identify stars which appear on several different frames. The name of the .als file from the best frame is given first to DAOMATCH; subsequent files are the .als ones from the other frames. The program determines coordinate transformations between the best frame and the others specified above, according to the following equations:

$$x(1) = A + C * x(n) + E * y(n)$$

$$y(1) = B + D * x(n) + F * y(n)$$

The results are typed out as the following equations:

```
'f907.als'      0.000    0.000   1.00000   0.00000   0.000   1.00000
'f906.als'      0.083   -0.518   1.00000   0.00000   0.000   1.00000
'f908.als'      1.425   -1.241   1.00000   0.00000   0.000   1.00000
'f909.als'      1.669   -0.462   1.00000   0.00000   0.000   1.00000
```

The excerpt above is taken from one of my output files. These files have a .mch extension. Note that the lines above are not formatted correctly; I altered the lines to remove some of the blank space between the columns so that the lines would fit in the space of the text. This file includes the .als filename and the transformation constants defined by the equations given above.

DAOMASTER is used to cross-identify all the stars on all the frames, and refine the transformation equation estimates produced by DAOMATCH.

This is done iteratively. The program asks for the .mch file created by DAOMATCH, followed by various constraints which it uses to determine whether a star is to be regarded as real (and therefore kept) or false (and discarded). These constraints are given below:

- *First, how many frames was the star detected in? You must enter three numbers, separated by commas or spaces, in the following order:*

  1. *Minimum number of frames. A star absolutely must be detected in at least so many frames, or it is discarded. If you are willing to keep detections that were seen only once, and did not appear in other frames of the same field, you may set this to 1.*
  2. *Minimum fraction of frames. Of those frames that a star may reasonably be expected to appear in (its average position, transformed to the coordinate system of this frame falls within this frame; its average magnitude, offset to the magnitude system of this frame is reasonably bright compared to the magnitude limit of this frame), it actually is found in at least this fraction of them. The fraction must be between 0.0 and 1.0, inclusive.*
  3. *Enough frames. Any star which appears in at least this many frames will be accepted, regardless of how many frames it could have been found in.*

- *Reject any star with too uncertain a magnitude. DAOMASTER asks for "Maximum sigma", and you type in a number. A star will be rejected if its mean instrumental magnitude, based on a weighted average of all available observations corrected to the magnitude scale of the "best" frame is larger than the number you type in.*

- *Then you specify how complicated a transformation you want. If your frames for this field were all taken one right after another on the same night with the same telescope, then you might answer "2" and DAOMASTER will solve only for mean offsets A and B among the various frames. If you answer "4" DAOMASTER will solve for the four constants in these equations:*

$$x(1) = A + C*x(2) +/- D*y(2) y(1) = B + D*x(2) +/- C*y(2) \quad \text{(B.1)}$$

which allow for arbitrary rotation angles and scale differences, as well as translations of the origin...If you answer "6" MASTER solves for all of A, ..., F in the equations above.

- *Finally you specify a match-up radius. After having transformed the stars in frame n to the coordinate system of the master frame, stars will be cross-identified only if their positions agree to within that tolerance.*

The match up radius specified in the last constraint initially should be large (I usually started with 10 pixels), since the transformation equations from DAOMATCH are only approximate. DAOMASTER goes through the star lists and matches as many stars as it can to stars in the master list. Many of these identifications will be spurious, but the number of legitimate cross-identifications will outnumber them. Corrections are applied to the approximate transformation equations, and another iteration is performed. You are asked to enter another match up radius (which should be smaller than the previous one), and this process goes on until the master list converges. At this point, various outputs are possible:

1. *A file with mean magnitudes and scatter? If you answer "y" it will correct all observed magnitudes for each star to the system of frame 1, take a robust average, and write out to a disk file the resulting mean*

magnitude, standard error of the mean, the ratio of the magnitude scatter observed to that expected from the individual standard errors, and the root-mean-square chi value.

2. *A file with corrected magnitudes? If you answer "y" it will correct all observed magnitudes for each star to the system of frame 1, and write them all out to a disk file. You can then search for variables (for instance), using your own algorithms.*

3. *A file with raw magnitudes and errors? If you answer "y" it will simply write out all the instrumental magnitudes observed for each star.*

4. *A file with the new transformations? If you answer "y" it will write out a new .MCH file with the latest set of transformation constants, plus the mean magnitude offsets.*

5. *A file with the transfer table? If you answer "y" it will write out a file which contains where each star in the master list appears in each of the input files: Star 1 in the master list is the 37th star in frame 1, it doesn't appear in frame 2, it is the 1193rd star in frame 3.*

6. *Individual .COO files? If you answer "y" it will invert the transformation equations and project each star in the master list to where it SHOULD have appeared in each of the CCD frames. It will then create new .COO files, so that if you want you can go through aperture and profile-fitting photometry with exactly the same star list for every frame. A star will not be written to a .COO file if it falls outside the actual area of that frame, however.*

7. *Simply transfer star IDs? If you answer "y" it will create verbatim copies of all of the input files with only the ID numbers changed, so*

that the same star has the same ID number in all frames. If you have not used the renumber option above, the ID number will be transferred from frame 1 to each of the other frames, except that stars in the master list that are not in frame 1 are given consecutive numbers starting with 50001. The new files are given the same filenames as the input files, with extensions .MTR.

I found it useful to look at the files produced by the first three output options, but these files were not required for the subsequent programs. However, it is necessary to choose options 4 and 5, since the fourth one produces the new .mch file (which includes mean magnitude offsets from each frame to the master one), while the fifth is used in the final reduction program. The few lines below are taken from one of my transfer (.tfr) files:

```
f907.als                          99.9990   9.9990
f906.als                          99.9990   9.9990
f908.als                          99.9990   9.9990
f909.als                          99.9990   9.9990
 ==============================
50001  711.463  636.028    0     1     0     2
50002  416.229  831.497    0     2     0     3
50003  710.745  634.517    0     0     0     0
50004  568.343  212.097    0     4     0     1
```

The master star ID is contained in the first column under the double horizontal line, while the coordinates on the master grid are in the second and third. The numbers in the subsequent columns point to the location in the .als files of each star. For example, star 50001 was not found in f907.als, was the first star in f906.als, was not found in f908.als and was the second star in f909.als.

DAOGROW

The next step involves computing the total, integrated instrumental magnitudes of the primary standards, as well as local standards on each of the object frames. The program DAOGROW, which utilizes aperture photometry and curve-of-growth analysis, may be used to obtain these magnitudes. DAOGROW (Stetson, 1990) requires the name of the file defining the aperture radii which were used for the aperture photometry (the photo.opt file should be used here), the name of the .inf file containing the airmasses for all the .ap files, and a file containing the names of all the .ap files, one filename per line.

I used the fetch files to select common stars on each set of related frames, and created temporary files containing these local standard stars. I then used the program DAOPHOT to subtract from the frames all the stars except those in the temporary files. Aperture photometry of the local standards was performed on the star-subtracted frames, and these .ap files were the ones used in DAOGROW. The program asks for the following parameters:

> *DAOGROW will ask you how many of the parameters A, B, C, D, E you want to solve for. If you answer "4" it will solve for A, ..., D; if you answer "2" it will solve for A, and B; and so on. It will always solve for at least A and a seeing radius for every frame. DAOGROW will ask you to type in values for the remaining parameters that you do not want new solutions for. I suggest D = 0.9 and E = 0.0, unless you have better information to the contrary.*
>
> *DAOGROW will now ask for the "Maximum magnitude error." When the program sees an aperture magnitude with a standard error larger than the value you enter, that magnitude and the mag-*

nitudes from all larger apertures for that star will be discarded.

DAOGROW will now fit the growth curves. It will type out values for each of the five parameters A, ..., E followed by an estimate of the current scatter of residuals, as the solution iterates. After convergence it will type out the final values for these numbers, and estimates of the standard errors of the final values. Finally, it will type out for each aperture the "average" value of the analytic model values for the difference between that aperture and the next smaller one, taken over all frames; the average residual between the actual, observed magnitude differences and the analytic models, taken over all stars in all frames; and the rms residuals of the actual magnitude differences from the analytic model growth curves, over all stars and frames. These allow you to see whether there is some gross mismatch between the family of analytic models and the imaging properties of your telescope.

DAOGROW produces several files, but the only one used in subsequent programs has a .tot extension. A sample is included below:

```
NL    NX    NY  LOWBAD HIGHBAD  THRESH     AP1  PH/ADU  RNOISE
 1 1024 1024   149.0 40000.0   41.37    3.00    4.00   15.00

 30  649.923  813.337  12.9388   0.0071  13.0600  -0.1212    7
124  356.821  913.996  14.8026   0.0190  15.0210  -0.2184    5
 39  563.426  378.594  13.2168   0.0086  13.3380  -0.1212    7
 43  265.153  336.280  13.2428   0.0076  13.3640  -0.1212    7
 63  551.593  478.668  13.5176   0.0083  13.6690  -0.1514    6
```

The columns contain the ID, x and y coordinates, corrected magnitude and error, uncorrected magnitude, the aperture correction and the aperture radius used which contains the total light from the star.

CCDOBS

The next file you must create will contain the observed instrumental magnitudes of the primary standards, as well as local standards (the ones which were chosen for the fetch files will work well). The program CCDOBS requires an output filename (with the extension .obs), labels for the magnitudes you are using, the file containing the exposure information (the .inf file), the coordinate transformation file (the .mch file created by DAOMATCH and modified by DAOMASTER) and the name of the fetch file (the one with the .fet extension). I have found that if all these files have the same root name, then a lot of hassle is avoided later on.

The program then asks for a maximum match-up radius. I specified 2 or 3 pixels, so that any star falling within this many pixels of the predicted position (based on the .mch transformations) will be identified as one matching one of the stars in the fetch file. The next set of input files are the .tot ones from DAOGROW. For the stars which are found, the program types out their positions, magnitude and error from the best aperture, and the aperture correction. Any stars too faint or outside the field will have only their predicted coordinates typed out.

Once all the .tot files have been entered, typing ctrl-d several times will step you back to earlier stages of the program, and eventually out of it entirely.

The following excerpt is from one of my .obs files.

```
2 MAGNITUDES:  (1) v      (2) i
Star          Mag.  H  M     X       Int.     Mag.      sigma     corr.
pg0231-B       1    2 41   1.395    60.010   13.672    0.0074   -0.118   f902
   511.90   506.81
pg0231-B       2    2 44   1.398    60.010   11.821    0.0047   -0.088   f903
   510.25   507.66
```

```
n2141-28      1    2 58   1.529   60.010   13.159   0.0062   -0.081   f906
   670.88   866.62
n2141-28      2    3 23   1.441   60.010   12.081   0.0044   -0.050   f909
   669.24   866.49
```

In the above example, I am working with two filters, V and I. The next line gives the star name, the filter ID, the UT in hours and minutes, the airmass, the integration time, the instrumental magnitude and error, the aperture correction, the name of the frame on which the stars are found and the coordinates. The exposure information was taken from the .inf file, while the magnitudes and star names were read from the .tot and .fet files. I have included one primary (pg0231-B) and one secondary (n2141-28) standard.

CCDLIB

This program is used to create a file containing the standard magnitudes and colours for the standard stars. Once an output filename has been entered, the program asks for the standard photometric indices (a maximum of six are allowed. In this case, indices refer to both magnitudes and colours). Usually, one magnitude plus some number of colours are entered. CCDLIB then asks for the star ID numbers, which are composed of a prefix and individual star IDs. The total ID numbers must be less than 12 characters. The program also asks for standard errors for each photometric index. A sample file is given below. Note that the star IDs are identical in format to the ones given in the fetch file.

```
2 INDICES:                V                    V-I
pg0231-0            16.1050   0.0068   -0.5340   0.1221
pg0231-B            14.7350   0.0030    1.9510   0.0057
pg0918-B            13.9630   0.0034    0.7870   0.0056
pg0918-A            14.4900   0.0033    0.6610   0.0085
```

CCDSTD

This program transforms the instrumental magnitudes from CCDOBS to standard magnitudes using the standard magnitudes and colours from CCDLIB, via least-squares analysis of the transformation and extinction coefficients. However one additional file is required before the transformation can be computed. This extra file contains information on how the photometric indices are formed from the constituent magnitudes, as well as equations relating the observed instrumental magnitudes to the standard magnitudes. If some of the transformation coefficients are known beforehand, they are included in this file. A sample is given below:

```
M1=I1
M2=I1-I2
I1=M1
I2=M1-M2
O1 = M1 + A0 + A1*I2 + A2*X
O2 = M2 + B0 + B1*I2 + B2*X
```

The first line of the file relates the first standard magnitude M1 to the first standard photometric index I1 in the library, while the second indicates to the program how to compute the second standard magnitude M2 from the first and second photometric indices. In this case, M1 = V, and I1 = V, while M2 = I (formed from the difference in the two indices V and $(V - I)$). The third and fourth lines relate the indices to the magnitudes. The last two lines relate the observed magnitudes O1 and O2 to the standard magnitudes and indices via the transformation coefficients A0 through A2, and B0 through B2 (X is the airmass of the observation). The coefficients are the zero point, colour terms, and first order extinction.

The program outputs a file with a .clb extension (this is the transformation equation file I mentioned in the description of the .inf file), and a file of

residuals with extension .rsd. Examples of these two files are given below.

```
M1=I1
M2=I1-I2
I1=M1
I2=M1-M2
O1 = M1 + A0 + A1*I2 + A2*I2*I2 + A3*X + A4*I2*X
O2 = M2 + B0 + B1*I2 + B2*I2*I2 + B3*X + B4*I2*X
A0 =   3.1181011
A1 =  -0.1799160
A2 =   0.1124521
A3 =   0.1745649
A4 =   0.1343253
B0 =   3.2405980
B1 =  -0.1701460
B2 =   0.1093539
B3 =   0.1486126
B4 =   0.1575854
S1 =   0.0163537
S2 =   0.0205413
```

```
M1=I1
M2=I1-I2
I1=M1
I2=M1-M2
O1 = M1 + A0 + A1*I2 + A2*I2*I2 + A3*X + A4*I2*X
O2 = M2 + B0 + B1*I2 + B2*I2*I2 + B3*X + B4*I2*X

Fitting residuals in v

      (Computed magnitudes and residuals are on the instrumental system.)

Star          Frame                              T      X     Int.   Std.
 Obs    Comp.  Resid.  Sig.    wt    V      V-I
pg0231+051-B 1.90   506.81                   2.683  1.395   60.0
 14.735  18.00  17.993  0.006  0.018   1.00 14.735  1.951
```

```
.
.
.
 20 standards     1 ?'s     0 !'s

A0 =   3.1181 +- 0.0162
A1 =  -0.1799 +- 0.0242
A2 =   0.1125 +- 0.0104
A3 =   0.1746 +- 0.0302
A4 =   0.1343 +- 0.0397

   20 stars, additional observational scatter = 0.0164, average standard
error 0.0196 per observation.

Fitting residuals in i

      (Computed magnitudes and residuals are on the instrumental system.)

Star          Frame                              T      X     Int.   Std.
 Obs     Comp.  Resid.  Sig.    wt   V      V-I
pg0231+051-B 0.25   507.66                   2.733  1.398   60.0  12.784
16.179  16.176  0.002  0.022   1.00 14.735  1.951
.
.
.
 25 standards     2 ?'s     0 !'s

B0 =   3.2406 +- 0.0200
B1 =  -0.1701 +- 0.0317
B2 =   0.1094 +- 0.0132
B3 =   0.1486 +- 0.0386
B4 =   0.1576 +- 0.0570

   25 stars, additional observational scatter = 0.0205, average standard
error 0.0256 per observation.
```

The second example is fairly self-explanatory with regards to the content,

with the exception of the column called "Frame". This should contain the frame name on which the stars in column 1 are found. However it gives two numbers instead. To date, I have not found the source of these numbers, and the program itself indicates the frame name should be written. The only explanation I have at this time is the executable form of the program is from a different version of the Fortran program given in the directory.

Following is an excerpt from Peter Stetson's file about the additional observational scatter and "?" and "!":

> *Notes concerning the .RSD file*
>
> *"Additional observational scatter": The user has specified in the input to the program (a) the uncertainty of the standard photometric indices from the literature, and (b) the uncertainty of the instrumental magnitudes from the observational data. Taken together, these imply the amount of scatter that the standard-star observations may be expected to show about the best-fitting transformation. In fact, the scatter is almost always observed to be larger than this, due presumably to error sources which are unrelated (a) to the observational errors of whoever set up the standard system, and (b) to the readout noise and Poisson statistics of the CCD observations. Examples of these error sources are: variations in transparency during the night; changes in the quantum efficiency of the detector; errors in the flat-fielding of the data, combined with the stars' being observed at different places on the chip; neglected higher-order terms in the transformations or simple star-to-star spectral differences which can not be related to the data at hand (e.g. two stars with exactly the same standard (B-V)'s might have different instrumental (b-v)'s if they have dif-*

ferent metallicities, gravities, or reddenings, and if the standard and instrumental bandpasses are sufficiently different). All such additional sources of error are described by the "additional observational scatter." The program varies this quantity until the expected and observed scatters are equal. Each star is weighted in the fits by

$$wt = 1/[(err\ of\ std.\ ind.)^2+(err\ of\ obs.\ mag)^2+(add.\ obs.\ scat.)^2] \quad \text{(B.2)}$$

"?" and "!": Any residual which is between two and three standard errors [std error = quadratic sum of (error of std. indices), (error of obs. mag), and (add'l obs. scatter)] is flagged with a "?". Any residual larger than three standard errors is flagged with a "!".

The .RSD file also types out for every star a weight describing the amount of confidence the program places in that observation. Large residuals get reduced weight (= reduced confidence), so truly discordant observations should not distort the answers too much. Finally, the last columns for each star in the .RSD file give all the standard photometric indices for the star, so it is easy to use supermongo or some other plotting package to produce plots of residual versus everything under the Sun to look for systematic effects.

Stars which appear in the .OBS file but not in the .LIB file are treated as program objects. CCDSTD will type out their names on the terminal just so you can check and make sure they aren't typos. These stars will not be used to compute the transformations, but after the transformations have been computed they can be applied to the observations of these stars (see CCDAVE below).

CCDAVE

This program takes the observations of each star in the .obs file, and computes the best average photometric indices on the standard system, using the .clb files generated by CCDSTD. The program asks for the library file, an output filename (extension .net) and the .obs file. The program is capable of using more than one .obs file, should you have several. The program then asks if you wish to use non-library stars. If you answer yes, the stars in the .obs file which do not appear in the .lib file (*i.e.* the local standards from the program frames) are included in the star list and reduced to the standard system as well. Finally, the program prompts for quantities called "sigma multipliers". These numbers account for additional night-to-night scatter which is not always predicted correctly from the standard errors associated with the photometry. After the standard error has been derived for each observation, it is multiplied by the appropriate sigma multiplier. I usually set these to 1.0 initially, and ran the program a few times to get the correct numbers.

In addition to the .net file, the program generates an output file with a .ave extension. While the .net file contains only the final average magnitudes for each star (local standards included, if you answered yes to the question described above), the .ave file contains all the reduction information. Samples of the two files are given below.

2 INDICES:		V		V-I			
pg0231-0	1.000	16.1548	0.0591	-0.3723	0.1257	1	1
pg0231-B	1.000	14.7400	0.0431	1.9550	0.0774	1	1
pg0918-B	1.000	13.9687	0.0408	0.7688	0.0759	1	1
pg0918-A	1.000	14.4954	0.0417	0.6598	0.0781	1	1
n2141-28	2.390	14.4024	0.0335	1.3001	0.1341	6	2
n2141-34	0.952	14.5966	0.0137	0.7383	0.0391	6	4

```
n2141-39          1.047  14.6567   0.0126   0.7289   0.0350    8    6
n2141-40          1.068  14.6248   0.0240   1.6204   0.0681    4    1

-------------------------------------------------------------------------

pg0231-0

  16.155  0.025  10  8.85   365.9  16.527  0.036  10  7.20   366.8
 ---------------                   ---------------
  16.1548 0.0246   1.00            16.5271 0.0364   1.00

n2141-34

  14.586  0.017  10  7.04   965.3  13.895  0.021  10  5.71   966.0
  14.653  0.017   6  7.12   964.8  13.921  0.021  10  5.50   965.3
  14.557  0.017   8  6.91   964.6  13.821  0.021  10  5.36   965.6
  14.606  0.017  10  6.65   963.5  13.794  0.022  10  5.57   554.7
  14.583  0.017  10  6.28   553.0
  14.600  0.017  10  6.63   554.1
 ---------------                   ---------------
  14.5944 0.0111   1.78   0.0194   13.8581 0.0367   3.43   0.0693
```

Note that the .net file has the same format as the .lib file, with the addition of a column of numbers between the star name and the standard photometric indices. These numbers are the root-mean-squares of the χ values. The last two columns contain the number of frames in each filter.

The .ave file contains the star name, followed by the calculated magnitude and its observational error, a weight based on the residual, and what should be the frame ID (but looks like it isn't), for each photometric magnitude. Underneath the dashed line is the weighted average photometric magnitude on the standard system (in this case V and I), its average standard error, the χ value (the ratio of the observed observation-to-observation scatter to the expected observation-to-observation scatter). Since these values are both greater than one in the case for star n2141-34, an additional number is given,

which is the amount of additional scatter shown by the magnitudes (0.0194 mag in the case for the first filter).

REDUCE

The final program in the set transforms all the instrumental photometry to a standard system, and produce average indices. The program asks for the file with the observational data (the .inf file), the file with the transfer table (the .tfr table which was generated by DAOMASTER), the file with the frame pairs (type ctrl-d if you don't have this file to skip the question), the standard star library (give it the .net, not the .lib, file so that the local standards will be used as well), the name of the fetch file (.fet extension), the critical radius (2 or 3 pixels is fine), the sigma multiplier values you specified in CCDAVE, and the output filename. Note that two output files are produced – the first one has extension .fnl and contains the final, average magnitude and colours, while the second one has the extension .zer and contains the zeropoints for each frame.

Sample .zer and .fnl files are given below.

```
14.657  17.733  17.672   0.062   0.021   6   n2141-39
14.906  18.038  17.988   0.051   0.023   7   n2141-58
15.718  18.804  18.774   0.031   0.022  10   n2141-117
16.081  19.202  19.176   0.027   0.028  10   n2141-154
15.496  18.572  18.575  -0.003   0.021   7   n2141-102
15.164  18.242  18.207   0.035   0.024   9   n2141-80
15.223  18.308  18.316  -0.007   0.024   7   n2141-83
14.049  17.217  17.217   0.001   0.021   8   n2141-19
15.715  18.793  18.778   0.016   0.024  10   n2141-115
15.497  18.580  18.547   0.034   0.023   9   n2141-103
14.799  17.926  17.916   0.010   0.030  10   n2141-48
                        ------- -------
                         0.0231  0.0073  f914.als
```

```
                          11  .9271

    0.0231    0.0073    0.9271   11   f914.als                    <<

-------------------------------------------------------------------------
 50001  711.463  636.028  11.0211   0.0097   1.0734   0.0247    0.965   -0.020
 0.000   0   3   1
 50002  416.229  831.497  11.1184   0.0092   1.1338   0.0244    0.709    0.060
 0.000   0   2   1
 50003  710.745  634.517  11.8204   0.0230   2.0405   0.0376    1.195    0.006
 0.000   0   1   1
```

The .zer file contains the standard magnitude from the .net file, the raw magnitude from the .als file corrected for exposure time and a zeropoint term (called *dat* in the program) which is derived from the standard and raw magnitude and a transformation term obtained from the airmass and time of observation, the magnitude from the .als file corrected only for exposure time, the *dat* value, the square root of the sum of the errors from the standard and raw magnitudes, the weight, and the secondary standard ID name. Under the dashed lines are the average zeropoint, error, file from which the standard stars were taken, the number of observations in the average and the mean error of unit weight. This information is repeated on one line.

The .fnl file contains, for each star, an ID number, x and y coordinates, a magnitude and error, colour (or colours) and error(s), values for χ and sharpness, two values which should be non-zero if you had files of frame-pairs which you specified at the beginning of the program (I didn't need this option, which I assume would be useful for variable star searches, so I don't know what these numbers should be) and the number of V and I frames in which the star appeared.